Modeling and Simulation of Wavelength-tunable Laser Diodes for WDM System

by

Wei Li

A thesis
presented to the University of Waterloo
in fulfillment of the
thesis requirement for the degree of
Doctor of Philosophy
in
Electrical and Computer Engineering

Waterloo, Ontario, Canada, 2000

Th University of Waterloo requires the signatures of all persons using or photocopying this thesis. Please sign below, and give address and date.

Abstract

Wavelength tunable semiconductor laser diodes are one of the most important devices in wavelength division multiplexing (WDM) optical communication systems. There has been intensive research effort to extend the tuning range of laser diodes, in order to increase the transmission capacity and to add other system functions to the existing optical systems and networks. Since the laser fabrication process is complicated and expensive, modeling and simulation become increasingly important to reduce development time and cost. The theme of this dissertation is to develop efficient and accurate models and simulation techniques for laser diodes in general and tunable lasers in particular.

A comprehensive hierarchical model framework is developed and validated, which spans from the material models to the longitudinal waveguiding structures commonly used for tunable lasers. A series of models are established to simulate the intrinsic refractive index and refractive index changes caused by carrier injection, thermal effects and applied electric field. An optical gain model for strained multiple quantum well (MQW) materials is developed based on accurate band structure calculations. Comparisons with experimental data for some of these material models are made and show good agreement.

A comprehensive traveling wave model is developed, which takes into account of spatial-hole-burning, spontaneous random noise as well as material effects in laser diodes with complex longitudinal configurations. Especially, thermal effects are incorporated into the traveling wave model for the first time. With the help of the new model, the various thermal time constants during the large signal modulation of a DFB

laser observed experimentally are explained. To improve the computational efficiency and the application versatility of the conventional traveling wave approach, we have proposed and demonstrated a digital filter approach, which combines the standing wave and the traveling wave models. This novel idea makes the traveling wave model more versatile and efficient, especially in simulation of laser diodes integrated with long optical waveguide structures.

Another major contribution of this work is the applications of the models and the simulation techniques for several novel tunable lasers. As the first example, the sampled grating assisted wavelength tunable laser is investigated. In this category, two kinds of devices are discussed. One is the DBR (Vernier ruler type) tunable laser; the other is DFB type tunable laser cascaded with a co-directional filter as wavelength selection element. This work is the first comprehensive simulation based on a rigorous numerical model. Secondly, we modeled and simulated a wavelength tunable multi-section gain-coupled DFB cascade. The interaction between the adjacent section is considered, and some key design parameters are optimized. In the design, the CW working condition and the tuning mechanism are demonstrated. Further, the condition and the characteristics of short pulse generation resulting from multi-mode nature of this complex DFB cascade is also identified.

Acknowledgements

Several years ago, I decided to transfer from physics to electrical engineering. This thesis may be the milestone, which marks the beginning of my engineer career. Looking back at my entire Ph.D research program, I would like to express my deepest gratitude to my supervisor, Prof. Wei – Ping Huang, for his suggestion to explore the wavelength tunable laser diode modeling/design through advanced laser diode simulation tool development. He also arranged the semiconductor material modeling as my first research topic, which is relatively easier for a physics student to begin with. Therefore I have the opportunity to study both semiconductor material and photonic devices. I would like to thank him not only for his insight guidance and inspiration in the academic research but also for his great assistance to my family and me. I believe that his opinions on the research and life will be the treasures for my future.

My thanks are due to Prof. X. Li for the great help both technically and personally. His excellent advice and concrete support are very important for my Ph.D program. I would also like to convey my thanks to Dr. J. Hong, Dr. C. L. Xu and Mr. Y. Chen for valuable discussions.

I am indebted to Prof. S. Safavi-Naeini, who is my co-supervisor and examination committee member, and the other members of my examination committee, Prof. R. I. Hornsey, Prof. T. Manku, Prof. M. Wartak and the external member Prof. S. - T. Ho from Northwestern University, for their interest in this work and valuable suggestions for the future research projects.

I also appreciate Ontario Graduate Scholarship for financial support.

The last, but not the least, I would like to express my acknowledgement to my wife Mingyu, for her love and continuous encouragement, to my son, Robert, for the fun he brought to my family, to my mother-in-law, for helping us to look after little Robert. I am deeply grateful to my parents, my sister and my brother. Especially I own a lot to my parents for the long lasting understanding on my career development and the suffering of missing their son.

Contents

List of Figures

List of Tables

Chapter 1

Introduction

1.1 Background Review

Semiconductor lasers are key devices in a wide range of applications such as fiber-optical communications, optical disk memory and laser printer due to their attractive features such as small size, low power consumption, fast response and so on [1,11]. In optical fiber communication systems, one of the most important characteristics required for a semiconductor laser is the stable single-mode operation [11], featured by high side-mode-suppression ratio (SMSR) and narrow spectral linewidth. To obtain stable single-mode operation, the distributed feed-back (DFB) [2,3,4] and the distributed Bragg reflector (DBR) [5] lasers were proposed and developed. In these two kinds of lasers, grating structures are utilized as wavelength selective elements. If the grating is in the active region of the laser, where the optical gain occurs, it is referred to as the DFB laser; if the grating is in the passive region, it is called the DBR laser. Examples of typical DFB and DBR lasers are shown schematically in Figure 1.1

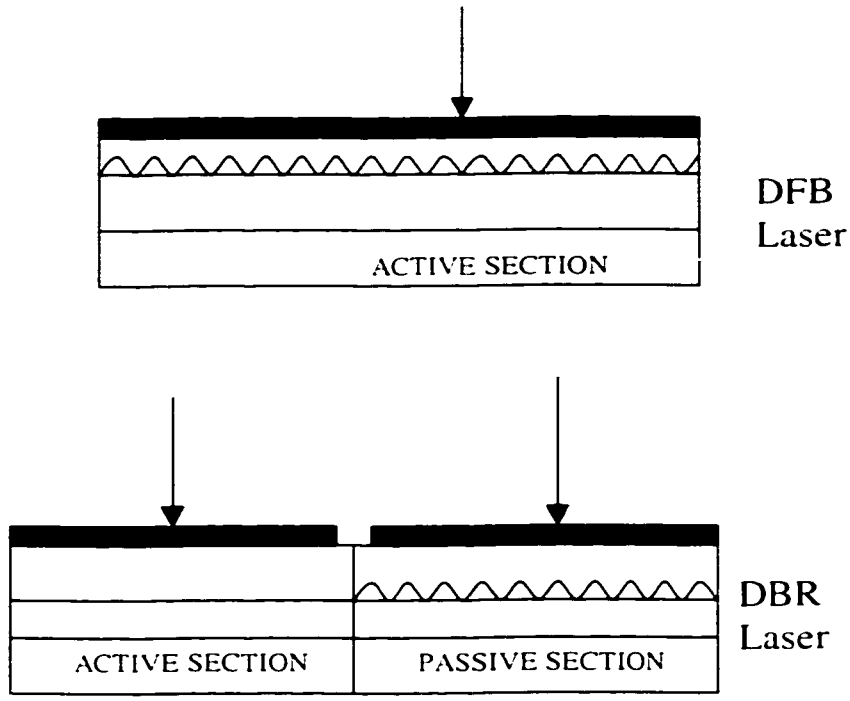

Figure 1. 1 The schematic diagraphs of the DFB and DBR lasers

The development of low-loss glass optical fibers has prompted the research on both bulk and quantum well (QW) InGaAsP/InP materials lasers emitting at $1.3\,\mu m$ and $1.55\,\mu m$. It is mainly due to the fact that the fibers as a light transmission medium have dispersion minimum at $1.3\,\mu m$ and loss minimum at $1.55\,\mu m$ [1.11]. The QW technology can confine electrons in the well region with the thickness less than 200 Å. Therefore, quantum effects such as the quantized energy states occur [15]. When strain is applied to the well region, the relative band structure positions of the heavy holes and the light holes may be changed, so that we can adjust the valence band structures to modify their profiles. The strained QW material lasers have shown lower threshold current, higher differential optical gain, and wider optical gain bandwidth compared with the bulk materials [15]. The QW concept to great extent revolutionizes

the material technology in laser diodes. It also leaves great space for engineers to design and optimize the material composition, well geometry and so on for obtaining required device performance.

To further increase the transmission capacity, frequency division multiplexing (FDM) or wavelength division multiplexing (WDM) techniques have been developed [11]. In the WDM systems, an accurate and stable single-mode wavelength tunable laser is required. Tunable lasers are used in the WDM system for arranging the wavelength of each channel on the sender side. Both discrete [6] and continuous [7,8] wavelength tunable lasers have been proposed and demonstrated experimentally. Some theoretical analyses of wavelength tunable lasers were also reported [9,10]. Since transmission capacity of optical communication system increase monotonically with the number of wavelength channels, there has great effort to extend the tuning range of a semiconductor laser.

As laser fabrication processes are very complicated and expensive, an efficient and relatively accurate simulation tool is in great demand for the laser design and optimization. There are some commonly used laser models such as the power matrix model, the transmission line model and the large signal time domain model (refer to chapter 3). However, to our best knowledge, a comprehensive model, which takes into account of important material, optical, electrical and thermal effects, for wavelength tunable laser is still lacking.

1.2 Objectives and Contributions of the Research

To demonstrate the function of a completed simulation tool, we choose the wavelength tunable DBR laser as example. Normally there are an active laser diode and a passive or functional tunable wavelength selector as shown in Figure 1.1. Wavelength selection and tuning can be achieved by index change associated with free carrier or temperature variation controlled by injection current. In practice, multiple electrodes are usually used to maximize the wavelength tuning range and optimize the overall performance of the devices.

It is obvious that material modeling, which provides the active region optical gain and wavelength selective region refractive index change, is very important in the wavelength tunable laser simulation. In some sense, the accuracy of material models will determine the validity of the device simulation and its application range. However, historically the material simulation and modeling are separated from the semiconductor laser diode simulator, because normally these two kinds of models were developed by two different research groups specialized in solid state physics and semiconductor device engineering, respectively.

Therefore, at first stage, our primary effort was to obtain a comprehensive and accurate models for bulk and QW material optical properties. The modeling refractive index and optical gain depend not only on materials, geometrical and operation parameters, but also on electrical field, temperature and carrier densities. The incorporation of the material models into the wavelength tunable laser simulation is one of the main features in our research.

Secondly, we have developed an efficient laser diode model to include the important features such as spatial hole burning, random spontaneous noise, optical gain saturation and thermal effects. There are two different approaches in the modeling of laser diode, one is the standing wave model, and the other is traveling wave model. In

this dissertation, these two approaches are derived from the same 1D effective optical field equation. Especially, combining these two models, we developed a time domain digital filter approach and incorporated the filter into the traveling wave model to simulate the passive section. This method makes the time domain traveling wave model more versatile and becomes another important feature of our research.
Thirdly we applied the theoretical models to some wavelength tunable laser diode simulation and design. Sample grating assisted tunable lasers provide wide wavelength tuning range. Although there are some qualitative theoretical analysis on these devices [12,13], numerical simulation based on more accurate model concerning the spatial hole burning, random spontaneous noise and so on have not been reported. To meet this challenge and to show the powerfulness of our model, a series of simulations and design issues were presented on this kind of laser diodes.

The last contribution is that our laser simulation tool is used in the design and simulation of multi-section gain coupled DFB laser cascade [14]. The interaction between adjacent sections is investigated. The tuning mechanism and optimized operation parameters are suggested. Especially, unique to this multi-section DFB laser, we also identified conditions for short pulse generation, caused by the beating of the oscillation modes in the composite laser cavity.

In summary, we have developed a comprehensive laser diode model and associated simulation techniques with a number of novel features as a useful addition to the arsenal of tools. The models and simulation techniques have been validated and applied to a number of wavelength tunable laser diodes. We expect that the research results achieved and the future research will not only advance state-of-the-art in modeling and simulation of optoelectronic devices, but also make impact on research and development of some of the devices in real life applications.

1.3 Outline of the Thesis

In chapter 2, general material models for both bulk and QW InP-based compounds are presented. Firstly, we will discuss the complex refractive indices of the intrinsic materials. An inter-band transition model in combination with a fitting procedure is implemented in the models. Secondly, we will present a generalized model for the refractive index change caused by carrier injection, doping, temperature and applied electric field. Finally, optical gain and related refractive index change are discussed. In particular, the QW material gain model is established based on a rigorous strained band structure calculation. Salient features of the strained multiple quantum wells such as negative effective mass of valence band structure, band structure shift due to both compressive and tensile strain effects and optical gain dependence on the TE and TM modes are all accounted for.

In Chapter 3, we will focus on the semiconductor laser diode model with emphasis on the longitudinal cavity configurations. The difference between the traveling wave and the standing wave approaches is clarified and the advantage and limitation of each model are pointed out. For the first time, we incorporate the static and transient thermal effects into the traveling wave model. The improved traveling wave approach is then applied to simulation of several laser diodes. In this chapter, based on the laser model, we also present a theoretical explanation on the various thermal time constants during large signal modulation for a DFB laser diode, which was reported experimentally.

In Chapter 4, we describe further improvement on the traveling wave model of laser diodes. In this respect, we combine the traveling wave model and the standing wave model by introducing a time-domain digital filter, which is suitable for simulation of

optically long laser cavity with both active and passive sections. The model is particularly effective for the long and/or complex passive section cascaded with active laser diode.

In Chapter 5, using the laser model developed in previous chapters, we will investigate sample grating assisted wavelength tunable laser diodes. We divide this chapter into two parts. One is on the DBR type wavelength tunable laser; the other is on the DFB type wavelength tunable laser. For the DFB type laser, we modeled and simulated a sampled-grating DFB laser cascaded with a co-directional filter, which has been to our best knowledge the first rigorous simulation for this kind of complex devices, though there have been some qualitative theoretical analysis already[13].

In Chapter 6, we will present the results for the study of a novel wavelength tunable laser diode, i.e., the multi-section gain coupled DFB laser cascade, invented and demonstrated by our industrial collaborator at Nortel [14]. Firstly, we focus on the two section DFB cascade to investigate the interaction between the two adjacent sections and to design and optimize the key parameters such as the coupling coefficients, the gain coupling ratio. Finally, we extend the design ideas to multi-section case and discuss the tuning mechanisms. In this chapter, we also identify mechanism and conditions for short pulse generation caused by the multi-mode operation nature of this gain coupled DFB cascade.

Finally, in Chapter.7, we summarize the achievements of our research, and present the future research work based on what we have accomplished in this dissertation. To show the building blocks and their relationships of this dissertation more clearly, we draw a schematic organization graph for each of the chapters in Figure 1.2

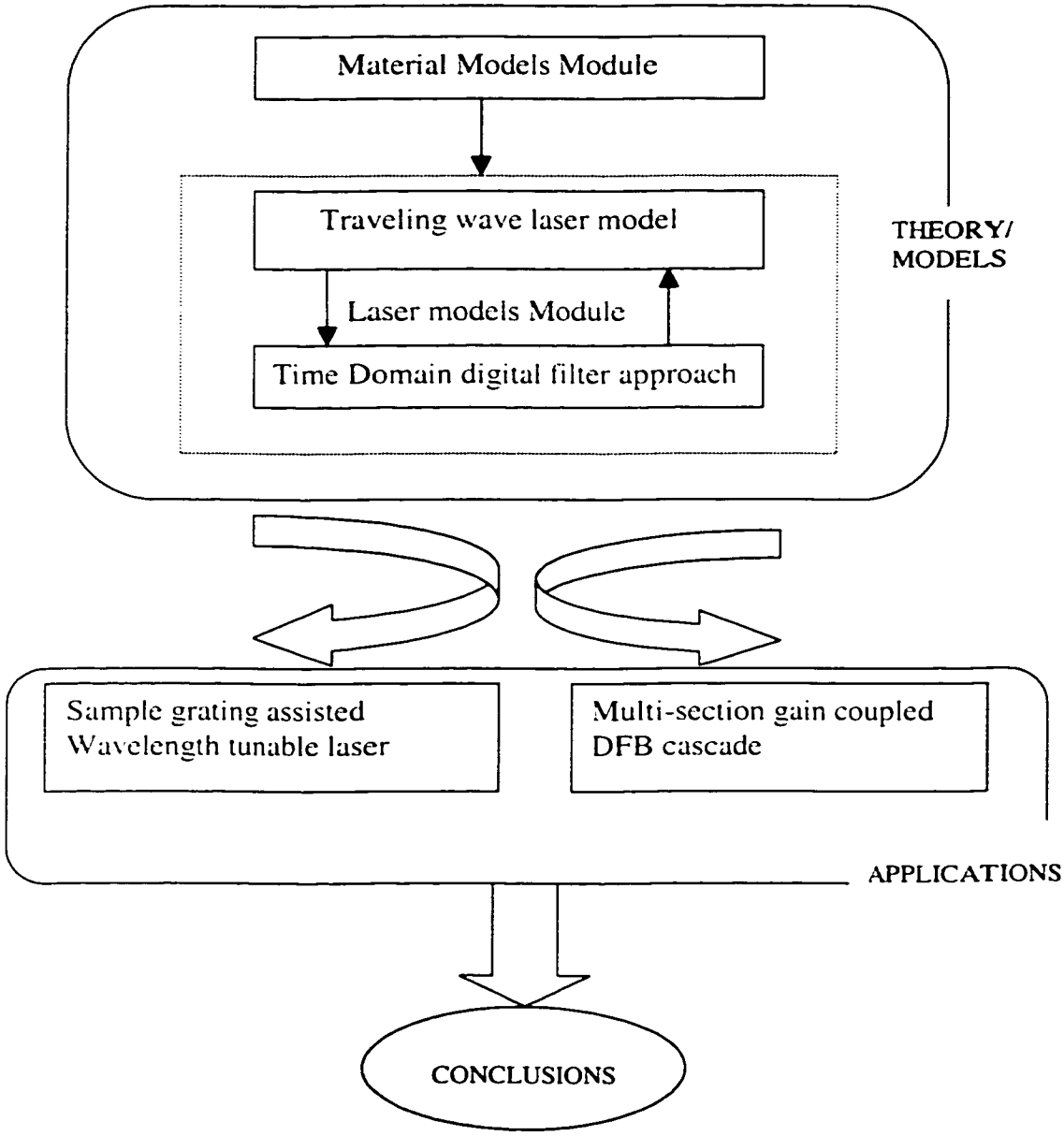

Figure 1.2 Thesis structure

Chapter 2

Modeling and Simulation of Semiconductor Materials

2.1 Introduction

In the simulation of laser diodes, we need first a deep understanding of semiconductor material optical properties. The progress of semiconductor technology is mainly dependent on two families of materials, i.e., group IV elements and III-V compounds [1]. Among them, $In_{1-x}Ga_xAs_yP_{1-y}/InP$ materials, which allow light emission in the wavelength range around 1.3-1.7 μm, becomes the preferred media for realizing optical transmitter in the long haul optical communication. Recently, the semiconductor crystal growth technology make it possible to control the material width and band-gap accurately to confine the electron within an energy potential well,

which is called quantum well (QW) in standard quantum mechanics textbook [3]. With this technology, for the first time, it was demonstrated experimentally that a one-dimensional electron is confined in a box, which is a classical tale in the quantum mechanics theory. It is shown that the QW technology is not only of great academic interest, but also can be used to make very good laser diodes among a variety of other devices.

Although the basic bulk and QW material concepts are well understood, the determination of some important optical parameters requires systematic experimental measurements or theoretical modeling and simulation. Especially, for the sake of simulation of laser diodes, we need a complete knowledge about the optical properties as a function of wavelength, temperature, physical geometry and so on. However, the experimental data are scattered, or at a specific operating condition. Therefore, it is required that through some fitting or optimization procedures, physical modeling and simulation results on one hand should consistent with the known experimental measurements, on the other hand it should predict the material properties for the different operating conditions and wide spectral range. It should be noted that because of the high accuracy required for material modeling, the fitting/optimization procedures seem unavoidable in the simulation. In fact, we do not believe that there exists a general physics-based model, which can provide such accurate results in the material properties simulation. Generally speaking, we should balance our efforts between the physics modeling and numerical fitting procedures. Therefore, in this chapter, we generalize the existing models in the literatures to include thermal, doping, carrier injection and other effects. The models will show good consistency with the limited well-known experimental results and leave some fitting parameters to fit the simulation results to a specific material system fabricated at certain lab. The models only provide a set of prototype functions.

In this chapter, firstly, we will demonstrate a model to describe the intrinsic refractive index of semiconductor material. Then we will discuss the refractive index change due

to doping, thermal and carrier injection for the passive device. Thirdly, we will present optical gain models for the active devices, and especially QW material properties are investigated in detail. The last section is a brief summary.

2.2 Intrinsic Refractive Index

Physically, refractive index profile determines both the lateral optical field distribution and the longitudinal optical wave propagation. Therefore, the knowledge of refractive indices and absorption coefficients of compound semiconductor materials such as $Al_xGa_{1-x}As$ and $In_{1-x}Ga_xAs_yP_{1-y}$ is important for designing semiconductor lasers and wave-guides. The refractive indices and absorption coefficients are the function of material compositions x (Al or Ga composition), y (As composition) and incident photon energy or wavelength. Up to now, measured refractive index data are usually used in the device simulation. However, these experimental data are only available for some specific material composition and incident photon energy. An efficient and accurate theoretical model, which can provide complex refractive index for all material compositions within certain incident photon energy range, is highly desirable. In this section, general models to describe the refractive indices of the intrinsic semiconductor materials, which are at 300K in absence of doping, carrier injection and applied field are developed. In particular, due to its important applications in photonic devices for fiber-optic communications, we focus on the material series $In_{1-x}Ga_xAs_yP_{1-y}$

2.2.1 Bulk Materials

The complex refractive index is defined by

$$\tilde{n} = n(\omega) + jk(\omega) \tag{2.1}$$

where n is the refractive index, and k is the extinction coefficient. They can be obtained from the complex dielectric function $\varepsilon = \varepsilon_1 + j\varepsilon_2$, where ε_1 and ε_2 are related by Kramers-Kronig (KK) relations [1]

$$\begin{aligned} \varepsilon_1 &= 1 + \frac{2}{\pi}\int_0^{\infty} \frac{\omega'\varepsilon_2(\omega')}{(\omega')^2 - \omega^2} d\omega' \\ \varepsilon_2 &= -\frac{2\omega}{\pi}\int_0^{\infty} \frac{\varepsilon_1(\omega')}{(\omega')^2 - \omega^2} d\omega' \end{aligned} \tag{2.2}$$

Once the dielectric function is obtained, the complex refractive index can be calculated from

$$(n + jk)^2 = \varepsilon_1 + j\varepsilon_2 \tag{2.3}$$

There are two kinds of theoretical models for the dielectric function. One is the Harmonic Oscillator Model. This model simulates the dielectric function by [3]

$$\varepsilon = \sum_{m=1}^{N} A_m \left(\frac{1}{E + E_m + j\Gamma_m} - \frac{1}{E - E_m + j\Gamma_m}\right) \tag{2.4}$$

where m is the index of the oscillator, A_m is the amplitude, E is the incident photon energy, E_m is the center energy of oscillator and Γ_m is damping coefficient. By fitting the parameters A_m, E_m and Γ_m to the experimental data, this model can give very accurate refractive index in certain photon energy range [3]. However, it is difficult to

gain a physics insight from this model, and less possible to extend the model to the complicated material systems such as multiple quantum wells (MQW). Another model is the Inter-band Transition Model [4.5.6]. In this model, all possible inter-band transitions are considered for ε_2 calculation and ε_1 is obtained by KK relation. Combining the physics inter-band transition modeling and the fitting procedure, this model is highly successful in producing accurate refractive index for bulk materials. It has been extended to the case of the QW materials. Therefore, the inter-band transition model will be used and further developed in this chapter. However, we suggest that the two kinds of models should be used combatively depending on the application problems.

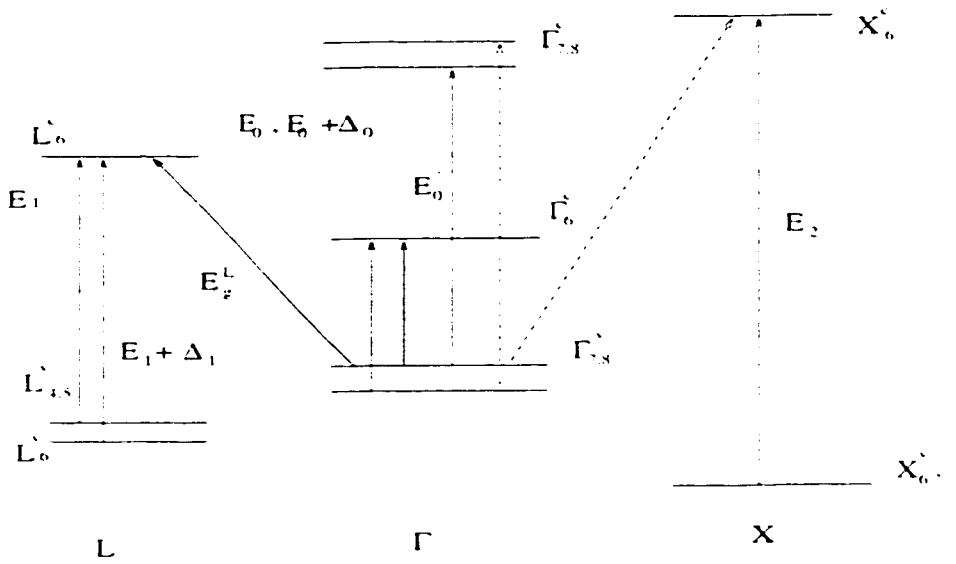

Figure 2. 1 Inter-band transitions considered for the model. The dot-line in the figure is not included.

A comprehensive inter-band transition model has been developed by Adachi [5.6] for $Al_xGa_{1-x}As$ and $In_{1-x}Ga_xAs_yP_{1-y}$ systems. All transitions at three critical points Γ, L (Λ) and X, and indirect transition from L_0^v to Γ_8^v are considered. A schematic description of these transitions is shown in Figure (2.1). It is an accurate and efficient model, but more than ten fitting parameters are required to calibrate the model in order to obtain accurate results in a wide range of material composition and incident photon wavelength. As shown in Figure (2.1), there are several inter-band transitions should be considered in the refractive index modeling. In the following, we will investigate them individually.

(1) E_0 *and* $E_0+\Delta_0$ *transitions*:

This transition occurs in the center of Brillouin zone. The imaginary part of the dielectric constant can be written as [1]

$$\varepsilon_2 = [A/(\hbar\omega)^2][(\hbar\omega - E_0)^{0.5} H(x_0 - 1) + 0.5(\hbar\omega - E_0 - \Delta_0)^{0.5} H(x_{s0} - 1)] \quad (2.5)$$

Using Kramer-Kronig relation, we obtain

$$\varepsilon_1(\omega) = AE_0^{-1.5}\left\{f(x_0) + 0.5[E_0/(E_0+\Delta_0)]^{1.5} f(x_{s0})\right\} \quad (2.6)$$

where

$$\begin{aligned} f(x) &= x^{-2}[2-(1+x)^{0.5} - (1-x)^{0.5} H(1-x)] \\ x_0 &= \hbar\omega / E_0 \\ x_{s0} &= \hbar\omega/(E_0+\Delta_0) \\ H(x) &= \begin{cases} 1 & for\ x \ge 0 \\ 0 & for\ x \le 0 \end{cases} \end{aligned} \quad (2.7)$$

(2) E_1 *and* $E_1 + \Delta_1$ *transitions*

The transitions take place at L point. Their contributions to ε_2 and ε_1 can be simplified as [1]

$$\begin{aligned} \varepsilon_2 &= \pi[B_1 x_1^{-2} H(x_1 - 1) + B_2 x_{1s}^{-2} H(x_{1s} - 1)] \\ \varepsilon_1 &= -B_1 x_1^{-2} \ln(1 - x_1^{\,2}) - B_2 x_{1s}^{-2} \ln(1 - x_{1s}^{\,2} - 1) \end{aligned} \tag{2.8}$$

We notice that this ε_1 exhibits a divergence at E_1 and $E_1 + \Delta_1$ To avoid this divergence, a damping factor is introduced phenomenologically by replacing ω with $\omega + j\Gamma/\hbar$

(3). E'_0 *transitions*:

This transition can be found in Γ point, as shown in Figure (2.1). The imaginary part of dielectric constant is simulated by a damped-harmonic-oscillator model. With the KK relation, we have,

$$\begin{aligned} \varepsilon_2 &= C_s x'_0 \nu / [(1 - x'^{\,2}_0)^2 + x'^{\,2}_0 \gamma^2] \\ \varepsilon_1 &= C_s (1 - x'^{\,2}_0) / [(1 - x'^{\,2}_0)^2 + x'^{\,2}_0 \gamma^2] \end{aligned} \tag{2.9}$$

(4) Indirect-band-gap transition:

The indirect band transitions occur from Γ_8^v to X_6^c and from Γ_8^v to L_6^c as shown in Figure (2.1). We consider only the transition from Γ_8^v to X_6^c, which is dominant. The indirect transition can be described as [5]

$$\begin{aligned} \varepsilon_2 &= \frac{D}{(\hbar\omega)^2}(\hbar\omega - E_g^{id} + \hbar\omega_q)^2 H(1-x_e)H(1-x_t) \\ x_e &= (E_g^{id} - \hbar\omega_q)/\hbar\omega \\ x_t &= \hbar\omega / E_t \end{aligned} \tag{2.10}$$

where E_t is the cut-off energy. In our calculation, we have set $E_t = E_1$. The KK transformation of this term appears to be difficult to obtain analytically. Instead, a constant factor $\varepsilon_{1\infty}$ is introduced to modify the calculated results and fit to the experimental data.

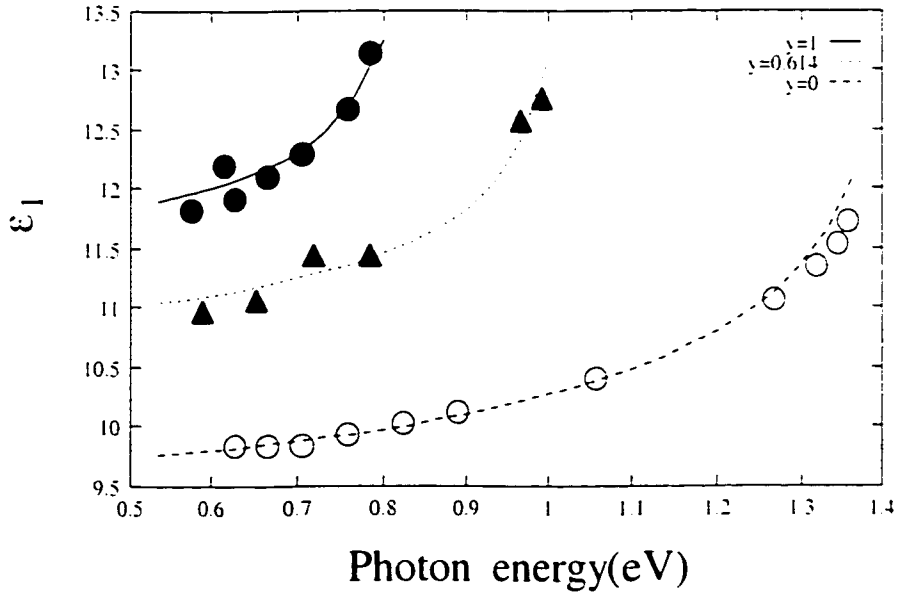

Figure 2. 2 Dielectric coefficient comparison between the simulation results and experimental measurements in [5].

Based on the model developed previously, it is applied to $In_{1-x}Ga_xAs_yP_{1-y}$ material system lattice constant matched to InP. All material parameters needed are list in Table (2.1), and all fitting parameters, which are obtained by fitting the target function to the experimental data of ε_1 and ε_2, are list in Table (2.2).

Table 2. 1 Material Parameters for $In_{1-x}Ga_xAs_yP_{1-y}$ system

Definition	Expression
Ga composition	$x = 0.1894y/(0.4184 - 0.013y)$
Band gap energy (eV)	$E_0 = 1.35 - 0.72y + 0.12y^2$
Spin-orbit splitting (eV)	$\Delta_0 = 0.116 + 0.163y + 0.009y^2$
Band gap at L (eV)	$E_1 = 3.163 - 0.59y + 0.33y^2$
Band gap at L (eV)	$E_1 + \Delta_1 = 3.296 - 0.466y + 0.26y^2$
High band gap at Γ (eV)	$E'_0 = 4.72 - 0.31y - 0.01y^2$
Electron Effective mass	$m_e = (0.08 - 0.039y)m_0$
Heavy hole mass	$m_{h1} = 0.46m_0$
Light hole mass	$m_{h2} = (0.12 - 0.069y)m_0$

Table 2. 2 Fitting parameters for the dielectric function

A(y)	5.402-4.12y
$B_1(y)$	$0.9-3.75y+2.34y^2$
$B_2(y)$	$0.09+2.37y-1.45y^2$
$B_{11}(y)$	$0.33-8.78y+6.22y^2$
$B_{21}(y)$	$1.9B_2$
$\Gamma(y)$	$0.14-0.10y+0.1y^2$
C_s	$1.3+3.7y-2.0y^2$
$\gamma(y)$	$0.093+0.256y-0.124y^2$
D(y)	$60.4-83.2y+43.9y^2$
$\varepsilon_{1\infty}$	2.1 (y < 0.82), 2.8 (0.82<y< 1)

The dielectric function calculated using this model is compared with experimental data as shown in Figure (2.2). The lines are simulation results and dots are measurement data. The model gives very accurate refractive index in a wide range of material composition and photon wavelength.

2.2.2 QW Materials

With the new material growth technologies such as molecular beam eptixy (MBE) and metal organic chemical vapor deposition (MOCVD), it is possible to grow ultra thin layers of semiconductor materials. When the width of the layer is less than 200 $\dot{A}$, electrons will be confined in the well and quantum effect occurs [2]. If the adjacent layers have different lattice constants, there will be strained in the QW. Figure (2.3) shows the quantum well effect, single quantum well, multiple QW, and supper lattice. The QW materials are used widely in the semiconductor lasers active region, and other photogenic wave-guide devices [7]. Therefore, a good understanding of its optical

properties such as gain and refractive index is required. The QW gain will be discussed in the following section. In this section, we just outline the procedure to calculate the refractive index of QW, multiple QW, and super-lattice.

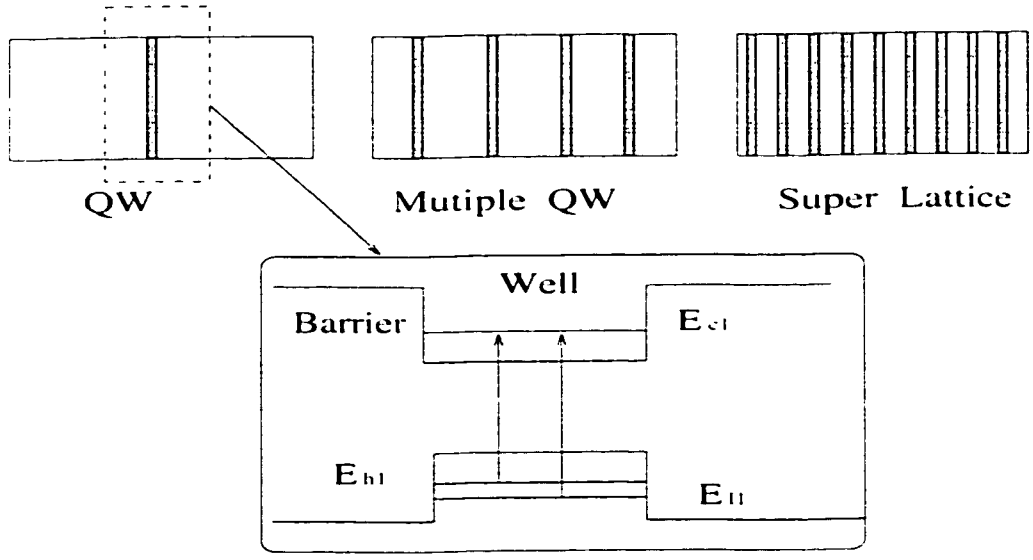

Figure 2. 3 QW, multiple QW and supper lattice

There are so far no well-accepted and adequately validated models to simulate the refractive index of the QW materials. The inter-band transition model is used to calculate the refractive indices in barrier and well regions as show in Figure (2.4). Then an effective refractive index of the QW is defined. For the multiple QW, the refractive index is approximated by [8]

$$\bar{n}^2 = \frac{n_w^2 + n_b^2}{1 + r} \qquad (2.11)$$

where n_w is the refractive index in the well, n_b is the refractive index in the barrier, and r is the ratio of well width and barrier thickness. This model assumes no wave function overlaps between electrons in adjacent wells, and refractive index is divided into well part and barrier part by the quantum well boundary.

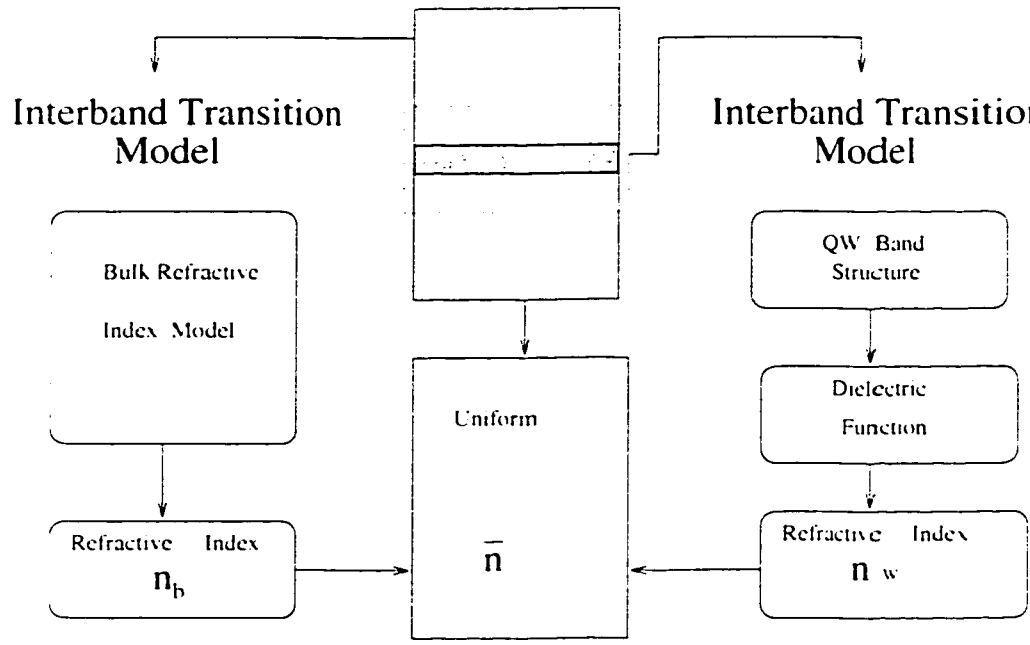

Figure 2. 4 Simulation on the refractive index of QW materials

From Figure (2.4), we can see that this model requires inter-band transition calculations for the QW materials, which is difficult to perform for all critical points. The boundary between well and barrier regions also introduces great conceptual difficulties. Therefore we will not implement this model, but leave the QW refractive index as an empirical value or fitting parameter in the following simulations.

2.3 Change of Refractive Index in Non-radiative Process

Refractive index can be changed by doping, carrier injection, temperature variation and applied electric field. In wavelength tunable laser, the refractive index change in the DBR and the phase control region tunes the reflectivity at the end of active region, and hence makes the semiconductor laser wavelength tunable. The refractive index change is also important in other functional devices such as switches and modulators. In this chapter, a comprehensive model to simulate the bulk refractive index change mechanism is developed, and the simulation results are compared with the experimental data.

For the QW material, a brief description for the corresponding models is given.

2.3.1 Effects of Doping and Carrier Injection

Doping and carrier injection change the refractive index by providing free electrons and holes to the conduction and valence bands. These two effects have the same physical mechanism, hence a general model is given for both effects and the difference between the two effects is explained in the context of the general model.

The free carriers will change the refractive index in three ways, *band-filling*, *bandgap shrinkage* and *plasma absorption* effects[9,10]. Our model is a combination of the works by Bennett *et al* and Weber [9,10].

This is a very simplified model. To include the doping and carrier injection effects, several strength coefficients are fitted to the experimental data. The refractive index changes obtained by this method are reasonably accurate compared with the published experimental data [9].

The change of refractive index induced by free carrier is obtained from [9]:

$$\Delta n = \frac{\hbar c}{\pi}\int_0^{\infty}\frac{\Delta\alpha(E')}{E'^2 - E^2}dE' \qquad (2.12)$$

where $\Delta\alpha$ is the absorption coefficient change associated with the free carrier effect, and E is the incident photon energy.

(1) *Band Gap Shrinkage and Band-filling*

Band shrinkage effects are determined by free carrier density, and are almost independent of impurity concentration. Its mechanism is that when free electron density is large enough, there will be strong repelling interaction among the electrons. The net result is a screening of electrons and a decrease in their energy. The free carrier effect will increase free hole energy. Consequently, the band gap shrinks. It can be modeled by [9]

$$\Delta E_g = -\frac{A}{\varepsilon_1}\left(\frac{N}{N_{cr}} - 1\right)^{1/3} \qquad (2.13)$$

where ε_1 is the dielectric constant we obtain in previous section, N is the larger of free-carrier density of electron or hole, and. N_{cr} is a critical density below which there is no shrinkage, which together with A could be chosen as fitting parameters

The band filling is caused by the free-carrier filling the band to an appreciable depth as shown in Figure (2.5).

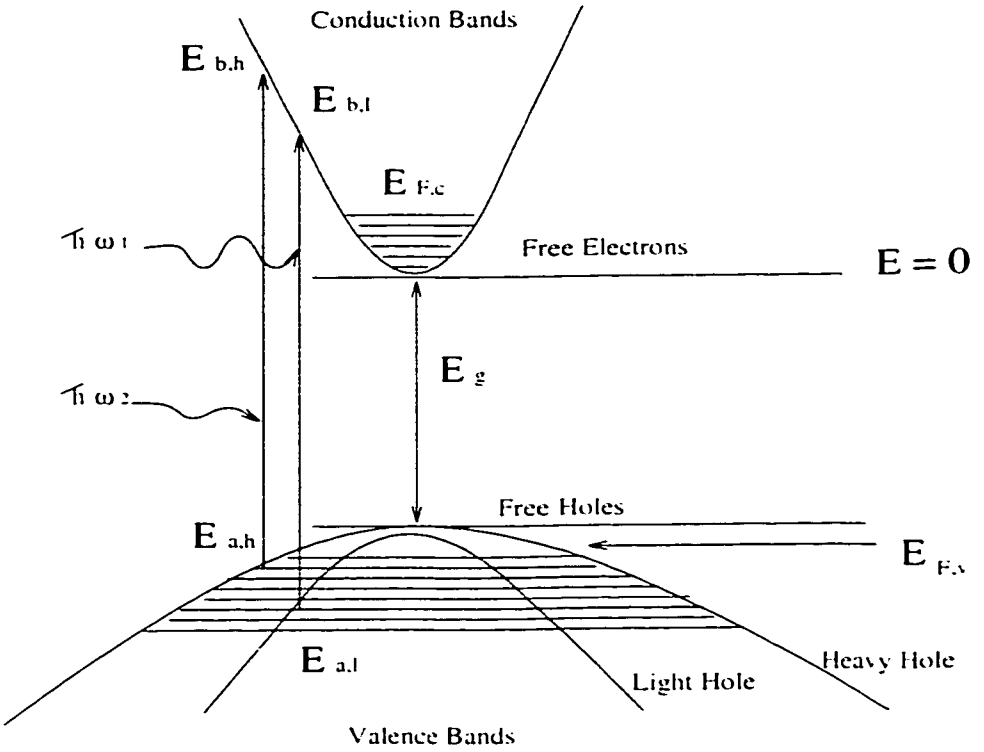

Figure 2. 5 Band filling effects

We will treat the band shrinkage and the band-filling effects together. For a direct band gap with parabolic band structure, if we neglect Urbach tail, the absorption is given by [9]

$$\alpha_0 = \frac{C}{\hbar\omega}\sqrt{\hbar\omega - E_g} \quad \hbar\omega \geq E_g$$
$$\alpha_0 = 0 \quad \hbar\omega \leq E_g \tag{2.14}$$

The constant C depends on the material and could be a fitting parameter.

If we consider the contribution from the light hole and heavy hole, and also the contribution from the band filling and band gap shrinkage, the absorption coefficient is [9]

$$\alpha(\omega) = \frac{C_{hh}}{\hbar\omega}\sqrt{\hbar\omega - E_g}\,[f_v(E_{ah}) - f_c(E_{bh})] + \frac{C_{lh}}{\hbar\omega}\sqrt{\hbar\omega - E_g}\,[f_v(E_{al}) - f_c(E_{bl})] \quad (2.15)$$

where C_{hh} and C_{lh} are the transition strength parameters, which could be fitted to the experimental measurements, and E_a, E_b are hole and electron energy respectively, which involve in the transition. We show these transitions schematically in Figure (2.5). E_a, E_b can be obtained using energy and momentum conservation

$$\begin{aligned} E_{ah,al} &= (E_g - \hbar\omega)\left(\frac{m_c}{m_c + m_{hh,lh}}\right) - E_g \\ E_{bh,bl} &= (E_g - \hbar\omega)\left(\frac{m_{hh,lh}}{m_c + m_{hh,lh}}\right) - E_g \end{aligned} \quad (2.16)$$

The probabilities f_v and f_c in eqn (15) are given by the Fermi-Dirac distribution functions

$$\begin{aligned} f_c(x) &= \{1 + \exp[(x - E_{Fc})/(k_B T)\}^{-1} \\ f_v(x) &= \{1 + \exp[(x - E_{Fv})/(k_B T)\}^{-1} \end{aligned} \quad (2.17)$$

where k_B is Boltzmann constant and T is temperature. E_{Fc} and E_{Fv} are the quasi-Fermi levels, and they are determined by the Nilsson approximation [10]

$$\frac{E_{Fc}}{k_B T} = \ln(\frac{N}{N_c}) + \frac{N}{N_c}[A + B\frac{N}{N_c}(A + \sqrt{\frac{N}{N_c}})]^{-1/4}$$
$$-\frac{E_{Fv} + E_g}{k_B T} = \ln(\frac{P}{P_v}) + \frac{P}{P_v}[A + B\frac{P}{P_v}(A + \sqrt{\frac{P}{P_v}})]^{-1/4} \quad (2.18)$$

Here we choose the zero energy at the conduction band minimum. N and P are the densities of electron and hole respectively. N_c is the effective density of states in the conduction band, and P_v is the effective density of states in the valence band, which are defined by [10]

$$N_c = 2(\frac{m_c k_B T}{2\pi\hbar^2})^{3/2}$$
$$P_v = 2(\frac{m_v k_B T}{2\pi\hbar^2})^{3/2} \quad (2.19)$$
$$m_v = (m_{hh}^{3/2} + m_{lh}^{3/2})^{2/3}$$

We can use eqns (2.14) and (2.15) to get

$$\Delta\alpha = \alpha - \alpha_0 \quad (2.20)$$

and then substitute this result into eqn (2.12) to obtain the refractive index change.
It should be noted that if the free carrier effect is caused by carrier injection, we choose N=P, where the density of free electron and holes are obtained from carrier distribution modeling, and Fermi energy is calculated by Nilsson equations (2.18) and (2.19). On the other hand, in the case of doping, we use the neutral equation to get the carrier density

$$N + N_a^- = P + N_d^+ \quad (2.21)$$

where N_a^- and N_d^- are acceptor and donor ion densities respectively. The quasi Feimi energies for the conduction band and the valence band are the same for the doping case.

(3) The Free-Carrier Absorption

Besides the inter-band absorption, a free carrier can absorb a photon and move to a higher energy state within a band. This absorption is also known as the plasma effect. The corresponding change in refractive index is given by [10]

$$\Delta n = \frac{C}{n(\hbar\omega)^2}\left[\frac{N}{m_{e,0}} + P\left(\frac{m_{hh}^{1/2} + m_{lh}^{1/2}}{m_{hh}^{3/2} + m_{lh}^{3/2}}\right)\right] \qquad (2.22)$$

with energy expressed in eV and N (free electron density) and P (free hole density) in cm^{-3}. For the doping case, another term related to the ions scatting should be added.

(4). General Model

To simulate the doping and carrier injection effect, we consider that plasma effect is a separate effect, but the band filling and the band-gap shrinkage occur jointly, i.e., the free carriers will fill the shrunk band.

As an example, we show the refractive index change caused by carrier injection in Figure (2.6). In the simulation, we did not use any fitting procedures, instead all fitting parameters in the model were calculated by the theoretical model [26]. The comparison with the experimental fitting curve is not perfect but reasonably good. It is shown that carrier injection will cause the decrease of refractive index, normally the maximum relative change is around 0.2%-0.7%.

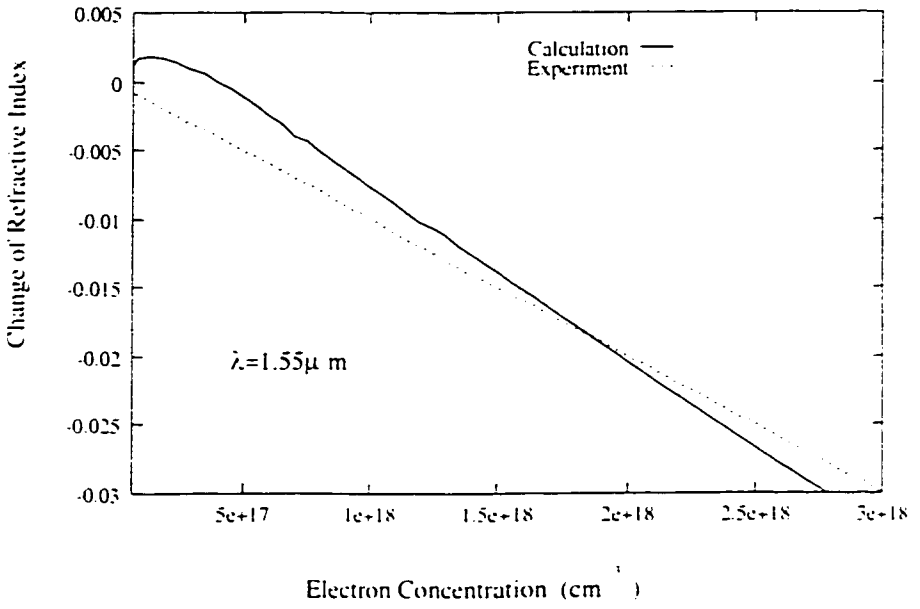

Figure 2. 6 Change of refractive index while energy gap is 0.95 eV. Experimental data is from [10]

2.3 2 Thermal Effects

The temperature change can affect the energy gap of semiconductor compounds as [9]

$$\Delta E_g = (a + b_1 x + c_1 x^2 + b_2 y + c_2 y^2)(T - 300) \qquad (2.23)$$

This change is quite small, we can substitute this result into eqns (2.5) and (2.6) as a perturbation term to obtain the refractive index change. In the case of doping or carrier injection, the thermal effect will also involve in the Fermi-Dirac distribution functions (17). Therefore, the thermal effects in the model are considered in two ways, firstly it changes the band-gap energy; secondly it affects the Fermi-Dirac distribution function.

The second effect is quite small if temperature change is not very large. If there is no doping, we will only apply the inter-band transition model, using the changed band-gap in eqns (2.5) and (2.6) to obtain the refractive index.

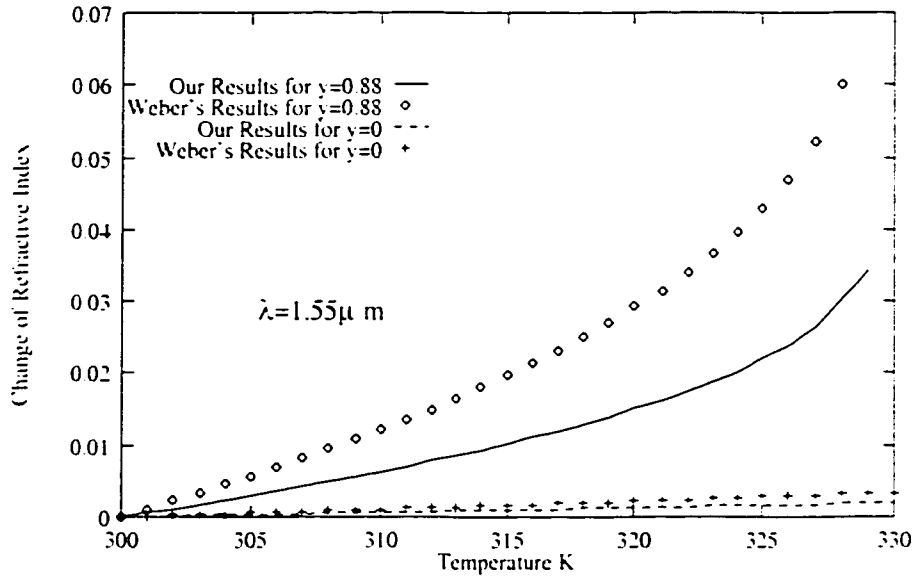

Figure 2. 7 Comparison of the thermal effects with those got by Weber [9]. No fitting procedure is applied in our simulation.

For $In_{1-x}Ga_xAs_yP_{1-y}$ material system, still without fitting procedure, we choose a=-3.18, b_2=0.41 and c_2=-0.61, which are commonly used parameters [26]. The thermal effects are compared with the theoretical results given by Weber as shown in Figure (2.7). Our results qualitatively are the same as Weber's when the photon energy is much smaller than the energy gap of the semiconductor. When photon energy is approaching the energy gap, there is considerable difference between the two models. Weber's

model is only valid when the photon energy is far below the energy gap. It is not apparent in what range this model is valid. Therefore, the discrepancy between the two models is still to be investigated. It is shown that thermal effect will increase the refractive index.

2.3.3 The Effect of Electric Field

Strong electric field affects the refractive index of semiconductor in two ways, one via the electro-optic effect, which is also known as Pockels effect. It is a well-established linear relation between the refractive index change and applied electric field [26]. The other is via electro-refraction, which is also known as Franz-Keldysh effect. We will give a theoretical model for Franz-Keldysh effect in this section.

Electro-refraction is the refractive index change induced by Franz-Keldysh electro-absorption effect. When an electric field is applied, the band edges are tilted, and hence the optical absorption is changed.

Using the weak-field approximation, the absorption coefficient $\alpha(F)$ in the presence of an electric field F, is [11]:

$$\alpha(F) = \sum_i A_i F^{1/3} [|(\frac{d\mathrm{Ai}(z)}{dz})_{\beta_i}|^2 - \beta_i |\mathrm{Ai}(\beta_i)|^2] \qquad (2.24)$$

where the sum is over the heavy and light holes, Ai is the Airy function [12].

In eqn (2.24), the coefficient β_i is

$$\beta_i = B_i (E_g - \hbar\omega) F^{-2/3} \qquad (2.25)$$

A_i, B_i in eqns (2.24) and (2.25) are the fitting parameters.

As F goes to zero, eqn (2.24) changes into the familiar expression for the absorption coefficient due to direct allowed transition.

To calculate the refractive index change induced by the electric field, KK relation is used as shown in eqn (2.12)

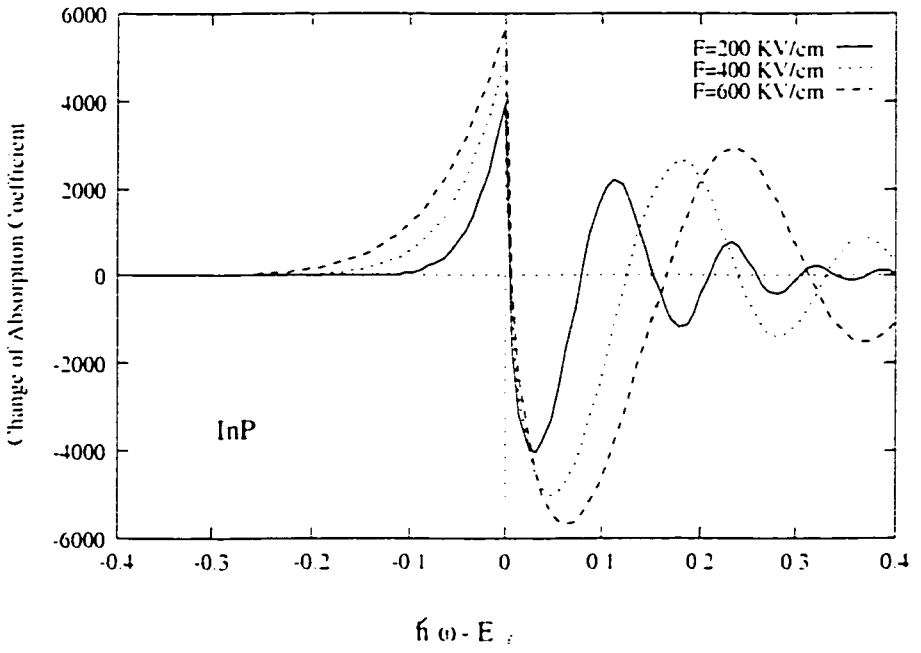

Figure 2. 8 Change of absorption coefficient of InP at different electric field.

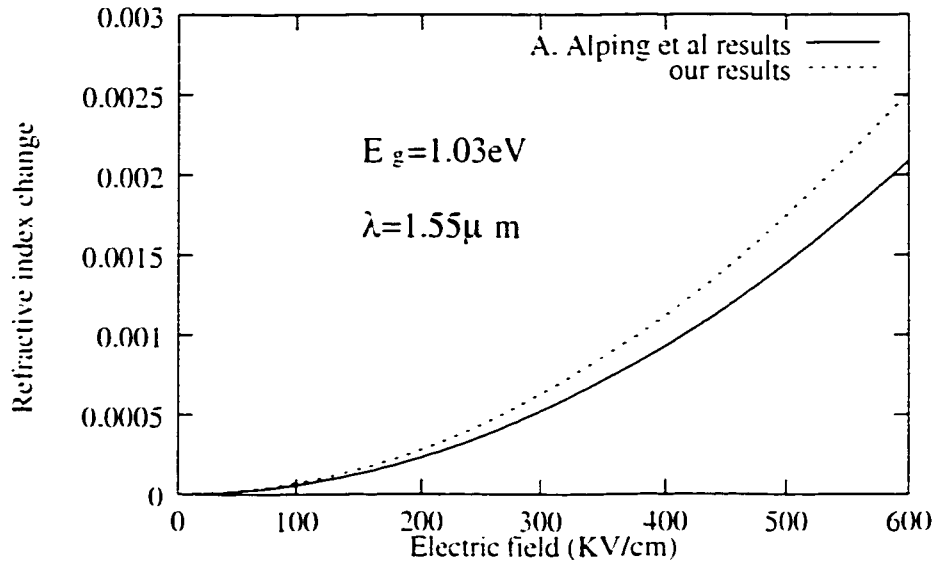

Figure 2. 9 Comparison of the change of refractive index of InGaAsP compounds with that got by Alping and Coldren

As an example, we will show the electro-refraction of $In_{1-x}Ga_xAs_yP_{1-y}$ system. Instead of using the fitting procedure, all parameters are obtained from theoretical calculation [26]. The absorption change $\Delta\alpha$ as a function of photon energy is shown in Figure (2.8). We compare our results at wavelength 1.55μm with those obtained by Alping and Coldren in Figure (2.9). Their results are expressed empirically in the form

$$\Delta n = 5.8\times10^{-15} F^2 (cm^2 V^{-2})$$

We can see that our results are in the same range as their empirical data.

2.4 Change of Refractive Index in Radiative Process: Optical Gain

In the active region, recombining carriers contribute to optical gain and photon emission. If the carrier injection density is sufficient high, the difference between the quasi-Fermi levels of conduction band and valence band will be greater than the incident photon energy. Under this condition, it can be shown that the optical gain will occur [13]. This phenomenon is the main mechanism of semi-conductor lasers. Therefore accurate and efficient models to simulate both bulk and QW materials are important topics. In this chapter, optical gain models for both bulk and QW materials are developed.

2.4.1 Bulk Material Model

Optical gain and the associated index change in bulk material have been investigated extensively, and there are well-established theoretical models available [13]. For a bulk material, there are analytical forms for density of state and band structure. Optical gain can be expressed as [13]

$$g(\omega) = \frac{\pi c^2 \hbar}{4\varepsilon_0 n_b^2 \omega^2} \int_0^{\hbar\omega - E_g} B(E)\rho_c(E)\rho_v(E')[f_c(E - E_{F_c}) - f_v(E_v - E')]dE \quad (2.26)$$

$$\begin{aligned} B(E) &= \frac{4\pi n_b e^2 \omega}{m_0^2 \varepsilon_0 \hbar c^3} |M_b|^2 |M_{cv}(E)|^2 V \\ E' &= \hbar\omega - E - E_g \end{aligned} \quad (2.27)$$

$M_b M_{env}(E)$ is called Stern's matrix element. M_b is the Bloch averaged dipole matrix, to which we will give an analytical form in the next section. The carrier injection results in the band tail effect, which can be simulated by the Halperin-Lax band tails model [13]. The band tails will change the densities of state ρ_c, ρ_v and "enveloped" function matrix element M_{env}. To calculate Stern's matrix element, a Gaussian fitting to the Halperin-Lax band tails is performed. This model is known as GHLBT-SME model [13]. In Figure (2.10), the comparisons between model simulations and the experimental measurements are shown for InGaAsP materials. The refractive index change associated with the optical gain can be obtained by KK relation. Since bulk material gain simulation is much easier than that of MQW, the theoretical details will be explained in the next section

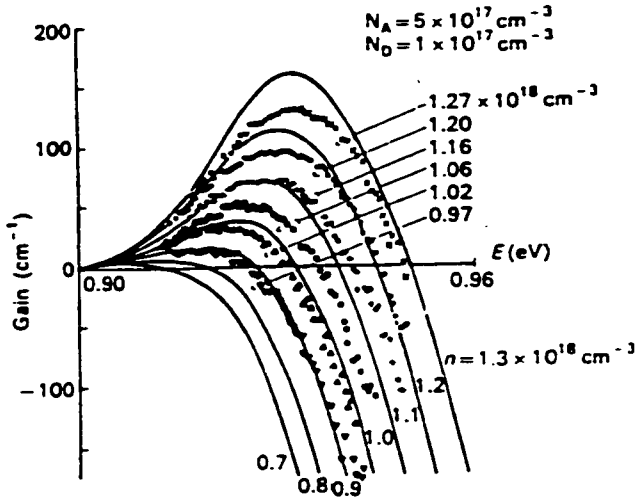

Figure 2.10 Comparison of the Gain profiles calculated by GHLBT-SME model (line) and those measured by experiments (dots) [27].

2.4.2 QW Material Model

The ability to fabricate QW and MQW structures has given rise to new optical and electronic devices. Quantum well technology makes it possible to control the depth, range and the arrangement of quantum well in the semiconductors. Since the first investigation of optical properties in quantum wells by Dingle *et al* [2], the application of quantum well structures to semiconductor lasers has received considerable attention for its superior characteristics, such as low threshold current density, low temperature dependence of threshold current, lasing wavelength tunability, and excellent dynamic properties [2]. It was suggested that the introduction of strain into the crystal lattice of a semiconductor material could help equalize the density of states in the conduction and valence bands, reducing transparency levels, as well as increasing the differential gain of the materials [14,15]. There has been great interest in the study of strained quantum well systems.

In this section, a theoretical analysis of quantum well band structures is presented. In our treatment, the strain effect is incorporated into the Hamiltonian naturally, and non-strain quantum well band structure is just a special case in our calculation. Quantum well gain and reflective index change are also modeled based on the band structures.

Quantum Well Band Structures

Historically, the calculation of quantum well sub-band structure has taken two different approaches. In the first approach, a single-band effective mass model is assumed and valence bands mixing effect between the valence sub-bands is ignored [16,17]. The advantage of this approach is that parabolic bands are obtained and simple analytical expression can be derived for the Fermi energy and quantum well gain calculations. With some approximation, this model even can solve the problem of strained quantum well. However, this approach assumes that the quantum well valence sub-bands are parabolic and isotropic. Consequently, many important features such as negative effective mass, band mixing are not accounted for. The second approach involves solving 4×4, 6×6, or 8×8 Hamiltonian of Luttinger-Kohn type [18,19], and imposes an enveloped function approximation in solving the quantum well sub-band structures. The valence bands obtained from this approach show complicated structure unique to quantum well material. It seems difficult to obtain simple analytical solutions in this approach. On the other hand, efficient numerical approach has to be used for the band structure calculation. In our calculation, we will use the second approach.

(1) Luttinger-Kohn Hamiltonian

The typical non-strain semiconductor band structure is shown in Figure (2.11).

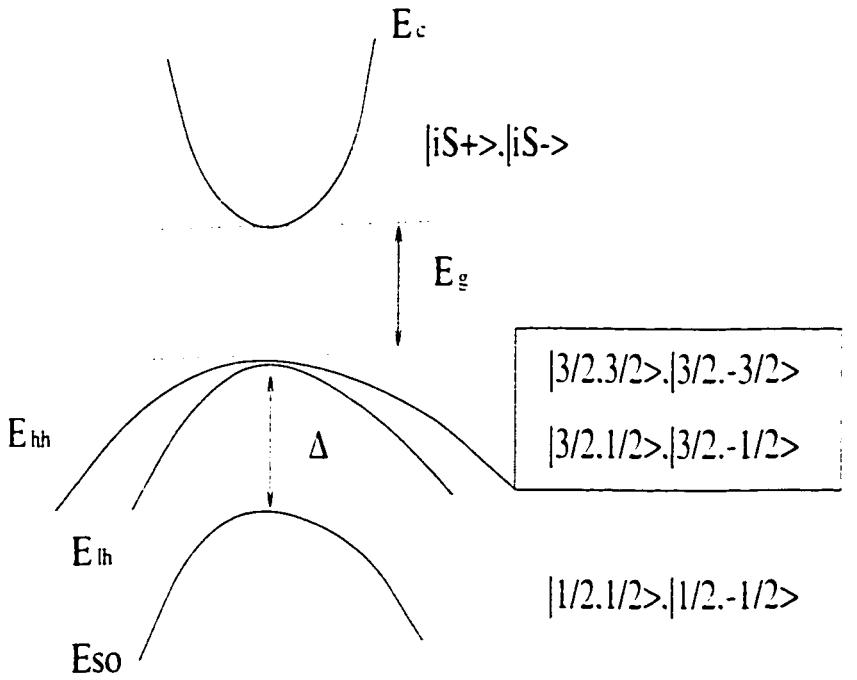

Figure 2. 11 Band edge Bloch functions and band energy.

If the spin split-off bands energy Δ and energy gap E_g are much larger than the energy separation between the heavy hole and light hole, we can use 4×4 Luttinger-Kohn Hamiltonian to solve this problem. The Hamiltonian is in the form [18]

$$H = -\begin{bmatrix} P_t + Q_t & -S_t & R_t & 0 \\ -S_t^* & P_t - Q_t & 0 & R_t \\ R_t^* & 0 & P_t - Q_t & S_t \\ 0 & R_t^* & S_t^* & P_t + Q_t \end{bmatrix} \tag{2.28}$$

where the base of Hamiltonian are $|\frac{3}{2},\frac{3}{2}>,|\frac{3}{2},\frac{1}{2}>,|\frac{3}{2},-\frac{1}{2}>,|\frac{3}{2},-\frac{3}{2}>$, and

$$\begin{aligned} P_t &= P + P_\varepsilon \\ Q_t &= Q + Q_\varepsilon \\ R_t &= R + R_\varepsilon \\ S_t &= S + S_\varepsilon \end{aligned} \tag{2.29}$$

The explicit expressions for the above matrix elements are

$$\begin{aligned} P &= [\hbar^2\gamma_1/(2m_0)](k_x^2 + k_y^2 + k_z^2) \\ Q &= [\hbar^2\gamma_2/(2m_0)](k_x^2 + k_y^2 - 2k_z^2) \\ R &= -[\hbar^2\gamma_2/(2m_0)]\sqrt{3}(k_x^2 - k_y^2) + j[\hbar^2\gamma_3/(2m_0)]2\sqrt{3}k_x k_y \\ S &= [\hbar^2\gamma_3/(2m_0)]2\sqrt{3}(k_x - k_y)k_z \end{aligned} \tag{2.30}$$

$$\begin{aligned} P_\varepsilon &= a_v(\varepsilon_{xx} + \varepsilon_{yy} + \varepsilon_{zz}) \\ Q_\varepsilon &= -3/2b(\varepsilon_{xx} + \varepsilon_{yy} + \varepsilon_{zz}) \\ R_\varepsilon &= \sqrt{3}b/2(\varepsilon_{xx} - \varepsilon_{yy}) - jd/2\varepsilon_{xy} \\ S_\varepsilon &= -\sqrt{3}d(\varepsilon_{xx} - j\varepsilon_{xz}) \end{aligned} \tag{2.31}$$

where a_v, b and d are potential parameters.

For the strained-lattice case, if base material lattice constant is a_0, and strained lattice constant is a^*, we have

$$\varepsilon_{xx} = \varepsilon_{yy} = \frac{a_0 - a'}{a_0} = \varepsilon$$
$$\varepsilon_{zz} = -2\frac{C_{12}}{C_{11}}\varepsilon \qquad (2.32)$$
$$\varepsilon_{xy} = \varepsilon_{yz} = \varepsilon_{zx} = 0$$

where C_{12} and C_{11} are elastic constants for the crystal. An unitary transformation to the Hamiltonian was introduced by Chuang [18]. The transformation changes the Hamiltonian into a block-diagonal form.

$$H = \begin{bmatrix} H^U & 0 \\ 0 & H^L \end{bmatrix} \qquad (2.33)$$

where

$$H^U = -\begin{bmatrix} P+Q+\zeta & \tilde{R} \\ \tilde{R}^* & P-Q-\zeta \end{bmatrix} + \frac{1}{3}\delta E_{so}$$
$$H^L = -\begin{bmatrix} P-Q-\zeta & \tilde{R} \\ \tilde{R}^* & P+Q+\zeta \end{bmatrix} + \frac{1}{3}\delta E_{so} \qquad (2.34)$$

The base of this Hamiltonian are |1>, |2>, |3>, and |4>. They are linear combination of the original base and can be easily obtained from the unitary transform matrix. |1> and |4> are linear combination of the two heavy hole base, and |2> and |3> are linear combination of the two light hole base.

The conduction-band Hamiltonian is given by

$$H_c = \frac{\hbar^2}{2m_c}(k_x^2 + k_y^2 + k_z^2) - \frac{2}{3}\delta E_{so} \qquad (2.35)$$

In eqns (2.34) and (2.35) , we have used the relations

$$
\begin{aligned}
a &= (C_1 + a_1) \\
\delta E_{hh} &= -2a[1 - \frac{C_{12}}{C_{11}}]\varepsilon \\
\delta E_{lh} &= -2b[1 + \frac{C_{12}}{C_{11}}]\varepsilon \\
\varsigma &= \frac{1}{2}\delta E_{lh} \\
\tilde{R} &= |R| - j|S|
\end{aligned}
\tag{2.36}
$$

Here we also have made the assumption $C_1=2/3a$.

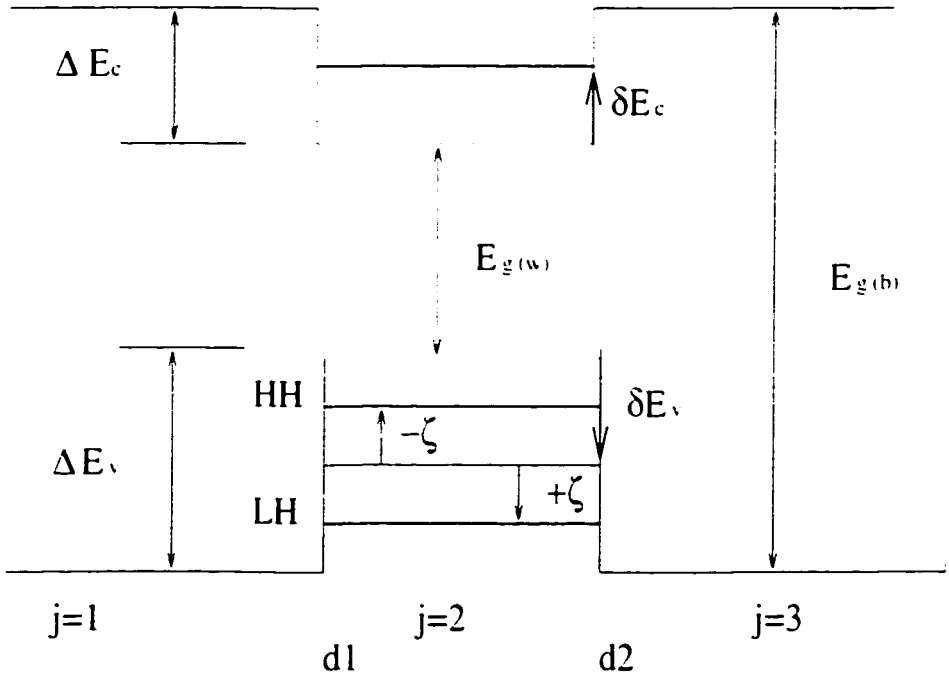

Figure 2. 12 Energy shift after strain is applied (compressive strain in this case).

The valence band Hamiltonian H^U and H^L give a degenerate energy. Therefore, only one of them, for example H^U, needs to be solved. The conduction band Hamiltonian remains a parabolic one, and easy to be solved. Figure (2.12) shows the quantum well potential shift after the strain is applied.

(2). Valence Band Structure

For a strained quantum well, the Hamiltonian is eqn (2.34). In the barrier region, the potential is ΔE_v. Here we use the model $\Delta E_v = 0.64\Delta E_g$, where ΔE_g is the band gap discontinuity between the well and barrier regions. The strain potential ΔE_{vh} and ΔE_{lh} are zero in the barrier.

For the special case of $k_t = 0$, i.e., $k_x = k_y = 0$, we find that $\tilde{R} = 0$, so that the Hamiltonian is a diagonal one. The eigenfunctions are |1> and |2> respectively, i.e., heavy hole and light hole are totally decoupled.

We will show later, in the case of $k_t \neq 0$, the eigenfunction will be the mixing states of |1> and |2>. The concept "heavy hole" band or "light hole" band mean the state when $k_t = 0$. If the effective mass approximation is used, the calculation will be based on the assumption that there is no band mixing even when $k_t \neq 0$. We will show that this assumption is no longer valid in the case of strained quantum wells. Since the Hamiltonian is diagonal when $k_t = 0$, we can solve the heavy hole and light hole separately. For heavy hole in the j region [see Figure (2.12)], we have the wave function

$$\psi^j = A_{hh_j}\begin{bmatrix}1\\0\end{bmatrix}\exp[jk_{zj}^{hh}(z-d_j)] + B_{hh_j}\begin{bmatrix}1\\0\end{bmatrix}\exp[-jk_{zj}^{hh}(z-d_j)] \qquad (2.37)$$

By using the boundary condition, we can find a transmission matrix

$$\begin{bmatrix} A_{HH_j} \\ B_{HH_j} \end{bmatrix} = U_{j(j-1)} = \begin{bmatrix} A_{HH(j-1)} \\ B_{HH(j-1)} \end{bmatrix} \tag{2.38}$$

where $U_{j(j-1)}$ is a 2×2 matrix defined by

$$U_{j(j-1)} = \frac{1}{2}\begin{bmatrix} 1+p_{j(j-1)} & 1-p_{j(j-1)} \\ 1-p_{j(j-1)} & 1+p_{j(j-1)} \end{bmatrix}\begin{bmatrix} \exp(-jk_{(j-1)z}l_{j-1}) & 0 \\ 0 & \exp(jk_{(j-1)z}l_{j-1}) \end{bmatrix} \tag{2.39}$$

where l_j is the length of the j section in the well, and

$$p_{j(j-1)} = \frac{m_j k_{(j-1)z}}{m_{j-1}k_{jz}} \tag{2.40}$$

where m_j is the effective mass of the j section at $k_t = 0$ point. For heavy hole, the effective mass is given as

$$m_j = \frac{m}{\gamma_1 - 2\gamma_2} \tag{2.41}$$

and for the light hole

$$m_j = \frac{m}{\gamma_1 + 2\gamma_2} \tag{2.42}$$

For a single quantum well, we have

$$\begin{bmatrix} A_{HH1} \\ B_{HH1} \end{bmatrix} = U_T = U_{12}U_{23} = \begin{bmatrix} u_{11} & u_{12} \\ u_{21} & u_{22} \end{bmatrix} \begin{bmatrix} A_{HH3} \\ B_{HH3} \end{bmatrix} \tag{2.43}$$

If choose $\mathrm{Im}(k_{z1,3}) > 0$, for the bound state, we will have $A_{HH1} = 0$, and $B_{HH3} = 0$. Consequently, the element u_{11} in the matrix U_T is zero. Using the root searching method, we can find the energy of the quantum well system, i.e., searching the roots of equation $u_{11}(E_m) = 0$.

For the case $k_t \neq 0$, the calculation will be more complicated. We can express the wave function in the form

$$\begin{aligned} \psi^j = & A_{HHj} \begin{bmatrix} F^j_{1HH} \\ F^j_{2HH} \end{bmatrix} \exp[jk^{HH}_{zj}(z - d_j)] + B_{HHj} \begin{bmatrix} F^{j-}_{1HH} \\ F^{j-}_{2HH} \end{bmatrix} \exp[-jk^{HH}_{zj}(z - d_j)] + \\ & A_{LHj} \begin{bmatrix} F^j_{1LH} \\ F^j_{2LH} \end{bmatrix} \exp[jk^{LH}_{zj}(z - d_j)] + B_{LHj} \begin{bmatrix} F^{j-}_{1LH} \\ F^{j-}_{2LH} \end{bmatrix} \exp[-jk^{LH}_{zj}(z - d_j)] \end{aligned} \tag{2.44}$$

In every region, the wave function is a combination of four linear independent solutions of Hamiltonian (2.34). Using the boundary conditions, i.e., (1). the wave function is continuous; 2. the probability stream is continuous, we can obtain the transmission matrix in the form

$$M_j = \begin{bmatrix} A_{HHj} \\ A_{LHj} \\ B_{HHj} \\ B_{LHj} \end{bmatrix} = M_{j+1} P_{j+1} \begin{bmatrix} A_{HH(j+1)} \\ A_{LH(j+1)} \\ B_{HH(j+1)} \\ B_{LH(j+1)} \end{bmatrix} \tag{2.45}$$

where $M_{j,j+1}, P_{j+1}$ are both 4×4 matrix, with the elements related to k_{jz}^{HH}, k_{jz}^{LH}, and Luttinger parameters. For a single quantum well, the bound state will have the form

$$\begin{bmatrix} 0 \\ 0 \\ B_{HH1} \\ B_{LH1} \end{bmatrix} = (M_1^{-1}M_2P_2)(M_2^{-1}M_3P_3)\begin{bmatrix} A_{HH3} \\ A_{LH3} \\ 0 \\ 0 \end{bmatrix} \qquad (2.46)$$

We define the transmission matrix

$$U = (M_1^{-1}M_2P_2)(M_2^{-1}M_3P_3) = \begin{bmatrix} U_1 & U_2 \\ U_3 & U_4 \end{bmatrix} \qquad (2.47)$$

where U_1, U_2, U_3 and U_4 are all 2×2 matrix. From eqns (2.46) and (2.47), we have $\det|U_1|=0$. By searching the roots of equation $\det|U_1(E_m)| = 0$, the energy of the quantum well system can be found. It is clear that there is strong sub-band mixing effect while $k_t \neq 0$.

To calculate the valence band structure, first we set $k_t=0$ to obtain the energy level of the heavy hole and the light hole. By changing k_t with small steps, the entire band structure can be calculated by the same procedure. Figures (2.13-2.15) show the band structures calculated by this method. The band structures include compressive, no-strain and tensile strain cases. It is shown that the band structures are not parabolic, for example, negative effective mass may appear due to the existence of the strain; and stain effect can change the relative position of the heavy hole and light hole dramatically.

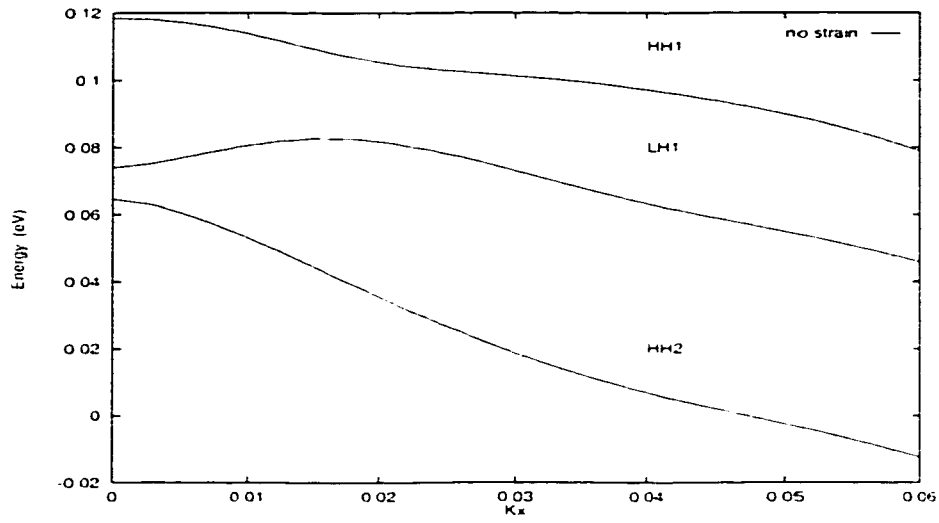

Figure 2. 13 Valence band structure while no strain applied.

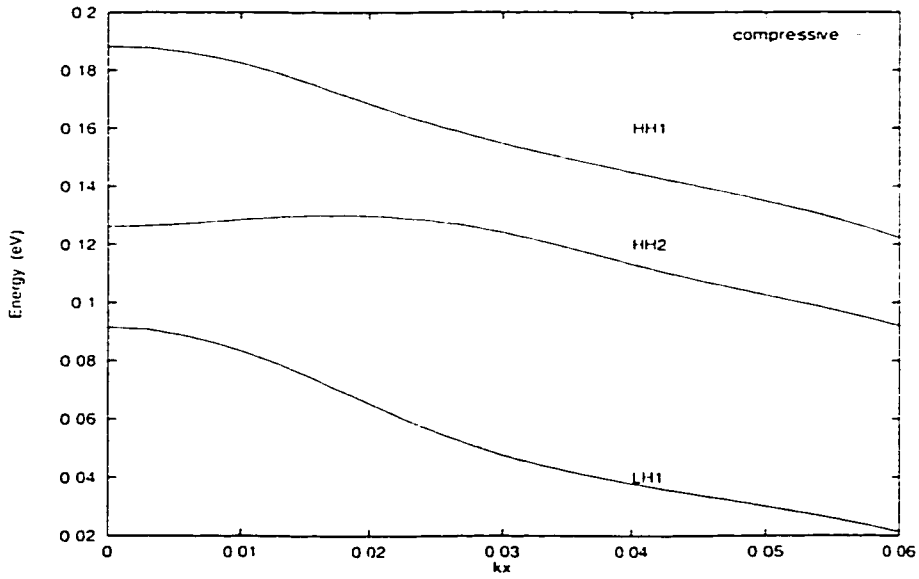

Figure 2. 14 Valence band structure with compressive strain.

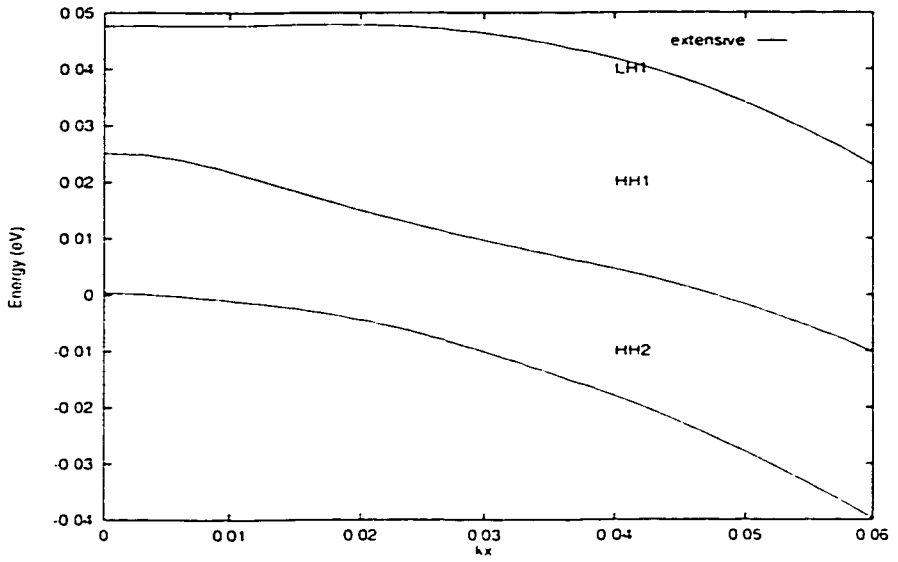

Figure 2. 15 Valence band structure with tensile strain

QW Gain Modeling

As free carriers are injected into the QW material, the free electrons will fill the quantized parabolic conduction bands, and the free holes will fill the complicated valence bands, which have been shown in the previous section. When the free carrier density is sufficient high, if the incident photon energy is smaller than the difference between the quasi-Fermi energies of conduction band and valence band, the optical gain occurs. Since QW material has multi-quantized energy levels, multi-peaks may be found in the gain spectrum. Due to the anisotropy structure of QW materials, TE and TM modes have different gain features. To make the modeling more efficient, we begin with the electronic susceptivity calculation. This model can give both the optical gain the refractive index change [20].

(1). Fermi Level

If the band structure is parabolic, Fermi energy will be very easy to calculate. For a given injected electron density N, which is usually determined by the injection current and could be obtained from carrier rate equation. The quasi-Fermi level F_t for electron can be calculated by [21]

$$N = \sum_n N_n = \sum_n \int dE \rho_c^{2D}(E) f_t^n(E) \tag{2.48}$$

where the sum is over all the occupied bands, $\rho_c^{2D}(E)$ and $f_t^n(E)$ are two dimensional density of state and Fermi function, respectively. If the band structure is parabolic, for example the band structure of conduction band, we have

$$f_t^n = \frac{1}{\exp[(E_{cn} + \hbar^2 k_t^2 / 2m_t - F_t)/(k_B T)] + 1} \tag{2.49}$$

where E_{cn} is the n band bottom energy at $k_t=0$ and

$$\rho_c^{2D} = \frac{m_t}{\pi \hbar^2 L_z} \tag{2.50}$$

where L_z is the width of quantum well. We have derived an analytical formula for the carrier density

$$N_n = \frac{m_c k_B T}{\pi \hbar^2 L_z} \ln\left(1 + \exp[(F_c - E_{cn})/(k_B T)]\right) \qquad (2.51)$$

From this equation, Fermi level can be easily calculated if the electron density is known. Figure (2.16) shows the schematic picture of the density of state, and electron distribution of parabolic band structure.

However, if the valence band structure is not a parabolic as in the case of valence bands of QW material, we can not use the analytical formula to obtain the quasi-Fermi level of the valence band. Instead, all the states are summed to yield the total hole density as

$$P_m = \frac{2}{V} \sum_{k_t} [1 - f_v^m(k_t)] \qquad (2.52)$$

Here m is the index of sub-band, and the number 2 accounts for the degeneracy of H^{U} and H^{L} mentioned before. We also have

$$f_v^m = \frac{1}{\exp[(E_{vm}(k_t) - F_v)/(k_B T)] + 1} \qquad (2.53)$$

where $E_{vm}(k_t)$ is the dispersion band energy function obtained numerically from the last section. Numerical method is used to calculate the quasi-Fermi level of valence band by

$$P = \sum_m P_m = \sum_m \frac{2}{V} [1 - f_v^m(k_t)] \qquad (2.54)$$

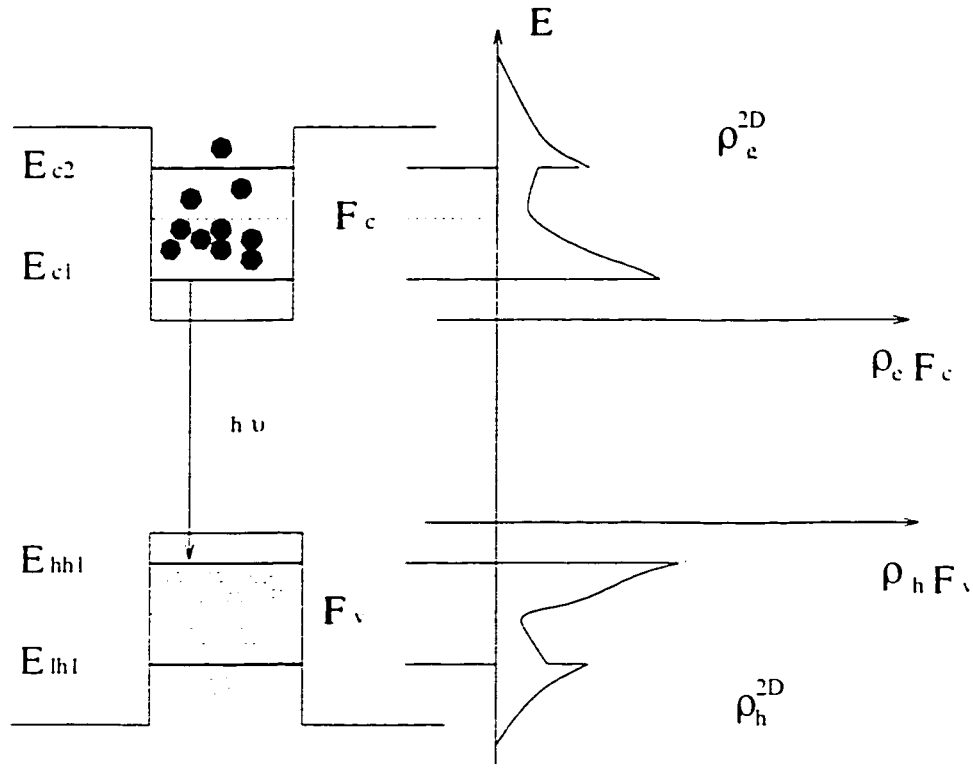

Figure 2. 16 Density of state of QW material and carrier distribution.

(2) Gain and Refractive Index Change

After all sub-band levels are known, the linear susceptibility $\chi(\omega)$ can be obtained by using density matrix formalism [22]

$$\varepsilon_0 \chi(\omega) = \frac{1}{V} \sum_{\sigma} \sum_{\eta} \sum_{m} \sum_{n} \sum_{k_t} |\hat{e} \cdot \vec{M}_{mn}^{cv}(k_t)|^2 \frac{f_c^m - f_{v,\sigma}^n}{E_{cm}(k_t) - E_{vn}^{\sigma} + E_g - \hbar\omega - j\hbar/\tau} \quad (2.55)$$

where σ denotes the upper and lower blocks of the valence band Hamiltonian, and η is the electron spin state. Parameters m and n are the indices for the sub-bands of conduction bands and the valence bands. Vector $\hat{e}$ is the polarization vector of the vector field. $\bar{M}_{mn}^{\sigma\eta}(k_t)$ is the optical dipole matrix between the m conduction band with spin η and the n valence sub-band with upper and lower block index σ. The functions f_t^m and $f_{v,\sigma}^n$ are Fermi functions as defined before. E_g is the band gap energy *after the strained is applied*; τ is the intra-band relaxation time. Gain and refractive index change can be calculated by [22]

$$g(\omega) = \frac{\omega\mu c}{n_b}\mathrm{Im}[\varepsilon_0\chi(\omega)] \qquad (2.56)$$

where μ is the permeability , n_b is the background refractive index, and we also have

$$\Delta n = \frac{1}{2n_b}\mathrm{Re}[\chi(\omega)] \qquad (2.57)$$

Therefore, once suscepbility is calculated, we will obtain the quantum well gain and the associated refractive index change from eqns (2.56) and (2.57).Since the upper and lower valence blocks of Hamiltonian give degenerate states, only the upper Hamiltonian needs to be solved. The final results are multiplied by 2 to account for the degeneracy.

In equation (2.55), the optical polar matrix can be written as

$$\hat{e}\cdot\bar{M}_{mn}^{\sigma\eta}(k_t) = \sum_{u=1,2} < F_m^u \mid \phi_n > < u \mid \hat{e}\cdot\vec{r} \mid S,\eta > \qquad (2.58)$$

where F_m^v and ϕ_n are the envelop function of valence and conduction sub-bands respectively, which we have calculated in the last section. S and u are Bloch period function. After some mathematical calculations we have

for TE mode ($\hat{e} = x$)

$$|\hat{e}\cdot\bar{M}_{mn}^{cm}(k_t)|^2=\frac{1}{4}<S|ex|X>^2(<F_n^1|\phi_m>^2+\frac{1}{3}<F_n^2|\phi_m>^2) \tag{2.59}$$

for TM mode ($\hat{e} = z$)

$$|\hat{e}\cdot\bar{M}_{mn}^{cm}(k_t)|^2=\frac{1}{3}<S|ez|Z>^2(<F_n^2|\phi_m>^2 \tag{2.60}$$

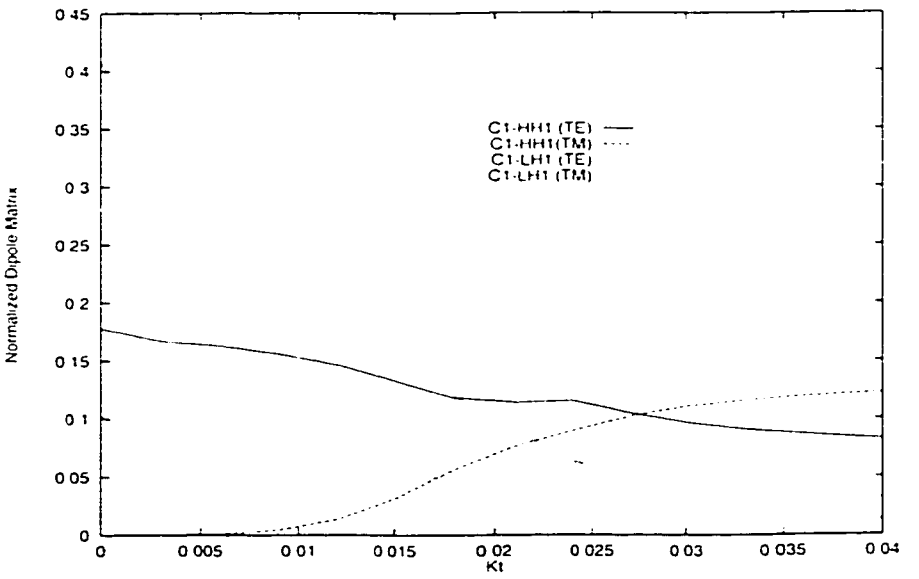

Figure 2. 17 Typical normalized dipole moment of QW material.

From the last section we know that $F_n^{1,2}$ is k_t dependent, so that band-mixing effect will play significant role in the optical dipole matrix. Figure (2.17) shows a typical picture of the optical dipole matrix vs k_t.

We can see that if a parabolic model is used, optical dipole matrix will be constant. The band mixing effect will be neglected.

In our calculation we have used the relation of bulk material [21]

$$< S \mid z \mid Z >=< S \mid x \mid X >= -\frac{\hbar}{\sqrt{2}}[\frac{E_g + \Delta}{E_g(E_g + 2\Delta/3)m_e}]^{\frac{1}{2}} \qquad (2.61)$$

To show the application of this model, in Figure (2.18), the quantum well band structure of $Ga_xIn_{1-x}As_yP_{1-y}$ material is shown. The well width is 60 A. All the other parameters used for the calculation are listed in Table (2.3).

In this case, the strain is tensile. The material gain is calculated for TE and TM modes respectively. Figure (2.19) shows the TE modes for two different electron densities. As the density gets higher, the first light hole band will be filled. When $N = 5\times10^{18} cm^{-3}$, we can see double peaks of the gain spectrum. Figure (2.20) shows both TE and TM modes for $N = 5\times10^{18} cm^{-3}$. From eqn (2.60), we can see that the main contribution to TM mode comes from light hole, thus there is only one peak for TM mode. It is shown that the gain profile bandwidth for QW material is much wider than the bulk material. In fact, the gain profile band-width of QW material could be as large as 100-200 nm.

To describe the refractive index change in the quantum well, we use the line-width enhancement factor

$$\alpha = -\frac{4\pi}{\lambda}\frac{dn/dN}{dg/dN} \qquad (2.62)$$

where n is refractive index, N is carrier density. The α factor of the QW material is much smaller than that of bulk material [21].

Table 2. 3 Material parameters for $In_{1-x}Ga_xAs_yP_{1-y}$ quantum-well calculation

Parameters	InP	GaP	GaAs	InAs	$In_{1-x}Ga_xAs_yP_{1-y}$
A (A)					5.8688-0.4176x+0.1896y+0.0125xy
E_g (eV)					$1.35+0.668x+1.068y+0.758x^2+0.078y^2-0.069xy-0.322x^2y+0.03xy^2$
γ_1	4.95	4.05	6.85	20.4	Vegard's law
γ_2	1.65	0.49	2.1	8.3	Vegard's law
Γ_3	2.35	1.25	2.73	9.1	Vegard's law
C_{11}	10.11	14.05	11.879	8.329	Vegard's law
C_{12}	5.61	6.203	5.376	4.526	Vegard's law
A (eV)	-6.31	-8.83	-8.33	-6.08	Vegard's law
B (eV)	-1.7	-1.8	-1.7	-1.8	Vegard's law
Δ (eV)	0.11	0.08	0.34	0.38	Vegard's law
m_e (m_0)					$0.08-0.116x+0.026y-0.059xy-(0.064-0.02x)y^2+(0.06+0.032y)x^2$

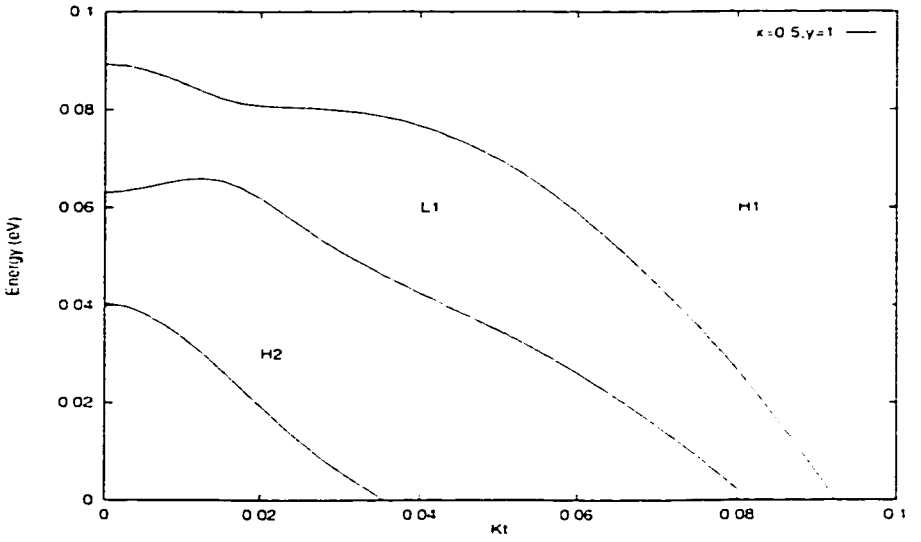

Figure 2. 18 Band structure of InGaAsP QW material. The well width is 60A. For barrier arrier y=0.57

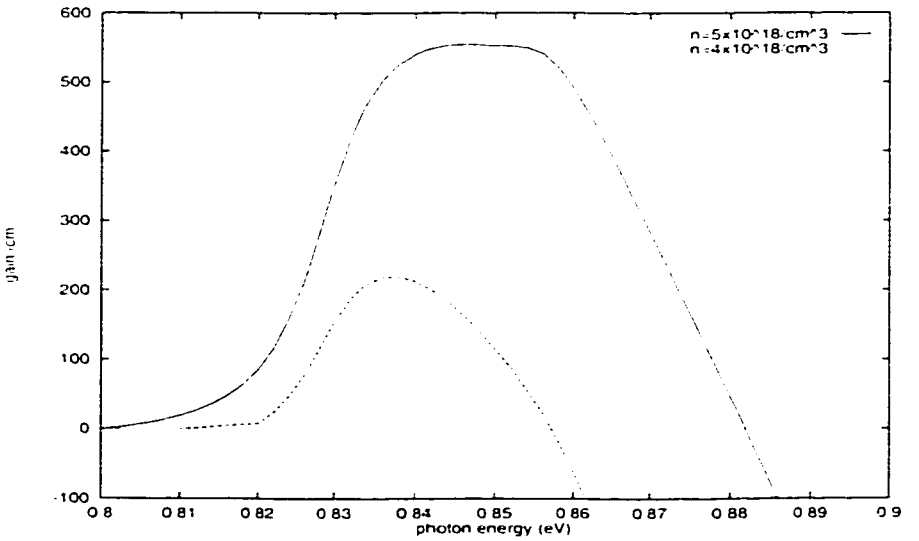

Figure 2. 19 Optical gain for the TE mode with different carrier density.

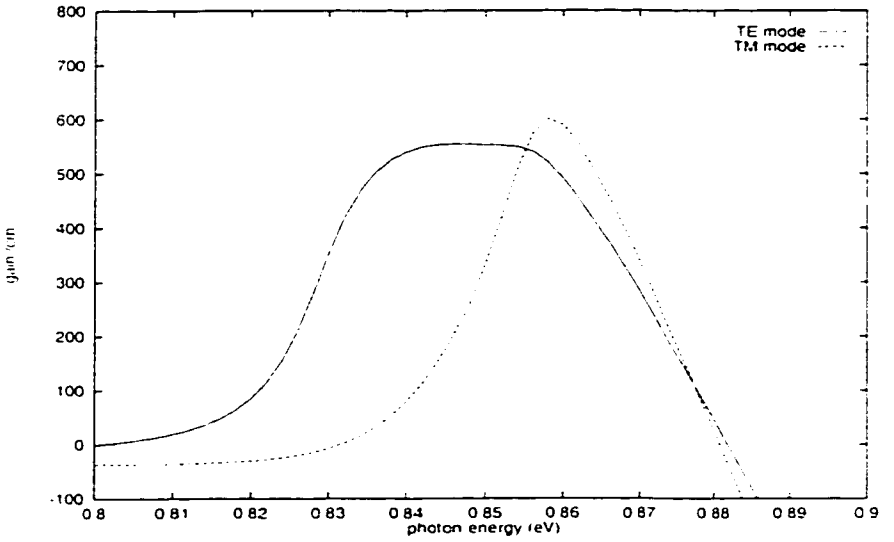

Figure 2. 20 Optical Gain for TE and TM modes with the same carrier density.

Comparisons with the Experiments

In this part, we compare the optical gain profiles calculated by our theoretical model with those obtained from experimental measurements. There are seven quantum wells in the active region with the well thickness equal to 105 A [28]. The QW is fabricated

by InGaAsP material system. The measured optical gain profiles are recorded while injected current changed from 6mA to10mA. Our comparisons are shown in Figure 2.21 and the simulation parameters are listed in Table 2.4. We conclude that the simulation results are reasonably good.

It should be noted that, there is no carrier transport equation in our model and the theoretical simulation is based on the carrier density. Therefore a self-consistent comparison will depend on the development of a more comprehensive model, which should include both carrier transport and optical mode solvers. In fact, along this end, using our QW material models and ALDS laser simulator [24], we have compared the optical gain simulation results indirectly with the measured data such as threshold currents, external efficiencies and oscillation frequencies of laser diodes with QW structures.

Table 2.4 Parameters used in the simulation ($In_{1-x}Ga_xAs_yP_{1-y}$ /InP)

	I=6mA	I=10mA
Carrier density (10^{3}/cm)	2.5	2.8
Temperature (K)	300	300
Effective length (μm)	200	200
Well Ga, As composition (x, y)	(0.504,0.993)	(0.504,0.993)
As composition in the barrier (y)	0.469	0.469

In the simulation, we have chosen the optical confinement factor around 0.1.

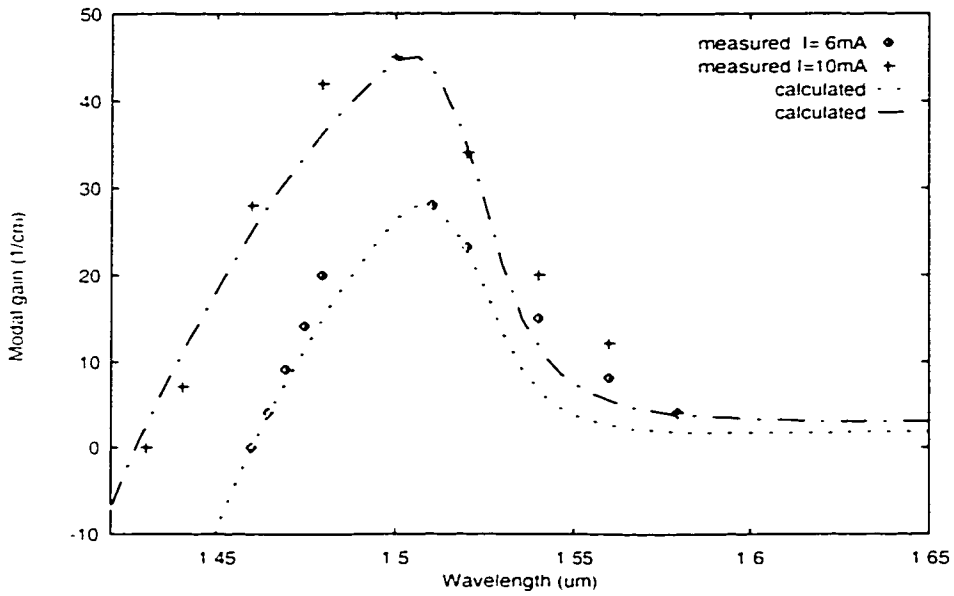

Figure 2.21 Comparisons of the optical gain profiles at room temperature.

2.5 Summary

In this chapter, we have shown the modeling and simulation of semiconductor materials. Both passive and active optical properties, such as refractive index, index change due to carrier injection, thermal or electric field effects, and optical gain are discussed. The simulation results are consistent with the known experimental measured data, or at least show the same trend qualitatively. We have left some fitting parameters in each model. It is believed that with some fitting procedures, the model can provide accurate simulation results as required. The accuracy gap between the

experimental measurement and theoretical model needs a series works in co-operation with the industry experimentalists. With the completed set of measured data, our model can be calibrated, and some new procedures, such as numerical fitting (genetic algorithm), neural networks, will be implemented to the whole simulation package with the material models in this chapter as prototype functions. Along this direction, our QW optical gain model has been used in NORTEL as a design tool and received very good feedback. It is hoped that this co-operation will be continued, and our material simulation package could be calibrated and finally completed. The models will be on one hand be used in the laser design and simulation, and on the other hand be used in any optical device design as a separate simulation tool. In the following chapters, we will refer to this chapter constantly.

Chapter 3

Traveling Wave Model of Semiconductor Laser Diode

3.1 Introduction

Laser diodes are among key components in a wide range of applications such as telecommunications, optical storage, and image recording. Laser diodes with complex longitudinal structures such as the distributed feedback (DFB) and the distributed Bragg reflector (DBR) lasers are particularly attractive due to their superior spectral characteristics such as narrow spectral width, low chirp and/or wavelength tunability. In the modeling and simulation of such laser diodes, there have been two different formalisms, namely, the standing-wave approach [2,4,18,19] and the traveling-wave approach [1,2,7,20]. The standing-wave approach is based on the assumption that the temporal and the spatial dependence of field distributions of the cavity modes are separable. As such, the dynamics is considered in the modal amplitudes. Consequently, the standing-wave approach is valid only when the photon lifetime is much shorter than the characteristic time of the laser dynamics. The traveling-wave

model, on the other hand, makes no assumptions about the cavity modes. Rather, it solves the time-dependent coupled-wave equations for the forward the backward traveling waves directly and therefore is valid even the laser cavity has relatively small Q-factor and/or the characteristic time of the laser dynamics is very short. Another advantage of the traveling-wave model is that it can be readily applied to laser diodes operated with multiple cavity modes, for which the standing-wave model may have difficulty in finding the complex roots corresponding to each mode.

In this chapter, firstly, from wave equation, we will derive an effective one-dimensional field equation for laser diode. Then the difference between the standing wave model and the traveling wave model will be identified based on the same 1-D optical field equation. The limitations of the two approaches will be clarified. Secondly, the traveling wave model will be implemented in details. Especially, the thermal effect is incorporated into the model for the first time. Finally, we will do some comparisons and show some simulation results.

3.2 Effective 1D Field Rate Equation

From appendix, the effective 1D field equation within the laser cavity is written as [4]

$$\frac{\partial^2}{\partial z^2}\Psi(z,t)+k_0^2\left[n_{eff}^2-j\frac{\bar{n}}{k_0}a_L+\frac{\bar{n}}{k_0}\Gamma(j+a_m)g\right]\Psi(z,t) - 2j\frac{k_0^2\overline{nn_e}}{\omega}\frac{\partial}{\partial t}\Psi(z,t)=-\mu_0\omega^2 f_S(z,t) \tag{3.1}$$

where $\Psi(z,t)$ is the longitudinal enveloped electrical field, k_0 is the wave vector in the vacuum at reference frequency ω. α_L and g are optical modal loss and gain respectively. α_m is the line-width enhancement factor and Γ is the optical confinement

factor. n_{eff}, $\bar{n}$, and n_g are effective refractive index, transverse average refractive index and group index respectively which are defined in appendix. f_s is the spontaneous noise source.

From this effective 1D field equation, there are two different approaches, which lead to the standing wave model and the traveling wave model.

3.2.1 Standing Wave Approach

If we assume that the temporal and the spatial dependence of field distributions within the cavity is separable, *i.e.*, the longitudinal enveloped electrical field can be expressed as

$$\Psi(z,t) = \Phi(z)A(t) \tag{3.2}$$

and Φ(z) is the eigen-wave function of the longitudinal mode with complex eigenvalue ξ satisfying the equation,

$$\frac{\partial^2}{\partial z^2}\Phi(z) + k_0^2\left[n_{eff}^2 - j\frac{\bar{n}}{k_0}a_t + \frac{\bar{n}}{k_0}\Gamma(j+a_m)g\right]\Phi(z) = k_0^2\xi\Phi(z) \tag{3.3}$$

By substituting eqn (3.3) into (3.2), we obtain

$$k_0^2\xi A(t) - j\frac{2k_0^2\overline{nn_g}}{\omega}\frac{\partial A(t)}{\partial t} = F_S \tag{3.4}$$

Here we have used the longitudinal field normalization $\int_0^L \Phi^*\Phi dz = 1$, and F_S is the spontaneous noise term transformed from f_S, which will be discussed in detail latter.

Eqns (3.3) and (3.4) are the rate equations of electrical field for standing wave model of laser diodes. In the case DFB lasers, if grating period is Λ, we have

$$\begin{aligned} n_{eff}^{2} &= \overline{n_{eff}^{2}} + \delta n_{eff}^{2} \\ \delta n_{eff}^{2} &= \sum_{l} \Delta \varepsilon_{l} \exp[-jl(2\pi / \Lambda)z] \end{aligned} \tag{3.5}$$

and $\Phi(z)$ can be expressed as

$$\Phi(z) = F(z)\exp(-j\frac{\pi}{\Lambda}z) + R(z)\exp(j\frac{\pi}{\Lambda}z) \tag{3.6}$$

By substituting eqns. (3.5) and (3.6) into eqn. (3.3), and considering only the first order grating, we obtain the coupled mode equations for the forward and reverse enveloped field F and R

$$\begin{aligned} \frac{dF}{dz} &= \{[\Gamma g - a_{L} - k_{0}\,\mathrm{Im}(\xi)]/2 - j\delta\}F + j\kappa R \\ \frac{dR}{dz} &= -\{[\Gamma g - a_{L} - k_{0}\,\mathrm{Im}(\xi)]/2 - j\delta\}R - j\kappa^{*}F \end{aligned} \tag{3.7}$$

where δ is the detuning factor defined by

$$\delta = k_{0}n_{eff} - \frac{\pi}{\Lambda} - \frac{k_{0}^{2}\Lambda}{2\pi}\mathrm{Re}(\xi) \tag{3.8}$$

and coupling coefficient κ in eqn (3.7) is defined by

$$\kappa = \frac{k_0}{2 n_{eff}} \Delta \varepsilon_1 \tag{3.9}$$

To derive eqns (3.7) and (3.8), we have assumed that $n_{eff} = \bar{n}$.

Eqn (3.4) can be transformed into the photon number and lasering phase equation by defining

$$A(t) = \sqrt{S(t)} \exp(j\theta(t)) \tag{3.10}$$

where S is the total photon number within the laser cavity and θ is the photon phase. Substituting eqn. (3.10) into eqn. (3.4), we obtain

$$\begin{aligned} \frac{dS}{dt} &= \frac{\omega}{nn_g} \mathrm{Im}(\xi) S(t) + R_{sp} \\ \frac{d\theta}{dt} &= \frac{\omega}{2nn_g} \mathrm{Re}(\xi) \end{aligned} \tag{3.11}$$

where R_{sp} is the ensemble average spontaneous emission rate term, which is expressed as

$$R_{sp}(t) = K n_{sp} v_g \int_0^L \Gamma g(z,t) dz \tag{3.12}$$

In eqn (3.12), K is Petermann factor, and n_{sp} is inverse spontaneous emission coefficient.

Eqns (3.7) and (3.11) constitute the governing equations to describe the photon dynamics within the laser cavity. Eqn (3.7) represents the longitudinal field profile

$\Phi(z)$ and the complex eigenvalue ξ. The eigenvalue ξ is an important parameter introduced by the standing wave approach whose imaginary part describes the net gain and real part describes the phase shift. Eqn (3.11) represents the dynamics of photon number and lasering frequency shift related to the reference frequency.

By separating the spatial and temporal variables, the standing wave model transforms the partial differential equation (3.1) into a series of differential equations (3.7) and (3.11). Therefore, in the simulation, the spatial discretized step is unrelated to the temporal step, which will be explained in detail in the following sections. This assumption makes it very efficient compared with the traveling wave approach. The other advantage is that since the field profile can be solved in the frequency domain, it is easy to implement the frequency dependent optical gain and refractive index dispersion effects. However, this model assumes that the standing wave pattern is created instantaneously. Therefore, it is impossible to describe some phenomena such as mode beating or mode locking. This model also presents great numerical calculation challenge in searching the standing wave modes for complicated multi-section laser simulation. Finally it is difficult to extend the model to some devices such as optical amplifier which does not support standing wave modes at all.

3.2.2 Traveling Wave Approach

Different from the standing wave approach, the traveling wave model solves the partial deferential equation (3.1) directly. For the case DFB lasers in the previous section, we can express the field profile $\Psi(z,t)$ as

$$\Psi(z,t) = F(z,t)\exp(-j\frac{\pi}{\Lambda}z) + R(z,t)\exp(j\frac{\pi}{\Lambda}z) \qquad (3.13)$$

where $F(z,t)$ and $R(z,t)$ are the enveloped time dependent forward and backward traveling wave functions, respectively. Substituting eqns (3.13) and (3.5) into eqn. (3.1), as in previous section, we neglect the second order derivative of F and R with respective to z. Finally we obtain

$$\begin{aligned} \frac{1}{v_g}\frac{\partial F}{\partial t}+\frac{\partial F}{\partial z} &= \{(\Gamma g - a_L)/2 - j\delta\}F + j\kappa R + s_F \\ \frac{1}{v_g}\frac{\partial R}{\partial t}-\frac{\partial R}{\partial z} &= \{(\Gamma g - a_L)/2 - j\delta\}R + j\kappa^* F + s_R \end{aligned} \qquad (3.14)$$

where v_g is the group velocity, Γ is the optical confinement factor, g is the optical gain, a_L is the optical loss, and δ is the detuning factor, respectively. The coupling coefficients due to the index/gain/loss gratings are κ_F and κ_R, which may be complex. s_F and s_R are the spontaneous emission sources for forward and reverse directions which will be discussed latter.

In the traveling wave model, we do not use the concept of standing wave mode. Instead, the partial deferential equation of the electrical field is solved directly. The field function includes both magnitude and phase information of the photons. The lasing frequency is determined by the Fourier transform of the output field from the laser facets and local photon density is proportional to the normalized power $|F|^2+|R|^2$. We will explore the traveling wave model in the next section extensively.

3.3 1D Traveling Wave Model

The traveling-wave model has been well developed with consideration for important effects in laser diode operation such as the variations of the average photon and carrier distributions along the laser cavity, the optical gain saturation, the random noise and

so on, with the exception for the thermal effect. In practice, however, the temperature distribution along the laser cavity and the thermal dynamics are important for the design and applications of the laser diodes. It is therefore necessary to incorporate the static and dynamic thermal effects in a self-consistent manner into the comprehensive traveling wave simulator. In this section, we will explore the model extensively. Firstly, based on the last section, we re-formulate all the governing equations of the traveling wave model, especially, the thermal effects are incorporated into the model for the first time. Secondly, we demonstrate the details of the numerical implementation of the traveling wave approach. Thirdly we will do a brief investigation on the series ohm resistance effects on the laser diode operation.

3.3.1 Theoretical Formulations

As we derived in the previous section, the governing equations for the envelopes *F(z,t)* and *R(z,t)* of the forward and backward traveling optical fields are eqn (3.14)
For the sake of simplicity, we may assume that the noise terms are approximated by a complex Gaussian noise with zero mean and satisfying the following correlation relation

$$\begin{aligned} \left\langle s_{F,R}(z,t)s_{F,R}^{*}(z',t')\right\rangle &= \beta K\left(BN^{2}/L\right)r_{sp}\,\delta(z-z')\delta(t-t') \\ \left\langle s_{F,R}(z,t)s_{F,R}^{*}(z,t)\right\rangle &= 0 \end{aligned} \qquad (3.15)$$

where L is laser cavity length, β is the spontaneous coupling factor and K is the Petermann coefficient. N=N(z,t) is the average carrier density in the active region along the laser cavity and is described by the carrier rate equation as

$$\frac{d}{dt}N(z,t)=\frac{I(z,t)}{eV}-\frac{1}{\tau}N(z,t)-BN^2(z,t)-CN^3(z,t)-2gv_gP(z,t) \qquad (3.16)$$

where I(z,t) is the injected current in the active region, V is the active region volume of the laser diode. The constant e is the free electron charge. The parameter τ stands for the electron lifetime and B and C are bimolecular and Auger recombination coefficients, respectively. P(z,t) is the photon density, which is related to the magnitude of the traveling wave amplitudes as

$$P(z,t)=|F(z,t)|^2+|R(z,t)|^2 \qquad (3.17)$$

The optical gain is modeled by the equation

$$g=\frac{g_N\exp[-(T-T_r)/T_g]\{N-N_T\exp[(T-T_r)/T_n]\}}{2(1+\varepsilon P)} \qquad (3.18)$$

where T=T(z,t) is the average temperature in the active region, T_r is a reference temperature and T_g, T_n are the thermal characteristic temperatures for the differential gain and transparent carrier density, respectively. g_N is the differential gain and N_T the transparent carrier density, both of which are taken at the reference temperature T_r. ε is the gain compression factor. Note that in this model, the differential gain and the transparent carrier density are both temperature dependent as evident in eqn.(3.18).The effective refractive index can be expressed as

$$n_{eff}=n_{eff}^0-\Gamma a_m g\frac{\lambda_0}{4\pi}+\alpha(T-T_r) \qquad (3.19)$$

where n_{eff}^{0} is the refractive index at the reference temperature T_r, a_m is the line-width enhancement factor, and λ_0 is the reference wavelength, respectively. The parameter α is the temperature coefficient for the effective index change due to the thermal effect. The detuning factor in eqn. (1a) and (1b) is defined as

$$\delta = \frac{2\pi}{\lambda_0} n_{eff} - \frac{\pi}{\Lambda} \tag{3.20}$$

where Λ is the grating period of the DFB laser. Note that, due to the temperature dependence of the effective index, the detuning factor is also a function of temperature.

All the material parameters can be obtained by fitting the empirical equation to the experimental/simulation data presented in the previous chapters

Temperature in the laser cavity is governed by the heat transfer equation [10,12].

$$\frac{\partial}{\partial t} T(x,y,z,t) = D\nabla^2 T(x,y,z,t) + R_t\left(\frac{E_g}{e} I - P_{out}\right) + R_t R_s I^2 \tag{3.21}$$

where T(x,y,z,t) is the temperature, which is a function of time and position. D is the thermal diffusion coefficient and $R_{s,t}$ are the material series resistance and reciprocal of thermal capacity, respectively. E_g is the band gap energy in the active region. P_{out} is the total output power from the laser. It is noted that the injected current works as the heat source, whereas the optical output power as the heat drain. In the thermal simulation, instead of solving eqn. (3.21) numerically as done in [15], we assume that the thermal diffusion goes only downward to the heat sink, which is located at a distance h from the active region. Further, we assume that the distance h between active region and heat sink is much less than the other dimensions [4]. Under this

circumstance; therefore, the temperature distribution is uniform in the lateral direction denoted as y (parallel to the expitaxial surface) and temperature difference is caused only by non-uniform injected current in the longitudinal direction denoted as z . With this assumption, we can solve an effective 1-D thermal equation in the downward direction denoted as x. At the bottom (i.e., the heat sink), the boundary condition is constant $T=T_c$, where T_c is heat sink temperature and on the top, adiabatic boundary condition is used. It is readily shown that the resultant 1-D diffusion equation has an analytic solution. The active region (with thickness equal to d << h) temperature can be expressed as [4]

$$T(z,t) = T_c + \sum_{n=0}^{\infty} t_n^1 \exp(-D_n t)\left[\frac{I_{s0}^2}{D_n} + \int_0^t \exp(D_n)I^2(z,\tau)d\tau\right] + \sum_{n=0}^{\infty} t_n^2 \exp(-D_n t)\left(\frac{I_{s0}-X_{s0}}{D_n} + \int_0^t \exp(D_n\tau)[I(z,\tau)-X(\tau)]d\tau\right) \tag{3.22}$$

where I_{s0} is the static injected current at the initial time. The parameter X_{s0}, which will be defined below, is a constant related to the initial static output power. The other parameters are defined as follows

$$D_n = \left[\frac{(n+1/2)\pi}{h}\right]^2 D \tag{3.23}$$

$$t_n^1 = (-1)^n \frac{2}{h}\int_0^h R_t(x)R_s(x)\sin\left[\frac{(n+1/2)\pi x}{h}\right]dx \tag{3.24}$$

$$t_n^2 = \frac{2E_g d}{eh}R_t(h) \tag{3.25}$$

$$X(t) = \frac{e}{E_g} P_{out}(t) \tag{3.26}$$

Eqns. (3.14), (3.16) and (3.22) provide a self-consistent formulation for the traveling-wave model of DFB laser diodes with consideration of the static and dynamic optical, carrier and thermal effects.

3.3.2 Numerical Implementation

To solve the governing equations for the self-consistent simulation of the static and dynamic characteristics of a DFB laser, we first discretize the traveling wave equations for the optical field envelope. There are two commonly used approaches in the discretization. One is the finite difference method (FDM); the other is transfer matrix method (TMM). We will introduce both methods in this section.

Finite Difference Method (FDM)

Using the explicit finite difference approach, enveloped optical field can be written as

$$\begin{aligned} F_{m+1}^{n+1} &= \exp[(\Gamma g - a_s - j\delta)\Delta z] F_m^n + j\kappa_F \Delta z R_{m+1}^n + s_{F\,m}^{\,n} \Delta z \\ R_m^{n+1} &= \exp[(\Gamma g - a_s - i\delta)\Delta z] R_{m+1}^n + i\kappa_R \Delta z F_{m+1}^n + s_{R\,m}^{\,n} \Delta z \end{aligned} \tag{3.27}$$

where we denote the time step in superscript (n or n+1) and space step in subscript (m or m+1). In derivation of eqn. (3.27), we have used the relation $\Delta z = v_g \Delta t$ which is the upper limit of the convergence condition. Therefore, unlike the standing wave approach, the spatial and temporal discretization is related by the group velocity in the

traveling wave model. It is noted that our discretization for the traveling-wave equations is different from that given in [1] in the following sense: We use an exponential term to express the incremental change of the field amplitude due to amplification and phase shift. In the absence of gratings, it is readily shown that the formulation reduces to the exact solution for the FP lasers. As the discretization in [1] corresponds to the first-order approximation of the exponential in eqn. (3.27), our formulation is expected to be more accurate.

Transfer Matrix Method (TMM)

In TMM approach, we assume that

$$\begin{aligned} \frac{\partial F}{\partial t} &= j\mu F \\ \frac{\partial R}{\partial t} &= j\mu R \end{aligned} \tag{3.28}$$

μ can be interpreted as frequency chirp and magnitude change of the local field. With this assumption, enveloped optical field equation can be solved analytically and expressed in the form a transfer matrix / scattering matrix

$$\begin{bmatrix} F_{m+1} \\ R_n \end{bmatrix}^{n+1} = C \begin{bmatrix} \gamma & -jk_t \sinh(\gamma \Delta z) \\ -jk_R \sinh(\gamma \Delta z) & \gamma \end{bmatrix} \begin{bmatrix} F_m \\ R_{m+1} \end{bmatrix}^n \tag{3.29}$$

where

$$\gamma = (g - a_v + j\mu - j\delta)^2 + k_F k_R$$
$$C = \frac{\exp(j\mu\Delta z)}{[\gamma \cosh(\gamma\Delta z) + (g - a_v + j\mu - j\delta)\sinh(\gamma\Delta z)]} \tag{3.30}$$

In this approach, μ is a local time dependent variable, which should be updated in every time step.

Both FDM and TMM approaches are described in Figure (3.1). The total laser cavity is discretized into M elements or cells with M+1 nodes. The optical field F in node m+1 at time n+1 will be determined by the field in node m and R in node m+1 at time n. For optical field R, similar approach is applied as shown in Figure (3.1). During the simulation, all other physical variables in eqns (3.27) and (3.29) are the values in cell m and should be updated in every time step. Therefore the photon density in cell m can be expressed as

$$P_m = \frac{(|F_{m-1}|^2 + |R_{m-1}|^2) + (|F_m|^2 + |R_m|^2)}{2} \tag{3.31}$$

The coupling coefficients in eqn(3.27) and (3.29) are related by $k_r = k_R^*$ for index coupling laser and $k_t = -k_R^*$ for the gain coupling.

Finally, the output powers from both facets P_L and P_R are in the form

$$P_L = \hbar\omega P_1 v_g A(1 - |r_L|^2)/\Gamma$$
$$P_R = \hbar\omega P_{M1} v_g A(1 - |r_R|^2)/\Gamma \tag{3.32}$$

where A is the effective active region area of the facets. $P_{1,M}$ is the photon density in the first and the M-th cell respectively.

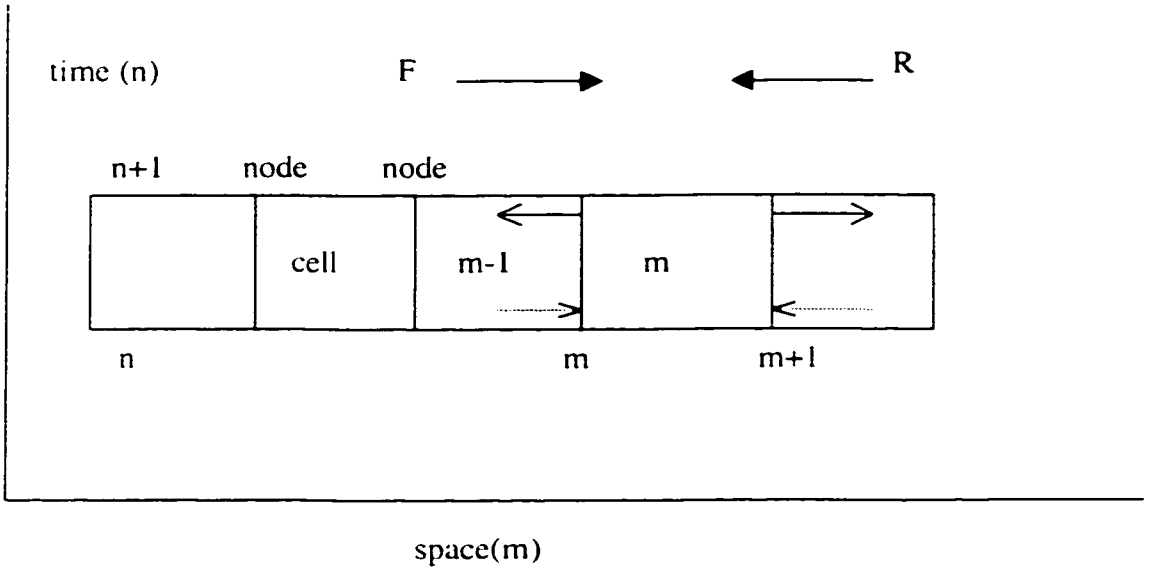

Figure 3. 1 Discretization scheme for the traveling wave model.

The boundary condition is determined by

$$\begin{aligned} F_1^{n+1} &= r_L R_1^{n+1} \\ R_{M+1}^{n+1} &= r_R F_{M+1}^{n+1} \end{aligned} \tag{3.33}$$

where $r_{L,R}$ is the field reflectivity at left and right facets respectively.

Frequency Dependent Gain Profile

As we show in the previous sections, the traveling wave model solves the optical field equation directly in time domain. Therefore, the frequency dependent gain profile can not be implemented so easily as in the standing wave approach. In this section, we introduce a simple time domain digital filter to simulate the parabolic shaped gain

profile. More advanced approach and detail theoretical explanation will be left to the next chapter.

We introduce a linear recursive digital filter with two characteristic parameters α and ϕ in every discretization cell. These two parameters are determined by the gain profile in frequency domain. If we denote the coarse field before passing the gain profile filter by X and Y for forward the reverse traveling wave respectively, then

$$\begin{aligned} F_m^{n+1} &= (1-\alpha)X_m^{n+1} + \alpha\exp(j\phi)F_m^n \\ R_m^{n+1} &= (1-\alpha)Y_m^{n+1} + \alpha\exp(j\phi)R_m^n \end{aligned} \tag{3.34}$$

This digital filter is corresponding to a frequency dependent gain profile with response function $H(f)$ in the form [11]

$$|H(\Delta f)|^2 = \frac{(1-\alpha)^2}{1+\alpha^2-2\alpha\cos(2\pi\Delta f\Delta t-\phi)} \tag{3.35}$$

where Δt is the time step set for the simulation and Δf is frequency difference with respect to the reference frequency. Therefore, α and ϕ in equation (3.35) could be obtained by fitting the response function to the gain profile. It should be noted that this simple approach is only valid for parabolic-shaped gain profile. More complicated response function will be introduced in the next section.

Carrier Rate Equation

The carrier equation (3.16) is discretized by the Euler method as

$$N_m^{n+1} = N_m^n + \Delta t\left(\frac{I_m^n}{eV} - \frac{N_m^n}{\tau} - B(N_m^n)^2 - C(N_m^n)^3 - 2gV_g P_m^n \right) \qquad (3.36)$$

In this implementation, we have assumed that the injected current is distributed uniformly. In fact, in reality we only know the voltage applied on the diode. Because of the longitudinal hole burning effect, the carrier distribution will result in non-uniform current distribution. However, this effect is not obvious experimentally. We will give a brief theoretical discussion on this issue at the end of this chapter.

Thermal Effects

Finally, the integrals in the calculation of the average temperature in the active region are carried out numerically.

For the transient-state simulation, we may solve the coupled equations (eqs. 3.27, 3.36 and 3.22) for the optical, the carrier and the thermal processes in a self-consistent manner by following the flow-chart depicted in Figure 3.2a. First, the initial state optical field, the carrier density, the temperature and other related parameters are set based on the static state simulation which will be discussed in details in the following; as time proceeds, the the optical field will propagate in the cavity as shown in eqn. (3.27), the carrier density will change according to eqn. (3.36) and a new temperature can be calculated by integral equation 3.22. The other parameters will also be updated using eqns. (3.17-3.20).This process will continue until the preset time is reached.

For the static-state simulation, however, the task appears to be more difficult due to the fact that the thermal process is much slower than the optical and the thermal ones. If we follow the same procedure as in the transient-state simulation described above, we will have to solve all the coupled equations as time evolves until the thermal steady state is reached. Such a procedure is extremely time consuming and may even suffer from the accumulation of round-off errors. To overcome this difficulty, we developed

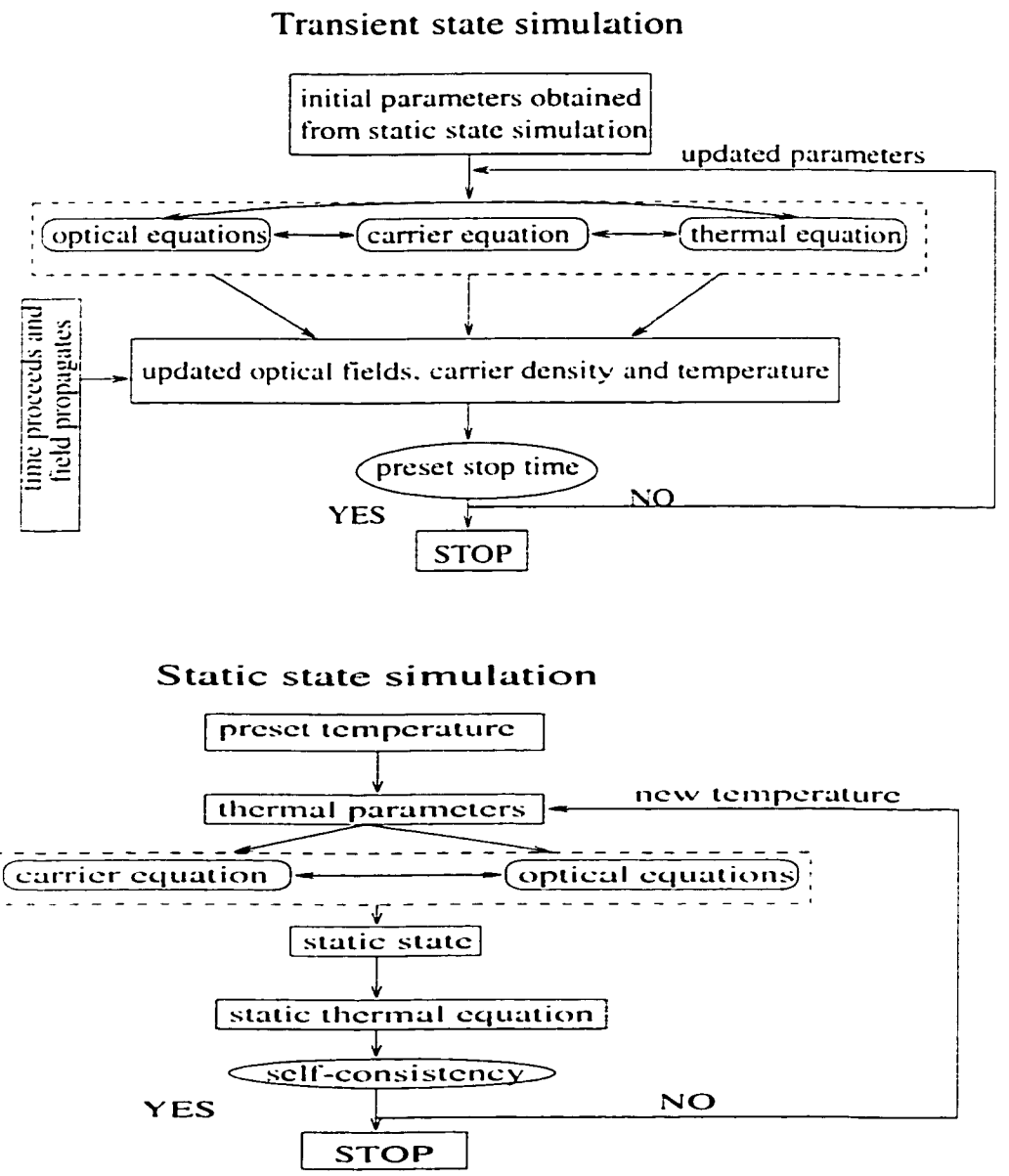

Figure 3. 2 Flow-charts for the static state and transient state simulation of the traveling wave model.

an iterative procedure as described in Figure 3.2b. Since the time constant of optical effect is very small compared with the thermal one, we can fix the active region temperature, for example, as the heat sink temperature first and then do the traveling wave simulation without considering the thermal process until the steady state is reached. The output power and injected current are subsequently substituted into the static thermal equation

$$T(z,t)\Big|_{\text{steady-state}} = T_c + \sum_{n=0}^{\infty} \frac{t_n^1}{D_n} I^2 + \sum_{n=0}^{\infty} \frac{t_n^2}{D_n} \left(I - \frac{e}{E_g} P_{\text{out}} \right) \qquad (3.37)$$

so that the average temperature in the active region is modified using this calculated value and other thermal related parameters are also reset accordingly. This procedure will repeat itself until the output power and the active region temperature converge,i.e., eqn.(3.37) is satisfied automatically.

Noise Term

In this model, we assume that the forward emitted noise source is the same as the reverse one, *i.e.*, $s_F = s_R = s$ This noise source is simulated by a Gaussian distributed random number generator satisfying the correlation relation eqn(3.15).
s is an random complex number expressed as

$$s = x + jy \qquad (3.38)$$

x and y are unrelated Gaussian distributed numbers with average equal to zero. From eqns. (3.15) and (3.38), it can be derived that the standard derivation of x and y should

be $\sqrt{\beta K R_{sp}/2}$, where $R_{sp} = BN^2/L$. It should be noted that in the discretized form, there is a noise term in every cell at any specific time step. All these noise terms are unrelated both in space and time domains.

Output Spectrum

During the simulation, the output field from both facets is memorized as time proceeds. We can choose a typical part from these data from both facets denoted as $F_{1,2,\ldots N}$ and $R_{1,2,\ldots N}$ and perform the Fourier transform to obtain the output spectra. If we open a N sample points window at equal time interval Δt and use fast Fourier transform (FFT) to compute its discrete Fourier transform

$$\begin{aligned} \tilde{F}_k &= \sum_{l=0}^{N-1} F_l w_l \exp(2\pi j l k / N) \\ \tilde{R}_k &= \sum_{l=0}^{N-1} R_l w_l \exp(2\pi j l k / N) \end{aligned} \tag{3.39}$$

then the power spectra at N+1 frequency points are

$$\begin{aligned} P_R(f_k) &= 1/W \mid \tilde{F}_k \mid^2 \\ P_L(f_k) &= 1/W \mid \tilde{R}_k \mid^2 \end{aligned} \tag{3.40}$$

where

$$f_k = k/(N\Delta t), \qquad k = 0, \pm 1, \ldots\ldots, \pm N/2 \tag{3.41}$$

When we perform the FFT of the output field, we have used a *typical* segment of data. It means that we used N sample points to stand for infinite number of field points. It is equivalent to multiply a window function which equals to one at the time segment NΔt and equal to zero at other time. This window function will introduce false information in frequency domain after the FFT transform. Therefore, Parzen window has been applied in the FFT. w_l in eqn. (3.39) and W in eqn.(3.40) contain all the information of Parzen window

$$w_l = 1 - \left| \frac{l - 1/2(N-1)}{1/2(N+1)} \right| \qquad (3.42)$$
$$W = N \sum_{l=0}^{N-1} w_l^2$$

There is a commonly used spectrum calculation algorithm in standing wave model called the transfer matrix method or the Green function method [14]. In that algorithm, when carrier and photon distribution within the cavity is obtained, by calculating the local reflectivity and transmission using the transfer matrix cascade and performing the integration, the output spectrum can be obtained analytically. In the traveling wave model, this algorithm could be used naturally, as the carrier and the photon distributions have been calculated without solving the standing wave equation. We will show later that these two methods in fact produce the same results. Therefore, we will choose one of the methods or use both of them in the simulation depending on the problem to be solved.

3.3.3 Series Ohmic Resistance Effects

In the previous sections, we assume that the injected current is a constant within one section. However, in reality we know instead the voltage applied to the diode. For this reason, we will modify the carrier rate equation (3.16) concerning the series resistance of the laser diode. We change eqn.(3.16) to the form [21]

$$\frac{\mathrm{d}}{\mathrm{dt}}\mathrm{N}(\mathrm{z},\mathrm{t}) = \frac{V_A(t) - V_F(z,t)}{eVR} - \frac{1}{\tau}\mathrm{N}(\mathrm{z},\mathrm{t}) - \mathrm{BN}^2(\mathrm{z},\mathrm{t}) - \mathrm{CN}^3(\mathrm{z},\mathrm{t}) - 2\mathrm{gv}_g\mathrm{P}(\mathrm{z},\mathrm{t}) \quad (3.43)$$

where V_A is the applied voltage on the diode, and V is active region volume. R is the bulk series resistance of the laser diode. V_F is the Fermi voltage, which will lead to the non-uniform injected current distribution. By definition, the Fermi voltage is equal to the semi-Fermi level difference between the electrons and the holes in the semiconductor. Therefore we have

$$V_F = \frac{1}{e}\left[E_g + kTF_c^{-1}(n) + kTF_v^{-1}(p)\right] \quad (3.44)$$

where, E_g is the band gap energy of the semiconductor material in the active region, k is the Boltzmann constant and T is temperature. n and p are electron and hole densities respectively. F^{-1} is the reverse Fermi function, which can provide the Fermi energy for a specific carrier density. This function is changed from material to material and can be found in the previous chapters.

3.4 Comparisons and Applications

In this section, we will first compare our simulation results with the well-known COST240 group's calculations for the static state simulation and A. J. Lowery /J. E.

Carroll's calculations for the transient state simulation. Then a few simulation applications will be presented, which includes index and gain coupled DFB laser, $\lambda/4$ phase shift DFB laser and FP laser. The last application is a detail discussion on the thermal effects.

3.4.1 Comparisons

Static State Simulation

COST240 was a project set up to compare the laser simulation results of twelve research groups in 1994, thereby often used as a benchmark for DFB laser models.[17] By our definition, all models in COST240 are in the standing wave approach. Therefore, their results provide the most reliable static state calculation. As we discussed in the previous sections, traveling wave model is a large signal model. If simulation time is long enough until the laser gets its static state, however, we can also use the model to perform static state simulation. In Figure 3.3, using the same simulation parameters, we show the L-I curve comparison of our traveling wave model with the COST240's results. They are in excellent agreement.

In the traveling wave model, it is difficult to define the threshold value. In practice, we simply lower the injected current to locate the minimum current, which can still provide stable output power in the time domain. The threshold current obtained from this method is around 23-24 mA, which agrees with the COST240 result 23.75mA. The lasing frequency is 1.6577μm, which also agrees with COST240's 1.6583μm.

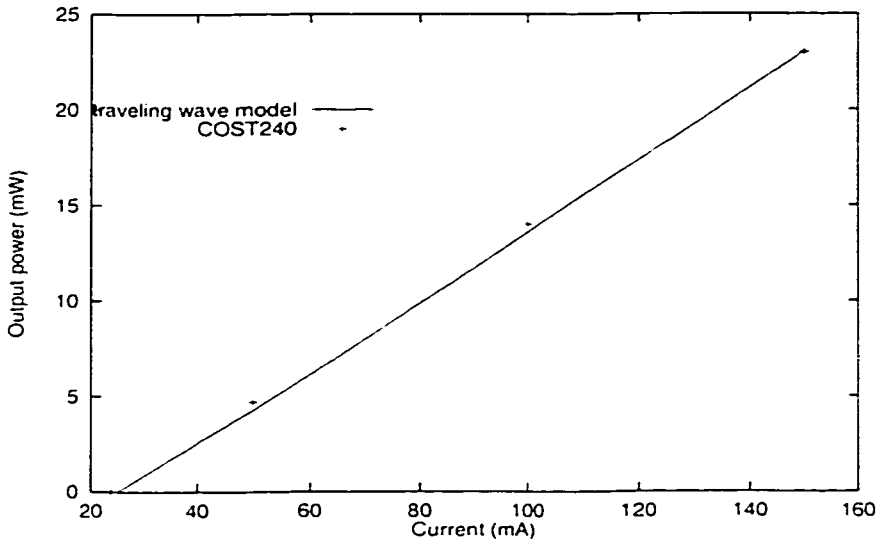

Figure 3. 3 Comparison of the L-I curve of a λ/4 phase-shifted DFB laser between the traveling wave model and COST240.

Transient State Simulation

We will compare our transient state simulation with those calculated by A. J. Lowery and J. E. Carroll's [18,16]. A. J. Lowery's model is called the transmission line model and J.E. Carroll's model is called the power matrix method. By our definition, the first one is a traveling wave approach, and the second one is a standing wave approach. Setting the same simulation parameters as [16,18], we compare our transient state simulation results with those obtained by power matrix method in Figure (3.4) .

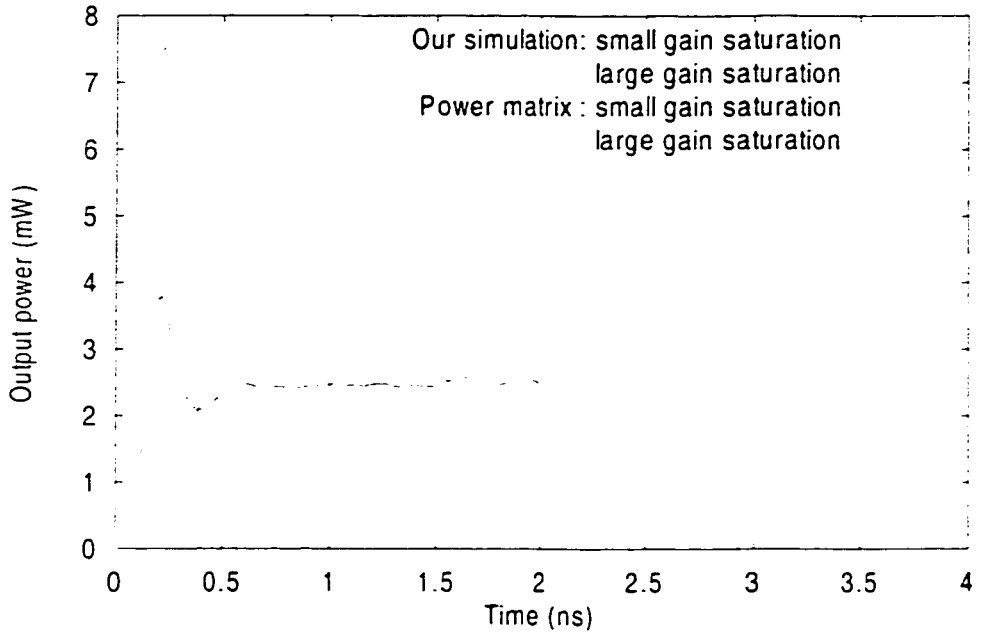

Figure 3. 4 Transient state of a λ/4 phase-shifted laser with different gain saturation coefficients. The parameters are the same as [18]

Our results are in very good agreement with power matrix approach for both gain-saturation cases. As for the transmission line model, the results are also in good agreement with our models, except their results show more noise driven fluctuation.

3.4.2 Fabry-Perot (FP) Laser

For FP lasers, the frequency dependent gain profile is the only wavelength-selecting mechanism; therefore this kind of lasers normally work in multi-mode operation. Using the parameters listed in Table 3.1, we simulate a FP laser with both facets cleaved. During the simulation, we use two different approaches. One is with a uniform gain profile with the active region band gap equal to 0.8 eV (emission wavelength around 1.55μm); the other is a parabolic gain profile with the gain peak at 1.55μm and full width to half maximum value (FWHM) equal to 50nm. With 50mA injected current, we show the output power and output spectra in Figure 3.5-3.7 respectively.

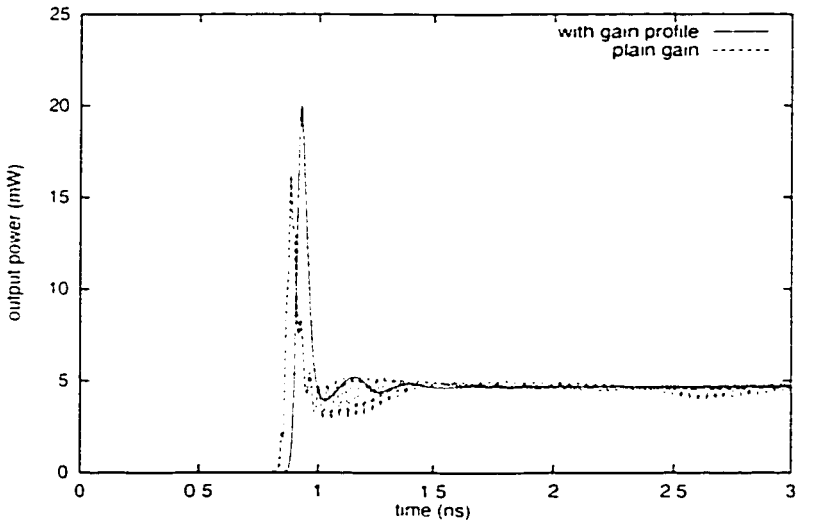

Figure 3. 5 Output power of a FP laser with step injected current equal to 50 mA.

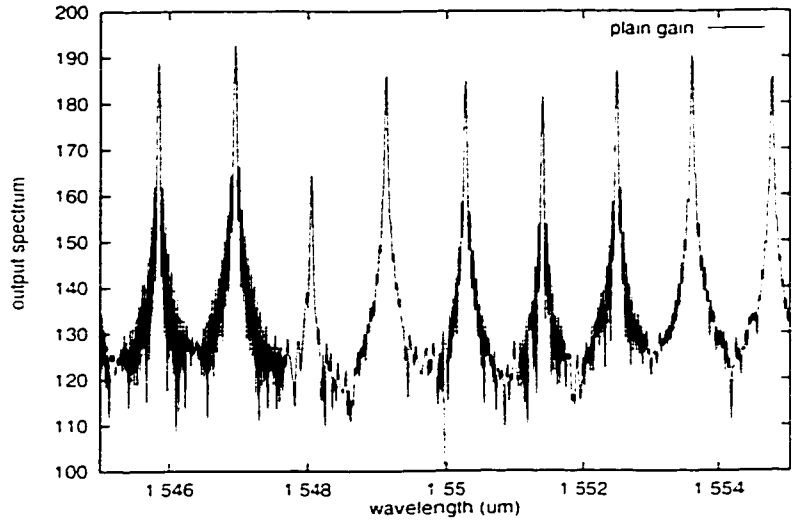

Figure 3. 6 Output spectrum of a FP laser with plain gain profile (normalized scale).

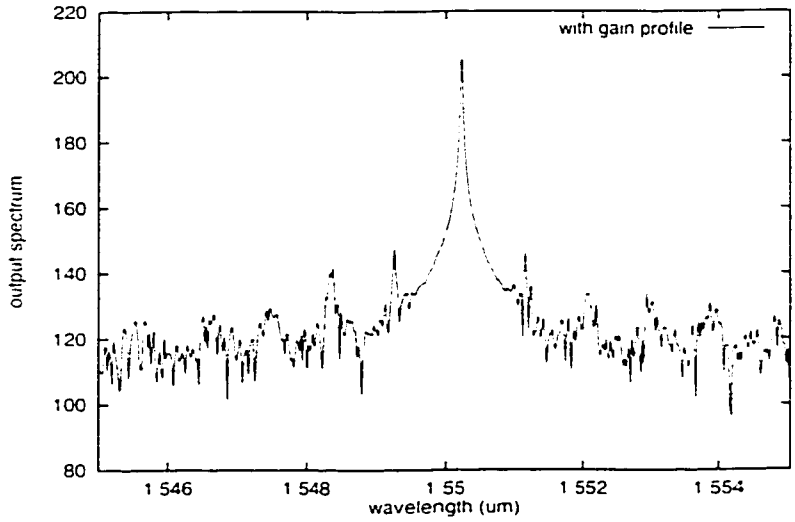

Figure 3. 7 Output spectrum of a FP laser with parabolic gain profile with FWHM equal to 50 nm (normalized scale).

It is shown that in the uniform gain profile case, since there is no mode-selection mechanism, all FP modes are excited around the reference wavelength. Because of multi-mode operation, there is a large energy fluctuation at the static state; in parabolic gain case, the mode near the gain peak is enhanced to be the lasering wavelength, and the other modes far from the gain peak are smeared. Although it still operates in multi-mode operation, the mode suppression ratio (MSR) is quite large.

Table 3. 1 . Laser parameters used for the simulation

Parameters	**values**
Facet reflectivies	0 (DFB)
($r_{L,R}$)	cleaved (FP)
Grating period (ns) Λ	244.5 (DFB only)
KL	1.5 (DFB only)
Strip width (μm) w	1.5
Active layer thickness (μm) d	0.2
Laser length (um) L	300
Confinement factor (Γ)	0.3
Effective index (n_{eff})	3.2
Group index (n_g)	3.6
Internal loss (cm^{-1}) a_v	50
Differential gain (10^{-6} cm^3) g_n	2.5
Transparent carrier density (cm^{-3}) N_0	10^{18}
Non-linear gain saturation coefficient (cm^3) ε	$6.0x10^{-17}$
Line-width-enhancement factor (a_m)	4
Carrier life time (ns) τ	10
Bimolecular radiation coefficient (10^{-10} cm^3 s^{-1}) B	1
Auger coefficient (10^{-29} cm^6 s^{-1}) C	7.5
Spontaneous emission coefficient (β)	$5x10^{-5}$
Petermann factor (K)	1
Gain coupling ration (for gain coupled laser only)	10%

3.4.3 Index and Gain Coupled DFB Lasers

Bragg grating is a widely used technique applied in semiconductor lasers as the lasering wavelength-selection component. However, pure index grating laser normally produces two degenerate lasering wavelengths at the edge of Bragg stop band. Usually, one of the modes will be dominant dependent on the random facet condition. But if an in-phase gain coupling, which means $k=k_R+jk_I$, is introduced, the longer wavelength mode will be enhanced to produce a single mode laser.

In this section, we will first simulate a pure index coupled DFB laser and the carrier/photon distributions at the static state are shown in Figure 3.8 and 3.9, respectively. The laser parameters used are listed in Table 3.1. To control the lasering wavelength deterministically, a 10% gain coupling is introduced and the output spectra of the two cases are compared in Figure 3.10.

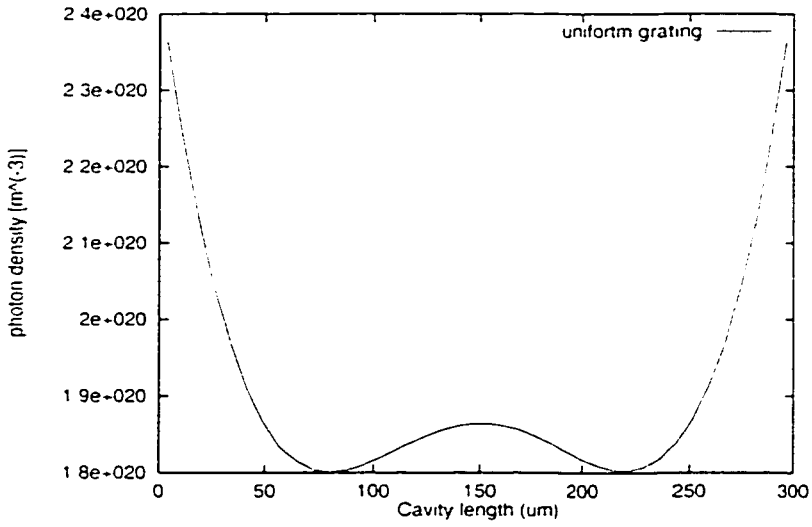

Figure 3. 8 Photon distribution at the static state for a index coupled DFB laser

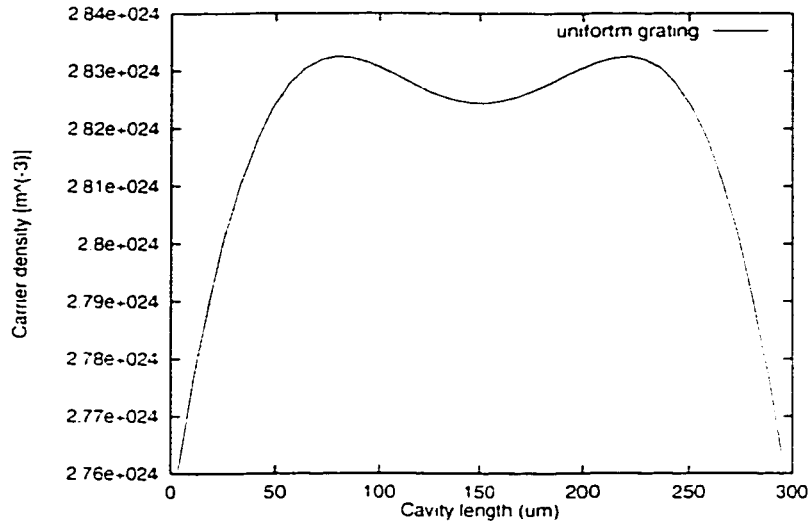

Figure 3. 9 Carrier distribution at the static state of a index coupled DFB laser.

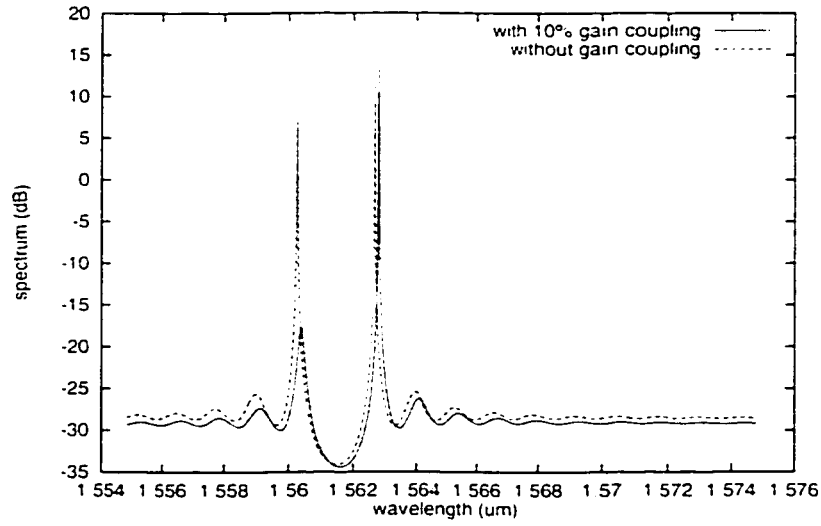

Figure 3. 10 Spectral comparison of index coupled and 10% gain coupled DFB lasers.

3.4.4 Large Signal Modulation of Single Mode Laser

There is another commonly used technique to obtain single mode operation of DFB laser, *i.e.*, a λ/4 phase shift can be applied in the middle of the laser diode. Using the same parameters as in [17], the static state output spectrum of this DFB laser at 50mA bias is shown in Figure 3.11. In the spectrum calculation, we have used both FFT method and the transfer matrix method (TMM). We can see that these two approaches provide similar results. In the FFT method, the reference wavelength in the simulation plays an important role. Therefore, we need multi-runs of the simulator to locate the correct lasering wavelength. From Figure 3.11, we can see that strong noise spectrum even make the stop band invisible. As such, we usually use the two methods in a combinative way.

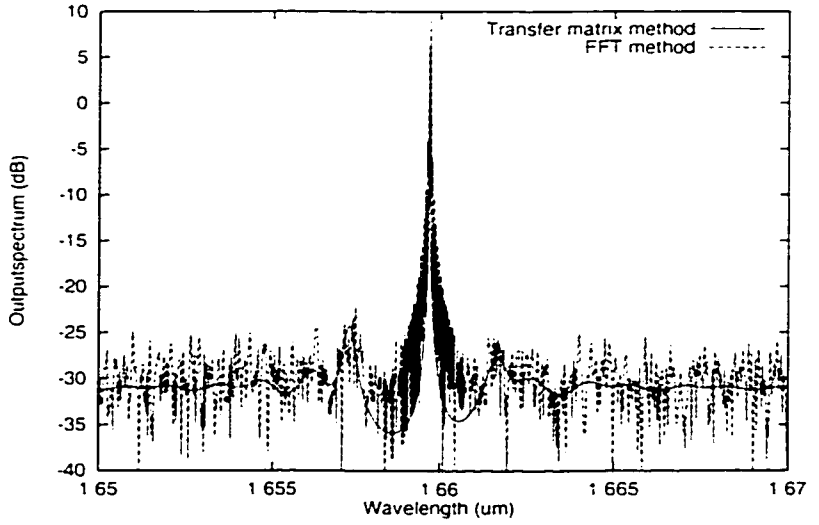

Figure 3. 11 Static state spectrum comparison of a λ/4 phase shifted DFB laser calculated by FFT and TMM methods

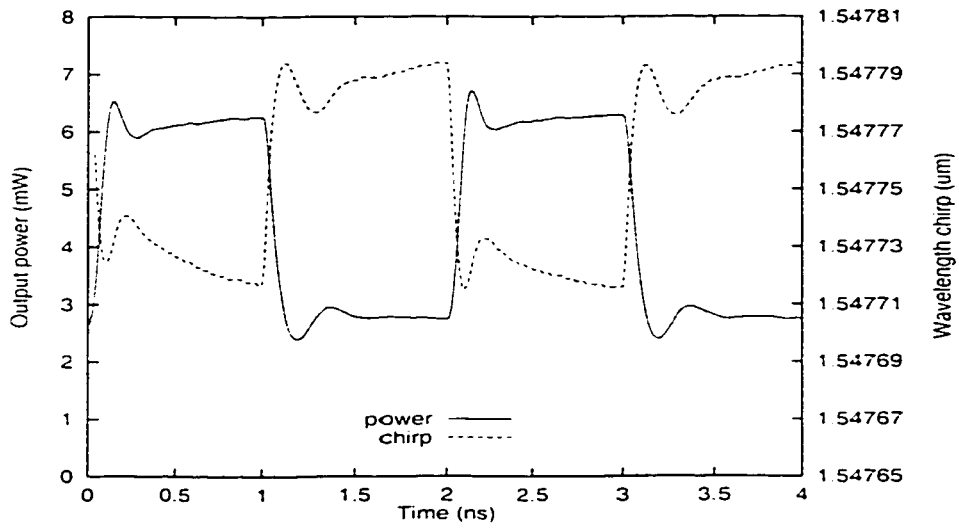

Figure 3. 12 Output power and wavelength chirp of a λ/4 phase-shifted DFB laser during the large signal modulation.

The traveling wave model is large signal model; therefore it is very efficient in the simulation of large signal modulation of laser diodes. Using the λ/4 phase-shifted laser whose parameters are set as in [16], we first let the simulator run 5ns with 50 mA bias injected current to obtain the static state. Then a 500MHz square wave modulation is applied to the laser diode with the modulation magnitude equal to 20mA. Figure 3.12 shows the output power and frequency chirp during the modulation. When the injection current rises, the output power will also increase. However, the wavelength will shift to blue direction due to the larger carrier injection. In the following section, we will also discuss the thermal effects on the wavelength chirp during the large signal modulation.

3.4.5 Thermal Effects of Laser Diode

To demonstrate the traveling wave model with consideration for the thermal effects, we simulated a $\lambda/4$ phase-shifted laser. The parameters used in the simulation are listed in Table 3.2

Table 3. 2 Parameters used for the thermal effect simulations

Parameters	Values
κL	2
Cavity length L (μm)	300
Grating Period Λ (μm)	0.2445
Active layer thickness d (μm)	0.2
Active layer width w (μm)	1.5
Carrier life time τ (ns)	10
Bimolecular coefficient B (10^{-10} cm^3/s)	1
Differential gain g_N (10^{-16} cm^2)	2.5
Absorption and scattering loss a_s (cm^{-1})	50
Effective index n_{eff0}	3.4
Effective group index n_g	3.6
Transparent carrier density N_T(10^{18} cm^{-3})	1
Line-width enhancement factor a_m	4.571
Confinement factor Γ	0.3
Nonlinear gain coefficient ε (10^{-16} cm^3)	1
Spontaneous coupling coefficient β	5×10^{-5}
Petermann factor K	1
Reference temperature T_r (K)	300
Series thermal resistance R_s(Ω)	7
Reciprocal of thermal capacity R_t(10^8 K/J)	3.87
Thermal diffusion coefficient D (10^{-5} m^2/s)	2
Characteristic temperatures T_g, T_s (K)	70
Thermal constant for refractive index change α (10^{-3}/K)	2.28
Active region band gap energy E_g (eV)	0.8
Distance between active region and heat sink h (μm)	3.5

Static State Simulation

Firstly, we applied the iterative procedure described in Figure 3.2b to calculate the static characteristics of the laser diode under different heat sink temperatures. In Figure 3.13, temperature-dependent L-I curves simulated by our model are compared with that neglecting the thermal effect. Due to the thermal effect, at high-injected current, the output power is saturated and presents a nonlinear relation with the injection current. Also, as the heat sink temperature rises, the threshold current increases, which is a phenomenon consistent with the experimental observation [12].

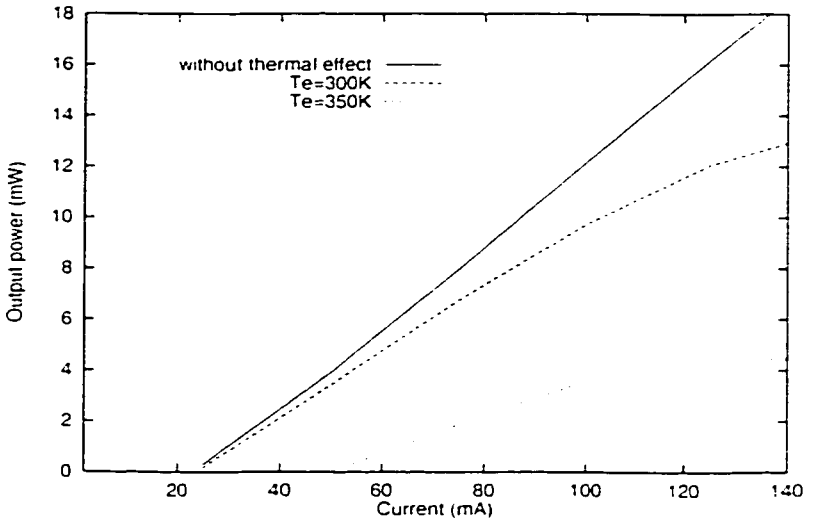

Figure 3. 13 Output power as a function of bias current at different temperature for a DFB laser.

Transient State Simulation

Secondly, we carried out transient simulation with consideration of thermal process. The transient state may be readily simulated by solving the governing equations for the traveling wave optical field, the carrier density, and the temperature as described in Figure 3.2a. In Figure 3.14, we show the output power change vs. time. The initial state biased current is 25 mA, which is reached by the iteration approach discussed before. A bias current of 50 mA is switched on at t=0 and kept on the laser diode for t>0.

We can see that, after about one nanosecond, the output power appears to reach a constant value, which is however not the static state value. Because the thermal time constant is very large, after a few nanoseconds, although the output power change is almost invisible, the heat up process is still going on. The heat up process results in a wavelength chirp, which is shown in Figure 3.15. It should be mentioned that in the traveling wave model spectrum calculation, FFT method is used as shown in [1,2]. Normally it requires multi-runs of the simulator and during the calculation, a large memory is needed to store the output complex field at very small time step, which is determined by Nyquist theorem [11,10]. In our simulation, we used the transfer matrix approach [13,14].

Time Constant under Direct Modulation

Recently, a thermal time constant of the order of 20 ns is observed for a DFB laser under direct large signal modulation [9]. In this section, using the model we developed, a theoretical explanation is given to the phenomena by introducing a quasi-static thermal state concept. As we know, the time constant of the optical process is much smaller than the thermal one. Therefore, after the static states at initial time and final time are obtained. The temperature change vs. time can be calculated approximately using the thermal equation (3.22). In Figure 3.16, we show the temperature

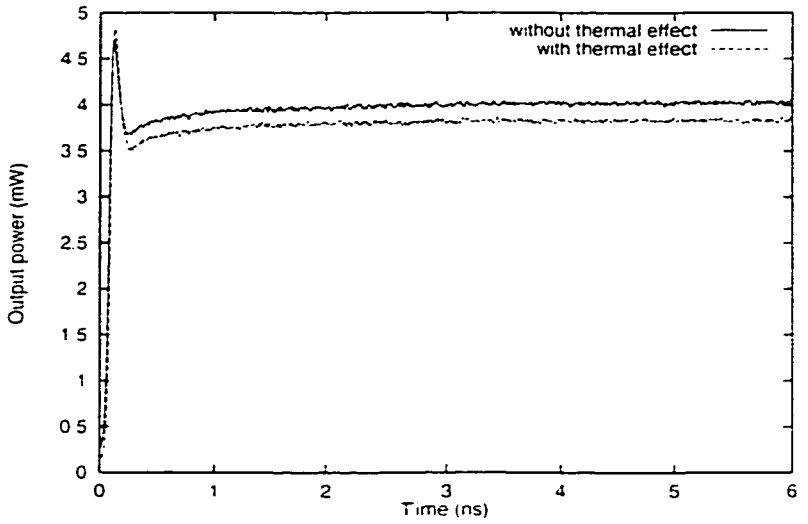

Figure 3. 14 Transient state output power as a function of time. The initial state is 25 mA biased static state. At time quual to zero, a 50 mA biased current is applied.

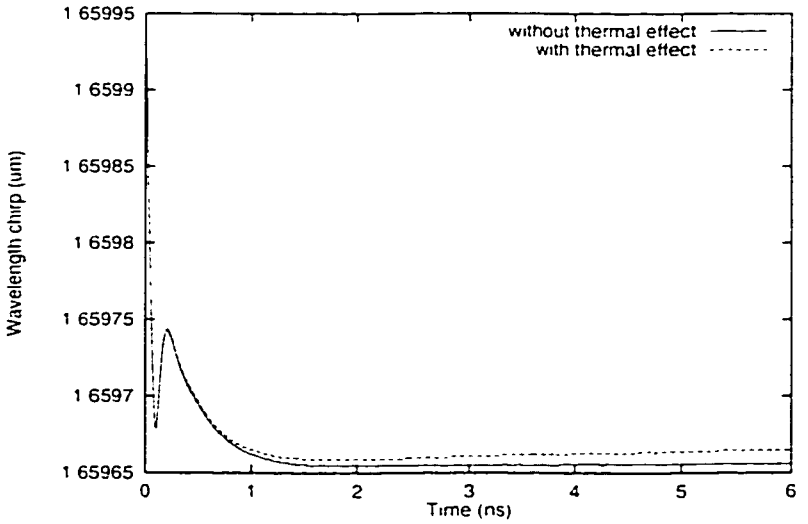

Figure 3. 15 Wavelength chirp during the transient state for the above operation

change at a step modulation. The modulation depth is 10 mA. We can see that time constant for the thermal effect is quite large, whose range is consistent with the commonly cited values 150 ns to several ms [3.5-8].

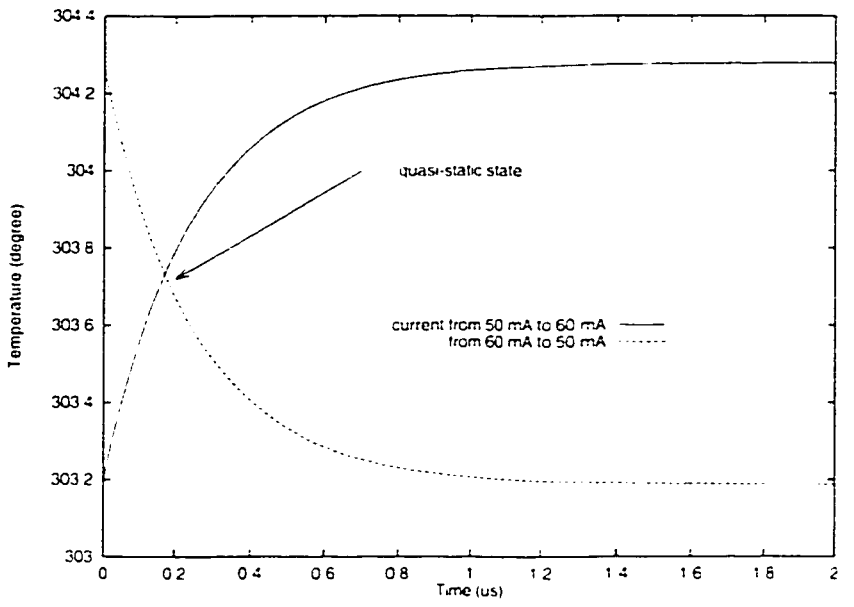

Figure 3. 16 Temperature change as a function of time. The initial state is a thermal static state. Then injected current suddenly change to another value.

To show the output power change and wavelength chirp, we first set the initial state as the static state of injected current equal to 50 mA, then a 12.5 Mb/s square wave modulation is applied to the diode with modulation depth equal to 10 mA. Figure 3.17 shows the simulation results.

In this simulation, we can not find the "balanced" frequency chirp observed in the experiment, instead, the up-going chirp time constant is much smaller than that of downward one. This phenomenon can be explained by a careful study of Figure 3.16. Since the initial state is set to 50 mA biased static state, as time goes on, the temperature change rate for heating up is much larger than that for cooling down, therefore the wavelength chirp shows an unbalanced shape. We also notice that at the curves inter-section region. Those two time constants mentioned before are almost equal. This region is a quasi-static thermal state. When laser diode is heated up to this region, since the two time constants are almost equal, the temperature will be trapped around this quasi-static point and begin to oscillate according to the modulation. Therefore, a balanced frequency chirp should be observed.

To verify our prediction, we set the initial state to the quasi-static state by resetting the initial condition of I_{s0} and X_{s0}, which is equal to the average of 50 mA and 60 mA static state values, i.e. the initial temperature is set equal to the quasi-static state temperature. The simulation results are shown in Figure 3.18, which agree with the experimental observation [9,10].

It should be noticed that no effort has been made to fit the experiment data. In fact, this quasi-static thermal state also has no relation with laser model used. We conclude that the short time constant observed comes from the temperature oscillation around the quasi-static state due to the periodic modulation. We also suggest that by a more precise experimental design, the unbalanced frequency chirp shown in Figure 3.17, which is an unstable state, should be observable.

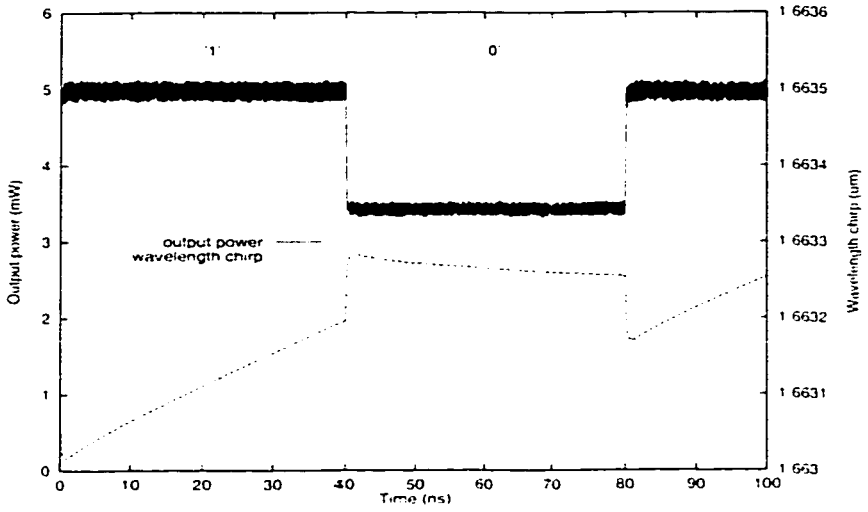

Figure 3. 17 Output power and wavelength chirp during the large signal modulation with modulation depth 10 mA. The initial state is 50 mA biased static state.

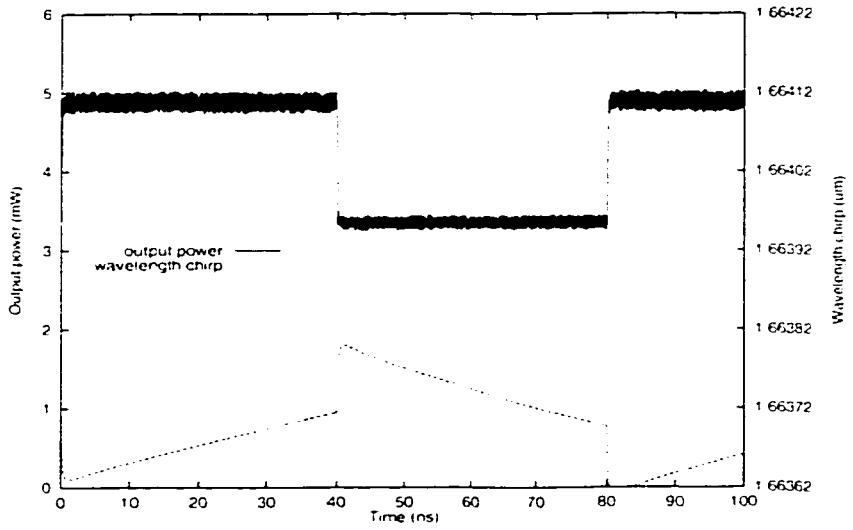

Figure 3. 18 Output power and wavelength chirp during the large signal modulation. The initial temperature is set around the quasi-state state region.

3.4.6 Series Ohmic Resistance Effects

In the previous applications, we have assumed that the injected current is distributed uniformly within the whole section. Using the theory presented in 3.3.3, we give a brief discussion on the series ohm resistance effects based on a λ/4 phase-shifted laser. During the simulation, we assume the temperature equal to 300K, n=p=N, and inverse Fermi function takes the form

$$F_{n,p}^{1/2}(x) = \ln\left|\exp(1/0.3\sqrt{1+0.6x}-1)-1\right| \tag{3.45}$$

where $x=N/N_{n,p}$, and $N_n=2.1x10^{23}\ m^{-3}$, $N_p=1.3x10^{25}\ m^{-3}$.

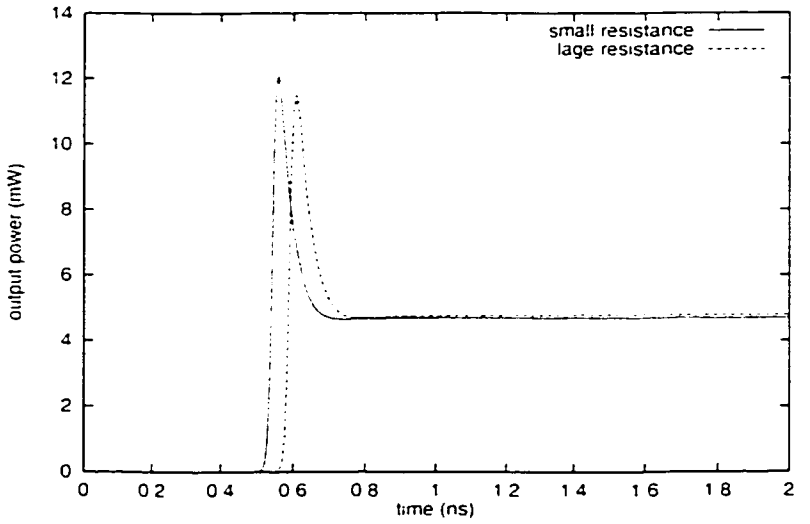

Figure 3. 19 Comparison of the transient state for different series Ohm resistance.

We will calculate the cases for large bulk resistance R=2Ω, and small bulk resistance R=1Ω respectively. In Figure 3.19, we show the transient state reaction of the two cases, it can be seen that for small series resistance, the reaction of the laser will be faster. In Figure 3.20, the L-V curves of the two cases are compared, it is obvious that for the same applied voltage, the small series resistance laser will provide higher output power.

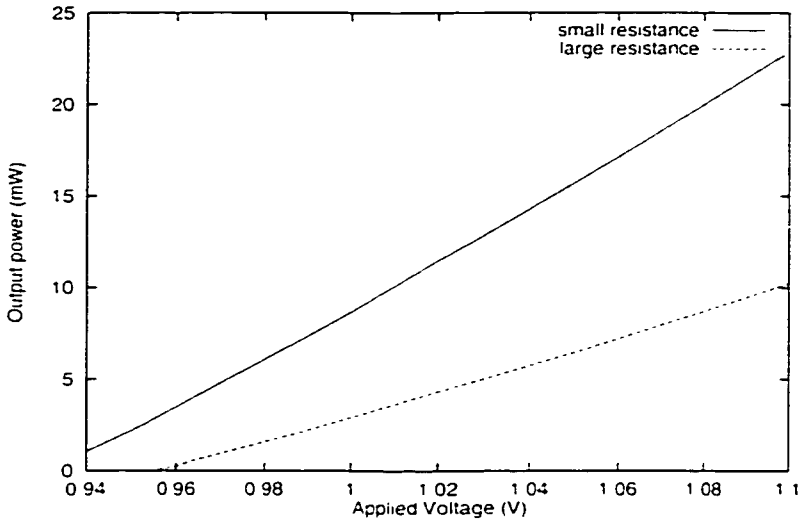

Figure 3. 20 Output power vs voltage applied for different series Ohm resistance.

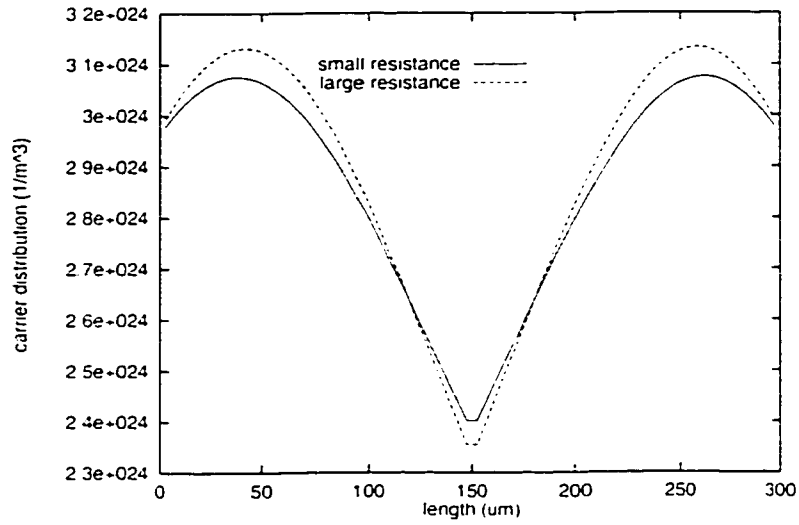

Figure 3. 21 Carrier distribution comparison with the same output power.

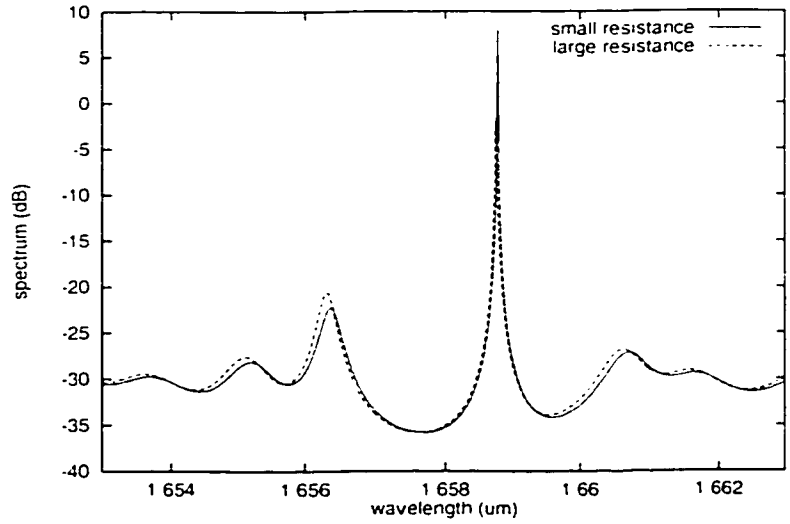

Figure 3. 22 Spectrum comparison with the same output power.

Finally, we compare the carrier distribution and output spectrum between the two cases in Figure 3.21 and Figure 3.22, respectively. Because of the compensation of the current distribution, if the series resistance is small, the spatial hole burning effect will not be so obvious as the case of large series resistance; therefore the MSR is also better. Although, the series Ohm effect is not so obvious, it is suggest that it should be considered in the laser design.

3.5 Summary

In this chapter, we have presented a comprehensive traveling wave laser diode model. Especially, we have emphasized the difference between the traveling wave model and the standing wave model and incorporated the thermal effect into the traveling wave approach for the first time. To show the versatility of the model, a few application examples are presented. In this chapter, for the first time, we gave a theoretical explanation on the various thermal time constants during the large signal modulation observed experimentally.

The traveling wave model is powerful in both static and dynamic simulations of the laser diodes. On the other hand, it is a challenging task to handle the problems such as complicated frequency dependent gain profile or extra long passive device cascaded with the active laser section, where the standing wave may be quite efficient. In the following chapter, we will introduce a split step approach to compromise the two models and improve the traveling wave approach.

Chapter 4

Split Step (Digital Signal Processing) Approach in the Traveling Wave Model for Laser Diodes

4.1 Introduction

As we mentioned in the previous chapters, the standing wave model and the traveling wave model are both commonly used in the laser diode simulation and design. The standing wave model is very efficient in the simulation, especially for the static state cases. On the other hand, it also has inherent physical limitation due to the assumption of the instantaneous creation of standing wave modes in the laser cavity. Compared with the standing wave model, the traveling wave model implementation will trace the waveform both in space and time domains with the numerical convergence up-limit constrain $\Delta z = v_g \Delta t$. Therefore it avoids searching the complex roots, which is corresponding to the longitudinal modes of the laser cavity, and hence is easy to be extended to the multi-section cases. However, traveling wave model also has some

shortcomings, which is related to tracing the waveform in both time and spatial domains with the signal transmission speed constrain $\Delta z = v_g \Delta t$.

One of the drawbacks for the traveling wave model is that it tends to be quite time-consuming when the total optical length of the device becomes long. For instance, for a laser diode cascaded with a long DBR section (e.g., a fiber Bragg grating), it takes a long time for the traveling wave approach to trace the waveform all the way along the entire passive section. Furthermore, under certain circumstances, the passive section may be characterized in terms of measured spectral responses and therefore difficult to be modeled in a self-consistent traveling wave form as for the laser diode.

To overcome the above shortcomings of the full traveling wave model, we try to compromise the standing wave model and the traveling wave models based on the digital signal processing technique. In this chapter, we propose a digital filter or a split step approach in the traveling wave model. By modeling the passive sections along the optical path as digital filters, we can simulate the counter-propagating waves by a combination of the standard evolution scheme (as done in the full traveling wave model) and the convolution scheme commonly used in digital filters. It is demonstrated that the new method is much more efficient than the full traveling wave model. In addition, we can readily incorporate the spectral properties of the passive sections, which can be obtained from measurements and/or other analytical and numerical models.

In the following sections, we will first present a detail description of the theory on digital filter approach and its implementation in traveling wave model. Then this model is to be compared with the full traveling wave model and its validity is verified. Thirdly we will apply this digital filter approach to the case of fiber grating stabilizer on laser diode. Finally we will give a brief summary.

4.2 Digital Filter Approach

As we presented in the previous section, both traveling wave and standing wave approaches have their advantages and shortcomings. Therefore, a split step/digital filter method is proposed, which combines the two approaches into one general model. In this section, we will present a detail theoretical explanation on the digital filter or the split step approach and its numerical implementation in the traveling wave model for laser diode.

4.2.1 Theory on Digital Filter

Fourier Transform

It is well known that a physical phenomenon can be described in both time domain and frequency domain. For example, the electric field of photons can be expressed either as $F(t)$,i.e., a time sequence in time domain or as $\tilde{F}(f)$,i.e., a frequency dependent field profile in frequency domain. They are the two different representations of the same physical function, and these two representations are transformable by the Fourier transform equations

$$\begin{aligned} \tilde{F}(f) &= \int_{-\infty}^{+\infty} F(t)\exp(-j2\pi ft)\,dt \\ F(t) &= \int_{-\infty}^{+\infty} \tilde{F}(f)\exp(-j2\pi ft)\,df \end{aligned} \tag{4.1}$$

Convolution of two functions denoted by $h \otimes f$ is an important operation, which is defined by

$$h \otimes f(t) = \int_{-\infty}^{+\infty} h(\tau) f(t-\tau) d\tau \qquad (4.2)$$

Although mathematically, $h \otimes f = f \otimes h$, these two functions have different physical meanings. f is a signal stream, and h is a response function acting on the signal, which usually is a peak function and falls to zero when time is far from the peak point. This interaction response has a simple representation in the frequency domain, i.e.

$$\overline{h \otimes f} = \tilde{h}\ \tilde{f} \qquad (4.3)$$

In reality, which representation should be chosen in the simulation is totally problem dependent. In the following section, we will make full use of the two different representations and the Fourier transformation technique. The split step/digital filter approach uses the time domain representation to describe the dynamics of the active sections of the laser diode, and uses the frequency domain representation to describe the long complex structure of the passive section. Finally a time domain digital filter, which is connecting these two representations into one picture, describes the interaction between these two sections.

Sample Theorem

During the simulation, the optical signal/field is in discrete form with the evenly time spaced interval Δt, so that the sampled field could be expressed as

$$F'' = F(n\Delta t) \qquad (4.4)$$

There is a special frequency called Nyquist critical frequency associated with the time interval Δt, which is given by[3,4]

$$f_c = \frac{1}{2\Delta t} \tag{4.5}$$

Nyquist critical frequency is an important concept. Because the sampling theorem states that if a continuous time domain function $F(t)$ is bandwidth limited by $2f_c$, i.e., $\tilde{F}(f) = 0, \quad \text{if} \quad |f| \geq f_c$, then the function $F(t)$ is completely determined by the sample function F^n at time interval Δt. It is proved that [3,4,6]

$$F(t) = \Delta t \sum_{-\infty}^{\infty} F^n \frac{\sin(2\pi f_c (t - n\Delta t))}{\pi(t - n\Delta t)} \tag{4.6}$$

Sampling theorem tells us two important facts, which should be considered in the simulation. One is that if we know the band-width of the optical field in the frequency domain, the simulation time interval should be chosen to be smaller than $1/2f_c$. In fact, in a real simulation problem, the band-width is usually limited or approximately band-width limited. For example, the laser active section gain profile has a finite band-width in frequency domain, and normally the wavelength-selection part (DFB or DBR structure) also has a limited band-width. The other fact should be considered is that if the band width of signal is not less than the Nyquist critical frequency, the power spectral density outside the Nyquist region will be aliased falsely into the frequency domain within the range $(-f_c, f_c)$. This phenonmenon is called aliasing[3,4]. We show it schematically in Figure (4.1) To overcome the aliasing, after simulation, we should check the output spectrum to see whether the power spectral density outside the range $(-f_c, f_c)$ equal to zero or very small compared with the other region. If this condition is

not satisfied, aliasing may occur. We should rearrange the time interval of the simulation Δt until the condition is satisfied.

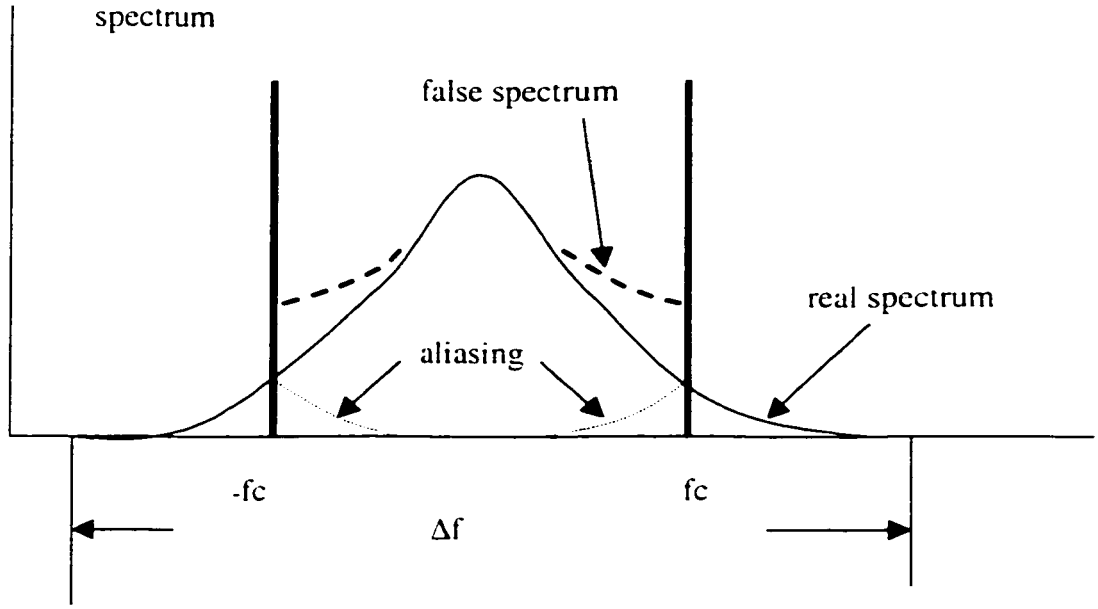

Figure 4. 1 Power spectrum aliasing due to Nyquist critical frequency range ($-f_c, f_c$) less than the signal band width.

The discrete Fourier transform from eqn.(4.1) can be written as

$$\tilde{F}^n = \sum_{k=0}^{N-1} F^n \exp(2\pi jkn / N)$$
$$F^n = \frac{1}{N} \sum_{k=0}^{N-1} \tilde{F}^n \exp(-2\pi jkn / N) \tag{4.7}$$

This discrete Fourier transform is implemented by the fast Fourier transform (FFT) technique.

Digital Filter in Time Domain

In previous sections, it is shown that complicated filter response function in time domain can be easily expressed in frequency domain. The filter solved purely in frequency domain is called the acausal type[4]. It requires a batch of signal data to perform the Fourier transform, therefore the response signal at a specific time depends not only on the signal stream before that time, but also on the signal stream after that time. However, in real time simulation, since we only have a continuous data stream before a specific time and we want to know the response signal at this time. Therefore it is impossible to solve the problem totally in frequency domain. Therefore a time domain digital filter is introduced, and it is also called causal or physically realizable type filter[3,4].

There are two kinds of commonly used causal filter. They are defined as[3,4]

$$F^n = \sum_{k=0}^{M} D^k X^{n-k} + \sum_{k=1}^{N} C^k F^{n-k} \tag{4.8}$$

where X is the coarse signal and F is the signal after filtering. D^k and C^k are the digital filter coefficients. If $C^k \equiv 0$, this filter is called non-recursive filter; otherwise, it is called recursive filter. It is shown that in the time domain digital filter approach, the response field at a specific time $n\Delta t$ is determined by the previous $M\Delta t$ coarse signal information and previous $N\Delta t$ filtered signal. The time domain digital filter

coefficients in eqn(4.8) are determined by the response function of the filter in frequency domain.

$$\tilde{H}(f)=\frac{\sum_{k=0}^{M} D^k \exp[-2\pi jk(f\Delta t)]}{1-\sum_{k=0}^{N} C^k \exp[-2\pi jk(f\Delta t)]} \tag{4.9}$$

We can derive eqn(4.9) easily from the Fourier transform of eqn.(4.8)

Now we have a reverse problem. Digital filter coefficients C^k and D^k can be obtained by fitting eqn.(4.9) to the response function of the filter in frequency domain. Then using eqn.(4.8), the signal can be processed digitally in time domain. It should be noted that the gain profile filter used in the last chapter is just a recursive digital filter with two coefficients. Therefore, the frequency response profile forms, which this gain filter can be described, are limited. Theoretically speaking, we may use the theory presented in this chapter to simulated more complicated gain profile.

4.2.2 Numerical Implementation of Digital Filter

We assume that photon field/signal emitted from the active region will pass through and be reflected from the passive section, which we regard as a frequency filter. If this approach is implemented using the full traveling wave model, the waveform should be followed step by step in both time and space domain just as shown in the previous chapter. However, for a linear passive section, if its reflectivity and transmission are known. In frequency domain, this process is merely a multiplication of response function $\tilde{R}(f)$ *and* $\tilde{T}(f)$. The response functions may be calculated analytically, simulated by other software or even measured from experiment.

For the passive sections in absence of nonlinearity, the governing equations for the envelopes F (z,t) and R(z,t) of the forward and backward traveling optical fields are

$$\begin{aligned} \frac{1}{v_g}\frac{\partial F}{\partial t}+\frac{\partial F}{\partial z} &= (\alpha - j\delta_o)F + j\kappa_F R \\ \frac{1}{v_g}\frac{\partial R}{\partial t}-\frac{\partial R}{\partial z} &= (\alpha - j\delta_o)R + j\kappa_R F \end{aligned} \tag{4.10}$$

As the governing equations are linear, we may perform a Fourier transform so that we have

$$\begin{aligned} \frac{\partial \tilde{F}}{\partial z} &= (\alpha - j\delta)\tilde{F} + j\kappa_F \tilde{R} \\ -\frac{\partial \tilde{R}}{\partial z} &= (\alpha - j\delta)\tilde{R} + j\kappa_R \tilde{F} \end{aligned} \tag{4.11}$$

Eqn (4.11) can be readily solved by using the transfer matrix method for arbitrary α, δ, κ and the characteristic matrix of the passive section can then be found by the multiplication of the transmission of the each subsection along the wave-guide axis[5]. We may further convert the characteristic transfer matrix into the scattering matrix with the reflection coefficient and transmission coefficient from the passive section given by a complex function $\tilde{R}(f), \tilde{T}(f)$ respectively. Of course, these response functions could also obtained from more accurate simulation results or even experimental measurement.

In the digital filter implementation, the causal or physically realizable filter is used, which provides the output at a specific time based on the inputs at that specific time or earlier. As we introduced in the previous section, there are two commonly used linear filters in this category. One is recursive filter; the other is non-recursive one. It is

argued that for the same number of coefficients, the recursive filter is usually more accurate than the non-recursive one [4]. However, if coefficients are not chosen well, recursive approach may cause unstable solutions. Since in our applications, the number of coefficient is not of great concern. We adapt the non-recursive filter in the simulation.

The output points F_{out}^{n} at a specific time can be expressed by the N input points in the laser active section end F_{M}^{k} at this specific time and earlier as

$$F_{out}^{n} = \sum_{k=0}^{N} T^{k} F_{M}^{n-k} \qquad (4.12)$$

where subscribe M denotes the end node of optical field in the space discretization. T^{k} is the digital filter coefficients, which can be determined from response function, i.e., the transmission coefficient from frequency domain

$$\tilde{T}(f) = \sum_{k=0}^{M} T^{k} \exp(-2\pi i k f \Delta t) \qquad (4.13)$$

Comparing eqn (4.13) with eqn. (4.1) or (4.7), we find that digital filter coefficients T^{k} could be obtained easily by a reverse FFT transformation of the transmission coefficient in frequency domain, and eqn (4.12) is just a discrete expression of the convolution formula eqn. (4.2).

Similarly, the reflected field from the passive section in the active section end R_{M}^{n} at a specific time can also be expressed by the N input points F_{M}^{k} at this specific time and earlier as

$$R_M^n = \sum_{k=0}^{N} R^k F_M^{n-k} \qquad (4.14)$$

where R^k is the digital filter coefficients, which can be determined from response function ,i.e., the reflectivity coefficient from frequency domain

$$\tilde{R}(f) = \sum_{k=0}^{M} R^k \exp(-2\pi i k f \Delta t) \qquad (4.15)$$

Therefore, if a laser diode is cascaded with a long passive section, we can first calculate or even use the measurement data to get the reflectivity and transmission spectrum in frequency domain, then use eqns.(4.13) and (4.15) to get the reflectivity and transmission filters' coefficient. Instead of tracing the wave along the passive section, these two effective digital filters will be mounted at the end of the laser diode to simulate the whole passive section. The algorithm is shown schematically in Figure (4.2)

It should be noted that (i). during the simulation, Δt should be small enough to make the Nyquist critical frequency range $(-f_c, f_c)$ cover the passive section filter band width; (ii). the digital filter coefficient number N should be chosen such that $N\Delta t$ is comparable with the time delay, otherwise, the time delay in the passive wave-guide should be considered.

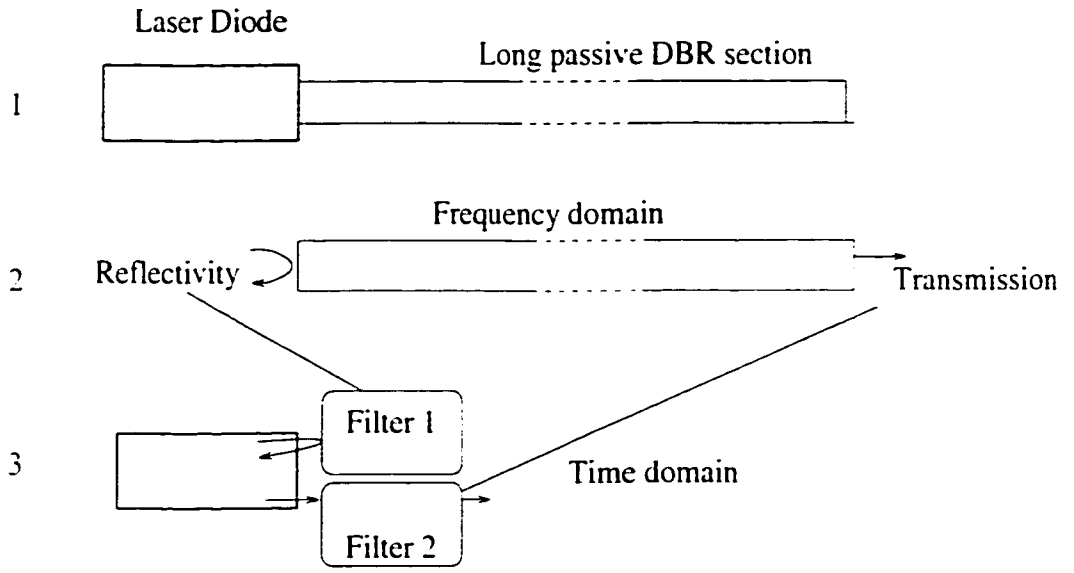

Figure 4. 2 Schematic of the digital filter approach for the traveling wave model of laser diode.

4.3 Comparison and Validation

To show the validity of the method presented in previous section, we will do a series of test using both the full travelling wave and the digital filter approaches as shown in Figure (4.3). There is a 300 μm long FP laser diode, and at the right end, a DBR with KL=1, with Bragg wavelength at 1.55μm and section length 300 μm. Between the laser diode and DBR, a uniform passive wave-guide without grating connects the two pieces together.

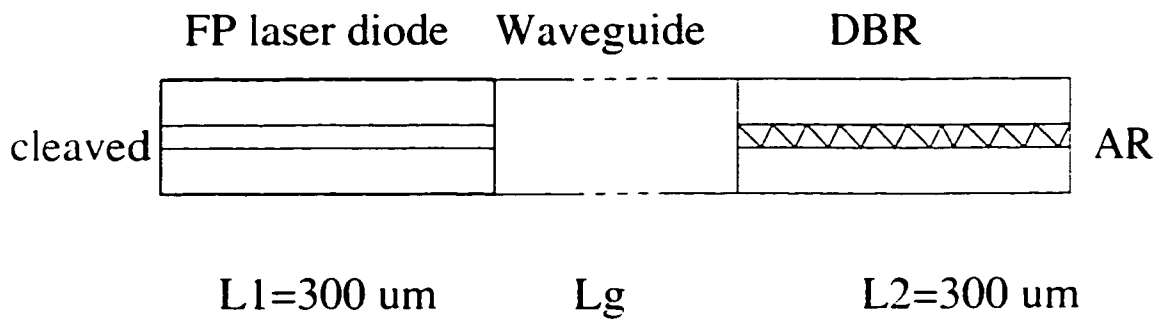

Figure 4. 3 The device used to do the comparison between the digital filter and full traveling wave approaches. Lg is changed from 0-1000μm.

We vary the length of wave-guide from zero to 1000μm, and compare the transient state, output power, carrier/photon distribution within the laser cavity and output spectrum obtained by the two methods. Figures (4.4-7) show the typical results. We can see that digital filter approach is in excellent agreement with the full traveling wave model.

However, while considering the simulation time between the two methods, the digital filter approach will show great advantage over the full traveling wave model, which has to tracing the wave-form all the way along the entire passive section. Figure (4.8) shows the comparison of the simulation time between the two approaches. To emphasize the generality, an arbitrary unit is used. Therefore, it is concluded that the digital filter approach provides an accurate yet efficient alternative method in the passive section simulation for the traveling wave model of laser diode.

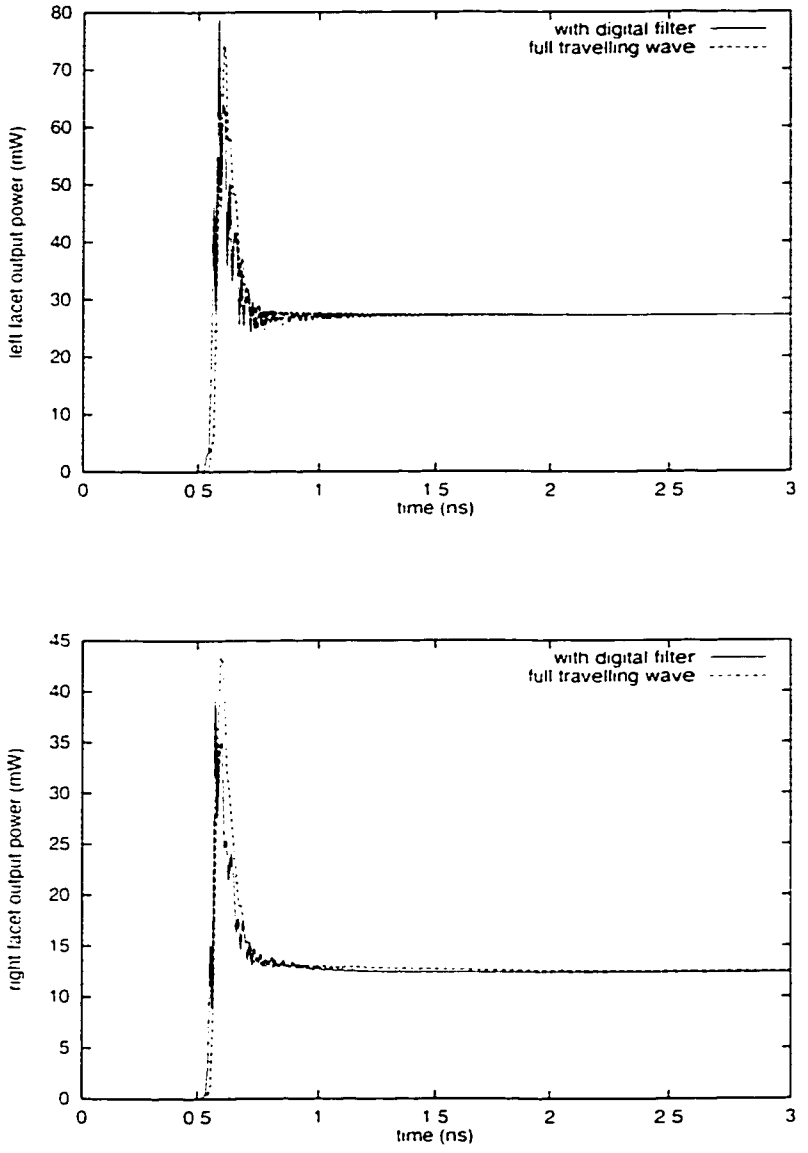

Figure 4. 4 The output power vs time comparison between the two methods. (a) left facet output power. (b) right facet output power. Here Lg=250μm. For other cases, similar results are obtained.

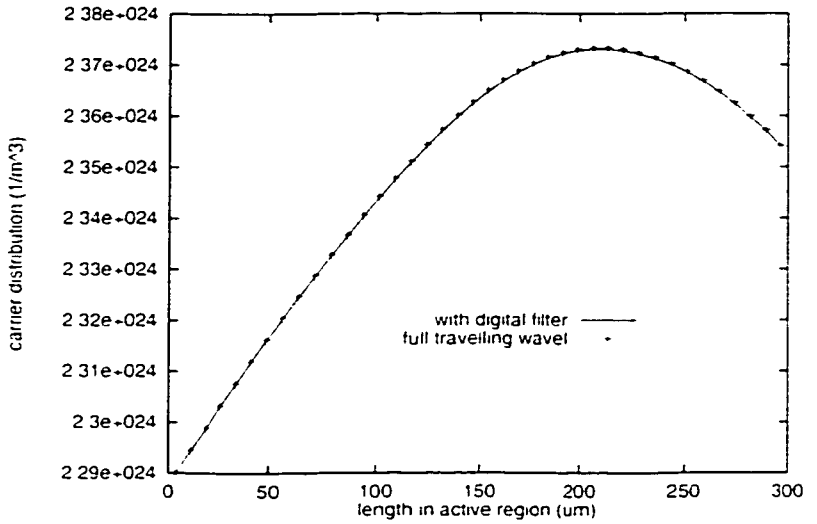

Figure 4. 5 Carrier distribution comparison between the two methods.

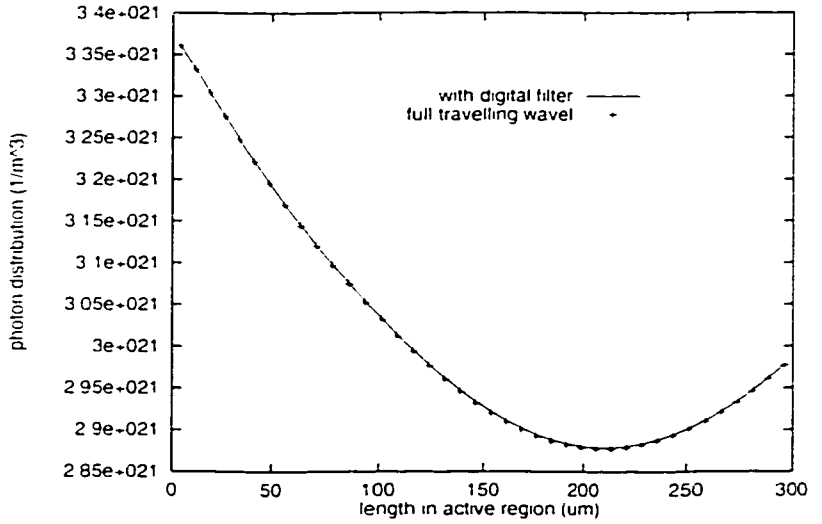

Figure 4. 6 Photon distribution comparison between the two methods.

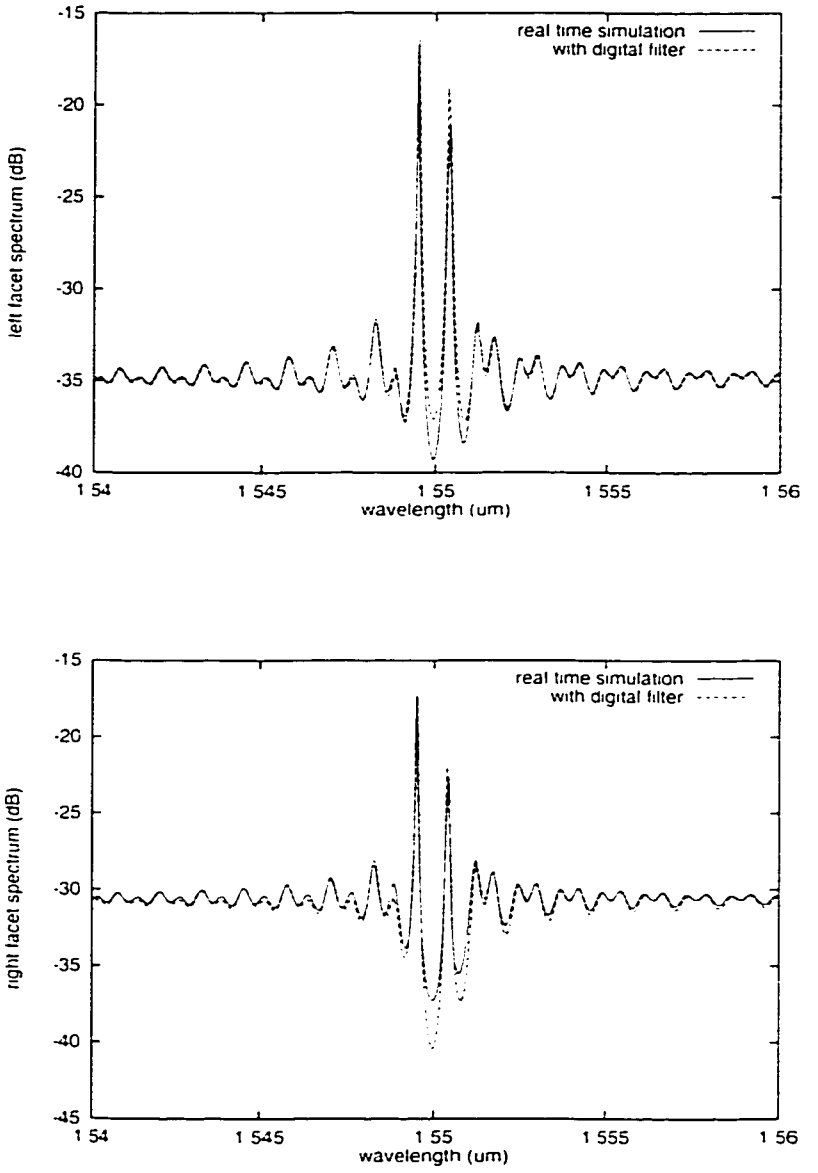

Figure 4. 7 The output spectra comparison between the two methods. (a) left facet spectrum .(b) right facet spectrum. Here Lg=0 μm. For other cases, similar results are obtained except there are more cavity modes.

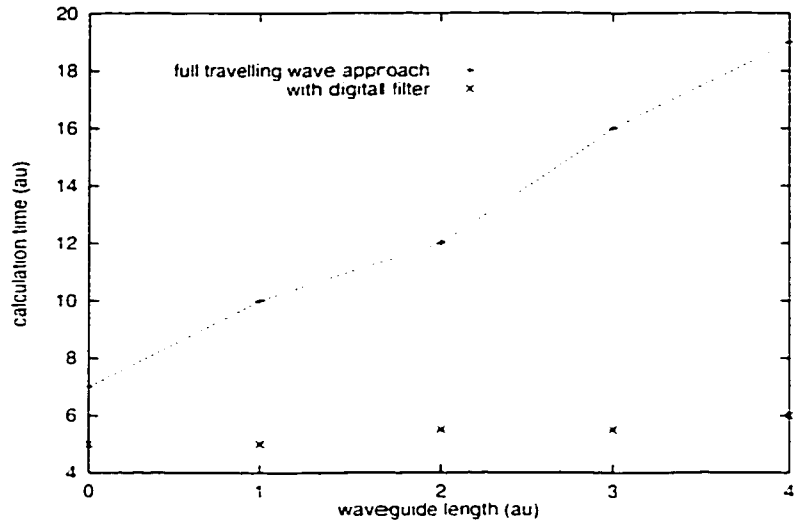

Figure 4. 8 Comparison of the CPU time used between the two methods

4.4 Fiber grating stabilizer laser diodes

In the WDM communication system, the wavelength spacing is down to 0.8nm (100Ghz)[1,2,6]. Therefore wavelength control is a critical issue. Fiber grating stabilizer cascaded with FP laser provides the required accurate wavelength in WDM system. In this section, to show the power of the split step/digital filter approach, by way of the model developed in previous section, we present some simulation results on this kind of laser diodes. The laser diode to be simulated is shown schematically in Figure (4.9).

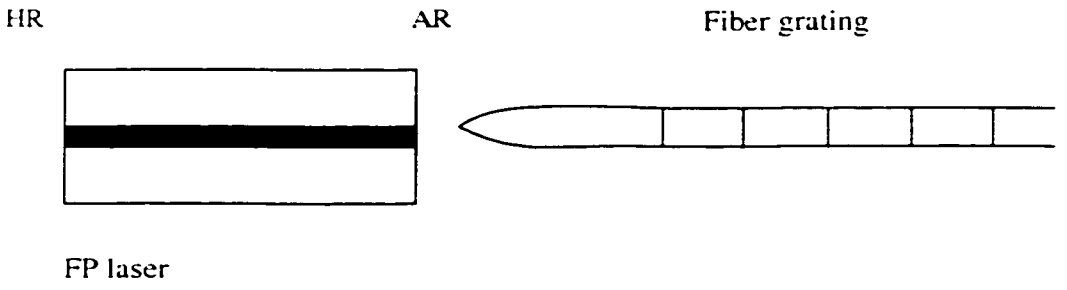

Figure 4. 9 Fiber grating stabilized laser diode.

The FP laser is HR coated in one facet, the other facet is AR coated and cascaded with a grating fiber, which is 5mm long with Bragg wavelength at 1.55μm and stop-band width around 0.3 nm. The air gap between the laser diode and fiber are simulated by an extra phase shift in the reflectivity and transmission spectrum of the grating fiber. We find that the output spectrum will be very sensitive to this phase, i.e., the air gap between the laser diode and fiber must be carefully adjusted to give the good single mode operation. Figures (4.10) and (4.11) show the L-I curve and the typical output spectrum of the laser diode.

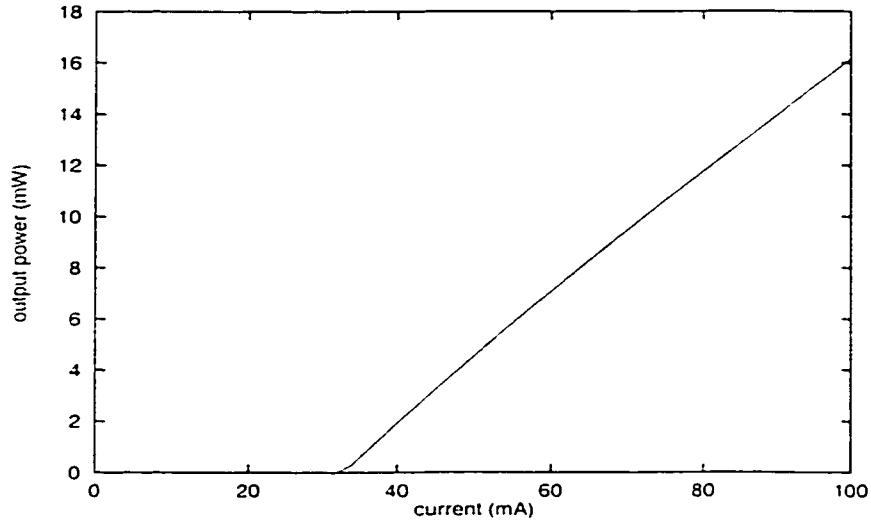

Figure 4. 10 L-I curve of the fiber grating stabilized laser diode.

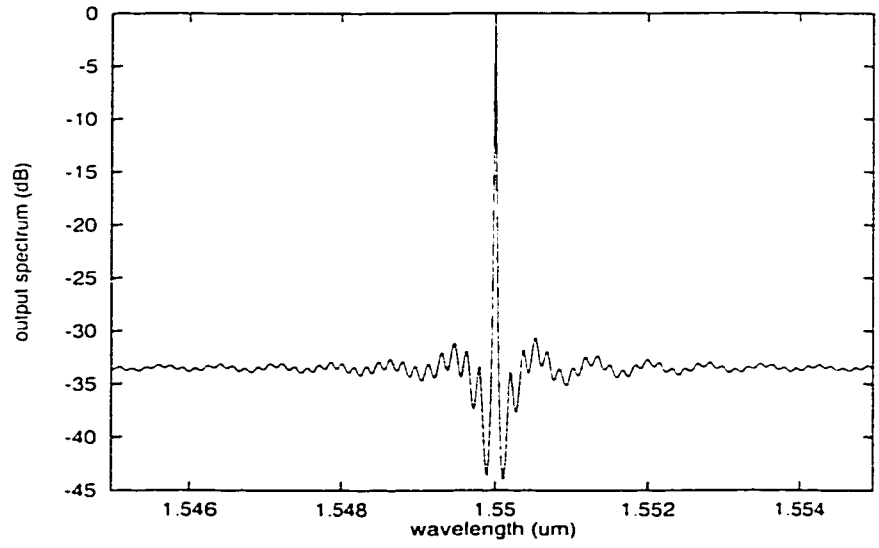

Figure 4. 11 Typical output spectrum of the fiber grating stabilized laser diode.

4.5. Summary

In this chapter, for the first time, we propose a split step/digital filter approach to the traveling wave model of laser diode. In the active region, the time domain traveling wave model is used, and in the passive section, the reflectivity and transmission are calculated by analytical method or measured from experiment in the frequency domain. Finally the response functions $\tilde{R}(f)$ and $\tilde{T}(f)$ are implemented as linear digital filters in the time domain to form a complete model with the active section traveling wave approach. It is proved that this new method is accurate and very efficient in the simulation of the complex passive section of the laser diode.

Chapter 5

Wavelength Tunable Laser Diode with Sampled Grating Structure

5.1 Introduction

Broadly wavelength tunable laser diodes are among the key components in wavelength division multiplexing (WDM) communication system [1.2]. The information capacity transmitted by a system increases linearly with the accessible number of wavelength channel, which the tunable laser diode can provide. Therefore, great efforts have been made to extend the tuning range of the semiconductor laser diodes. However, as we introduced in the previous chapters, stable single mode laser diode with large SMSR is of great importance in the long haul communication system. To realize the single mode performance, grating structures such as DFB or DBR are usually applied as wavelength selection elements. It seems that the tunable laser

concept is somewhat controversial to this requirement. In fact, for a tunable laser diode design, on one hand, it is required that the lasing wavelength should be tunable in a wide wavelength range. On the other hand, it is also required that the laser diode should operate with single mode and large SMSR at any wavelength, which it can access. That means, we should combine the wavelength selection element and tunable mechanism effectively to meet both requirements in a single device. Actually, in the following sections, we will demonstrate that these two requirements usually have to be compromised for a satisfactory laser diode performance.

Naturally, we begin to introduce the wavelength tunable laser with traditional multi-section DBR type laser to show the tuning mechanism and its limitation. The laser structure to be discussed is shown schematically in Figure (5.1). There are three sections in this tunable laser, one is an active FP laser cavity, one is the phase control section and the last one is a DBR reflector.

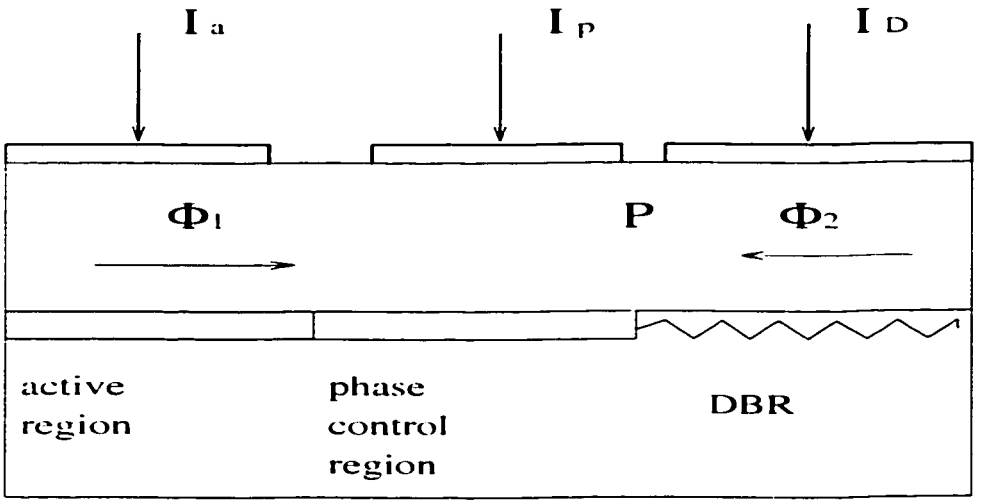

Figure 5. 1 Traditional multi-section DBR wavelength tunable laser.

Since the gain section and wavelength selective section in a DBR laser are spatially separated, we may discuss the two parts individually. To give more insight to the laser operation and tuning mechanism, in this introduction, unlike the previous two chapters, we will discuss the problems only in a phenomenological or analytical way. Firstly, let us focus on the DBR reflector with the structure as shown in Figure (5.2). Using the coupled mode theory, we can obtain the reflectivity spectrum of the DBR

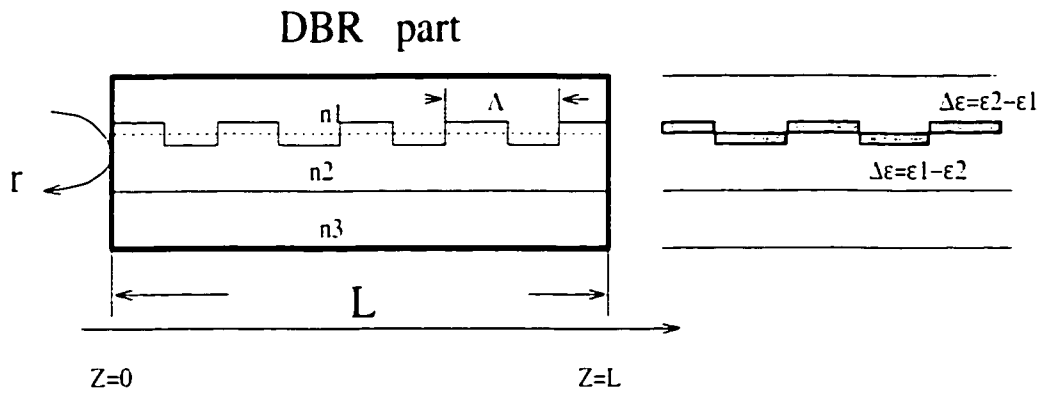

Figure 5. 2 DBR part of wavelength tunable laser.

From Maxwell equation, we derive

$$\nabla^2 E + k_0^2 \varepsilon^0 E = -k_0^2 \Delta\varepsilon E \qquad (5.1)$$

where $\Delta\varepsilon$ is a perturbation provided by the grating shown in Figure (5.2). If the electric field is expressed as

$$E = \Phi(x, y)[F(z)\exp(-j\frac{\pi}{\Lambda}z) + R(z)\exp(j\frac{\pi}{\Lambda}z) \qquad (5.2)$$

where Λ is the period of grating, and $\Phi(x,y)$ is the transverse field profile for a mode of propagation constant $\beta = (2\pi/\lambda)n_{eff}$, which is obtained by solving equation

$$[\nabla^2 + k_0^2\varepsilon^0]\Phi(x,y)\exp(-j\beta z) = 0 \tag{5.3}$$

Substituting eqns(5.2) and (5.3) into eqn.(5.1), we obtain the coupled mode equation

$$\frac{d}{dz}\begin{bmatrix}F(z)\\R(z)\end{bmatrix} = j\begin{bmatrix}\Delta\beta & k_{ab}\\ k_{ba} & -\Delta\beta\end{bmatrix}\begin{bmatrix}F(z)\\R(z)\end{bmatrix} \tag{5.4}$$

where $\Delta\beta = \beta - \frac{m\pi}{\Lambda}$, and coupling coefficients k_{ab} and k_{ba} are defined as

$$\begin{aligned} k_{ab} &= \frac{k_0^2}{2\beta}\int d_m(x,y)\,|\Phi(x,y)|^2\,dxdy \\ k_{ba} &= -\frac{k_0^2}{2\beta}\int d_{-m}(x,y)\,|\Phi(x,y)|^2\,dxdy \end{aligned} \tag{5.5}$$

where d_{zm} is the Fourier series expansion coefficient of $\Delta\varepsilon$

$$\Delta\varepsilon = \sum d_m \exp[-jm(2\pi/\Lambda)z] \tag{5.6}$$

For the first order grating case, after solving the coupled mode equations, if set R(L)=0, we can obtain the reflectivity of DBR at z=0

$$r = \frac{-k_{ab}^{*}\tanh(sL)}{js + \Delta\beta\tanh(sL)}$$

where s is the eigenvalue of the coupled mode equation defined by

$$s = \sqrt{|k_{ab}|^2 - (\Delta\beta)^2} \tag{5.7}$$

In Figure (5.3), we show the reflectivity vs the detuning factor for different coupling coefficients.

It is readily proved that the maximum reflectivity is at the point $\Delta\beta = 0$, i.e., at the wavelength

$$\lambda = 2n_{eff}\Lambda \tag{5.8}$$

This maximum reflectivity is corresponding to the minimum mirror loss of the laser cavity. To obtain a large SMSR, a narrow bandwidth of reflectivity spectrum is required. We can optimize the profile of the reflectivity by changing the coupling coefficient and the length of DBR section as shown in Figure (5.3).

Secondly, we will discuss the turning mechanism of the laser diode. To make the lasering wavelength tunable, we need to tune the reflectivity peak of DBR reflector. In previous chapter, we have shown that the refractive index of the semiconductor material can be changed by carrier injection, temperature variation, and applied electric field. The refractive index change will affect the mode effective refractive index and hence the reflectivity profile. Using perturbation theory, the effective refractive index change is expressed as

$$\Delta n_{eff} = \frac{\int n_b \Delta n \,|\, \Phi(x,y) \,|^2 \, dxdy}{n_{eff} \int |\, \Phi(x,y) \,|^2 \, dxdy} \tag{5.9}$$

where n_b is the background refractive index, and Δn is the refractive index change associated with carrier injection, temperature variation and applied electric field in DBR region, which could be calculated by the material simulator developed in the previous chapters or by experimental measurements. The integral is over the region where the refractive index is changed. If the effective refractive index is changed to n_{eff}, the maximum reflectivity point will change to the wavelength λ as shown in Figure (5.4).

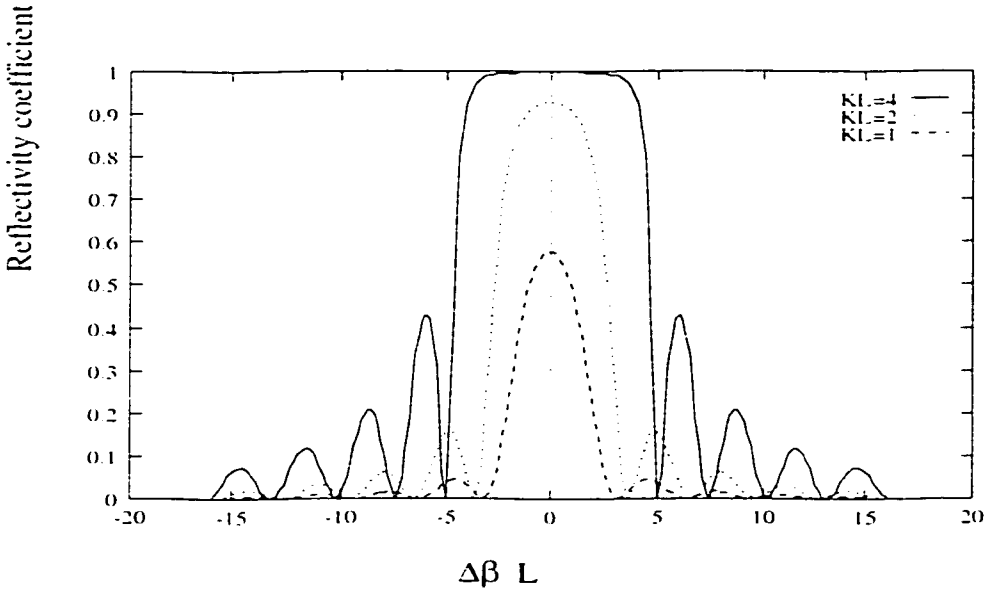

Figure 5. 3 Reflectivity vs detuning factor of a uniform DBR reflector.

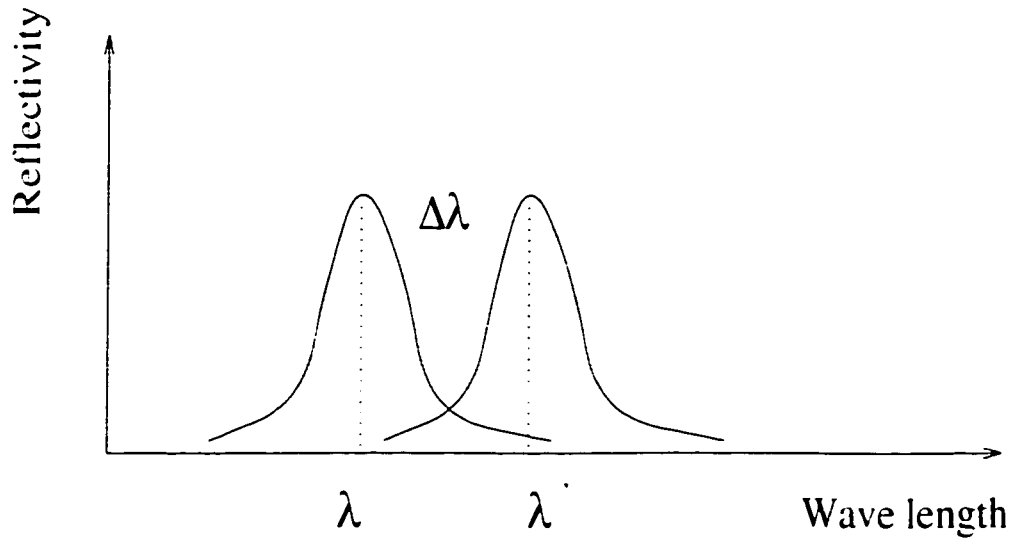

Figure 5. 4 Reflectivity profile change due to refractive index change of DBR

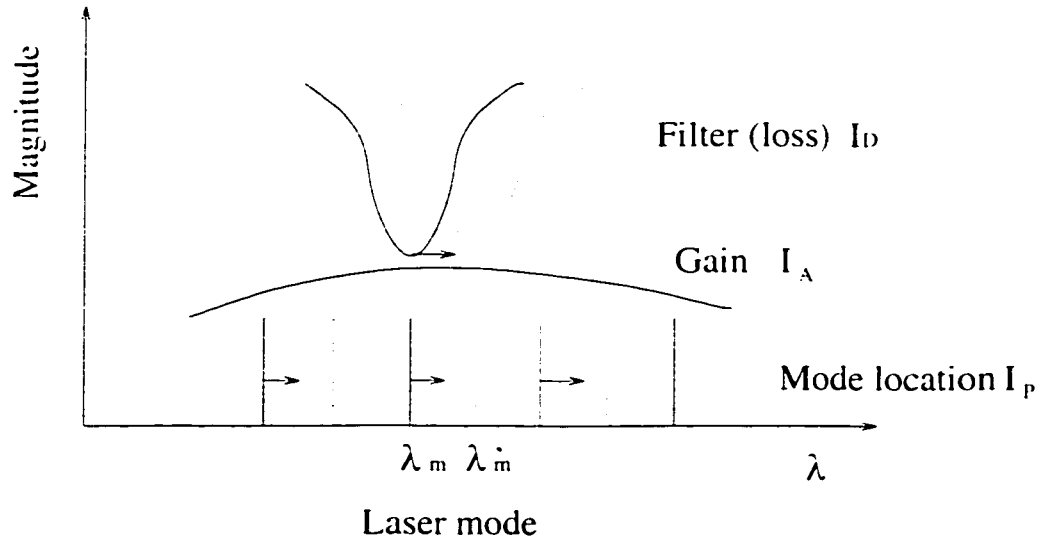

Figure 5. 5 Tuning mechanism of traditional DBR tunable laser diode.

For a multi-section DBR tunable laser, there is an additional phase control region between the active and the DBR sections as shown in Figure (5.1). By changing the current in the DBR section, the reflectivity profile and the mirror loss are shifted as shown in Figure (5.5). To obtain the maximum SMSR, we can adjust the current in the phase control region, and tune the wavelength of the FP laser mode to the same wavelength as the maximum of the DBR reflectivity or the minimum of the mirror loss. This situation is illustrated by Figure (5.5). The phase control region calibrates the laser mode wavelength to the mirror loss minimum wavelength. As the optical gain reaches its threshold value, the carrier density will clamp at its threshold level. Therefore, only one mode is excited, and a continuous single-mode DBR wavelength tunable laser is obtained. The tuning range is determined by the range of effective index change. From eqn (5.8), we have

$$\frac{\Delta\lambda}{\lambda} = \frac{\Delta n_{eff}}{n_{eff}} \tag{5.10}$$

For this simple DBR type tunable laser, the wavelength tuning range is primarily dependent on the material refractive index change. As we presented in the previous chapters, the maximum effective refractive index change achievable is around 0.7% by electronic means. Therefore, from eqn (5.10) these structures only have about 10 nm tuning range around the wavelength 1.55μm. This wavelength tuning range is much less than the gain profile bandwidth. For example, the gain bandwidth of quantum well material can be as large as 200nm. This bandwidth difference leaves great margin for increasing the tuning range of the laser diodes.

To fill this margin, new laser structures have been proposed. In this chapter, we will show one of such tunable lasers based on sampled grating structure.

In the following, we will first present a detail investigation on the physical properties of the sampled grating structure. Secondly, using the laser model developed in the previous chapters, we will present some simulation results on the DBR/vernier ruler type tunable lasers. With a co-directional filter as the wavelength-tuning/selection element, a DFB type sampled grating tunable laser is proposed and its operations are simulated.

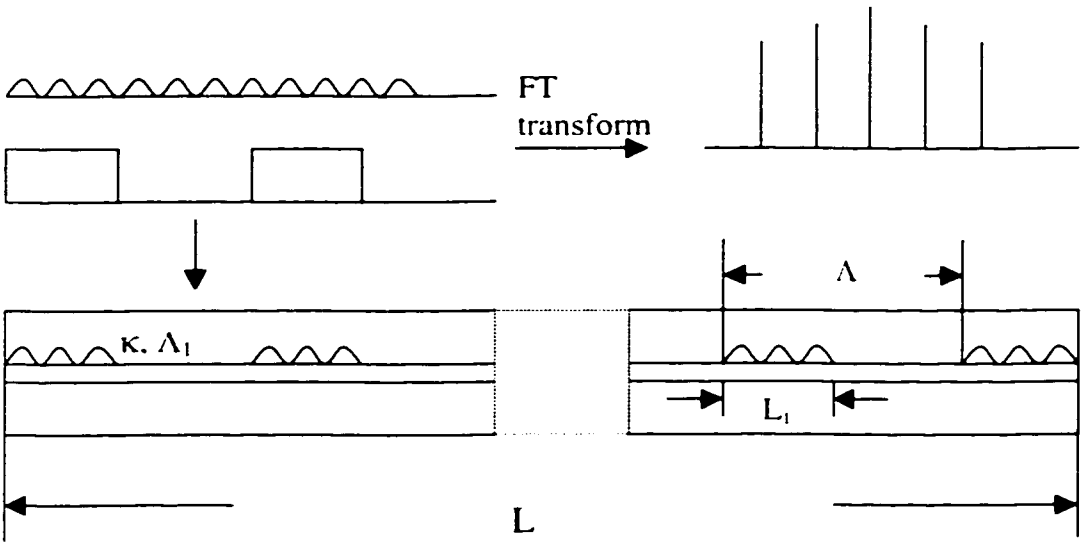

Figure 5. 6 Sampled grating structure

5.2 Sampled Grating Structure

The sampled grating structure is shown schematically in Figure (5.6). This structure can be regarded as a uniform Bragg grating with grating period equal to Λ_1 and coupling coefficient equal to κ multiplied by a sampling square function with period equal to Λ, and duty cycle equal to $x = L_1 / \Lambda$ [3]. The Fourier transform of this structure will give a comb like spectrum as shown in Figure (5.6) with the center at Bragg wave number, and higher order peaks distributed uniformly on the two sides.
To analyze this structure by using the coupled mode theory, we have the transfer matrix for each section

$$\begin{bmatrix} F(z^{m-1}) \\ R(z^{m-1}) \end{bmatrix} = T^{(m)} \begin{bmatrix} F(z^m) \\ R(z^m) \end{bmatrix} = \begin{bmatrix} T_{11}^{(m)} & T_{12}^{(m)} \\ T_{21}^{(m)} & T_{22}^{(m)} \end{bmatrix} \begin{bmatrix} F(z^m) \\ R(z^m) \end{bmatrix} \tag{5.11}$$

where

$$\begin{aligned} T_{11}^{(m)} &= \left[\cosh(s_m l^m) + \frac{(g_m - j\delta_m)}{s_m} \sinh(s_m l^m) \right] \exp(-j\beta_m l^m) \\ T_{12}^{(m)} &= \frac{-jk_m}{s_m} \sinh(s_m l^m) \exp(-j\beta_m l^m) \\ T_{21}^{(m)} &= \frac{jk_m^*}{s_m} \sinh(s_m l^m) \exp(j\beta_m l^m) \\ T_{22}^{(m)} &= \left[\cosh(s_m l^m) - \frac{(g_m - j\delta_m)}{s_m} \sinh(s_m l^m) \right] \exp(j\beta_m l^m) \end{aligned} \tag{5.12}$$

In this equation, $l^m = z^m - z^{m-1}$ is the section length. g_m is the net gain or loss in section m, which is a constant for the passive device. $\delta_m = 2\pi n_{eff} / \lambda - \pi / \Lambda_m$ is the

detuning factor for section m with Bragg grating period equal to Λ_m. $s_m = \sqrt{(g_m - j\delta_m)^2 + k_m^2}$ is the eigenvalue of the system, and $\beta_m = \pi / \Lambda_m$ is the Bragg wave vector of section m. It is noted that the coupling coefficient in the equation could be a complex number, which can be defined as

$$\begin{aligned} k_m &= k_0 \exp(j\theta_m) \\ \theta_m &= \theta_{m-1} + 2\beta_{m-1} l_{m-1} \end{aligned} \tag{5.13}$$

Cascading the transfer matrix section by section, we finally obtain

$$\begin{bmatrix} F(0) \\ R(0) \end{bmatrix} = \prod T^{(m)} \begin{bmatrix} F(L) \\ R(L) \end{bmatrix} = T_{total} \begin{bmatrix} F(L) \\ R(L) \end{bmatrix} \tag{5.14}$$

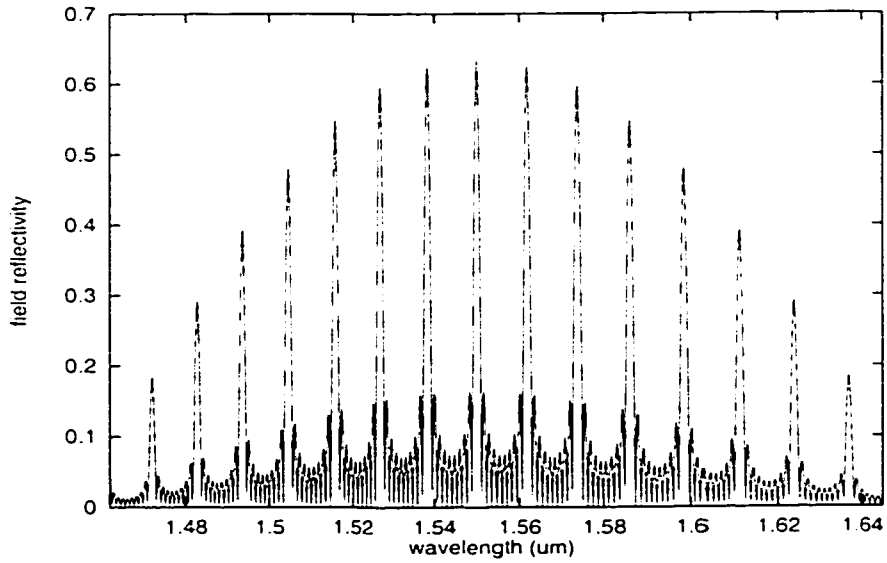

Figure 5. 7 Reflectivity profile of a sampled grating DBR reflector

Therefore, we can investigate the properties of sampled grating structure analytically according to eqn (5.14). A typical reflectivity profile of a sampled grating structure is shown in Figure (5.7).

It is easy to show that (i) the main peak is located at the grating Bragg wavelength $\lambda_0 = 2n_{eff}\Lambda_1$; (ii). the peak's interval is approximately equal to $\Delta\lambda = \lambda^2/(2n_{eff}\Lambda)$; (iii) if the duty cycle $x = L_1/\Lambda$ is decreased, there would be more peaks in the reflectivity profile; (iv).since the coupling coefficient is limited, to maintain the reflectivity peak amplitude, the duty cycle should be large enough.

With the comb-like reflectivity of sampled grating structure, in the following sections, we will discuss its application in the content of tunable laser diodes.

5.3 DBR Type (Vernier Ruler) Tunable Laser

As we demonstrated in the introduction, the uniform grating DBR reflector provides a maximum reflectivity peak profile, which also corresponds to the minimum loss of the laser cavity at a certain wavelength. This wavelength will be the lasing mode as the optical gain reaches its threshold value and be clamped. However, it was also pointed out that, for the traditional uniform grating DBR type tunable lasers, the wavelength tuning range is limited to around 10nm. With the multi-peak comb-like reflectivity profile of the sampled grating structure, based on the idea of vernier ruler, we could extend the tuning range of a DBR type laser dramatically.

The laser structure is shown schematically in Figure (5.8). There is a sampled grating structure at each side of the active section. The two structures have different sampled grating periods, and hence the peak interval is different for the two sampled grating's reflectivity profiles. The total reflectivity maximum or the total minimum

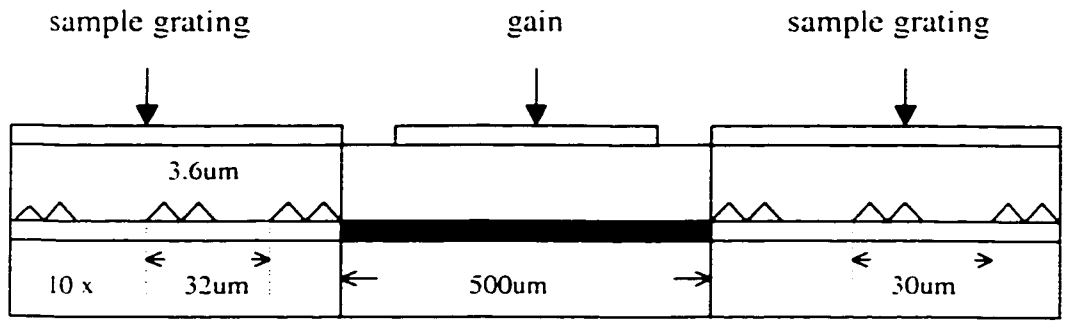

Figure 5. 8 Tunable laser structure with sampled grating DBR reflector.

mirror loss of the cavity is located at the wavelength where the two peaks of reflectivity profiles lining up as shown in Figure (5.9). This wavelength will be the lasing wavelength. As we know, a vernier ruler can be used to measure very small distance with two-mismatched ruler structures. The sampled grating structure DBR laser borrows this idea to extend the wavelength tuning range. As shown in Figure (5.9), we may fix one of the reflectivity profiles, for example, left side DBR, then change the refractive index of the other side by carrier injection or applied electric field. The tiny change of refractive index and hence the central wavelength of right side reflectivity profile will lead to the adjacent peaks lining up. Therefore a discrete wavelength tunable laser with large tuning range is obtained. As shown in Figure (5.9), we can also tune the wavelength continuously by moving the reflectivity profiles of both DBRs in the same direction equally after the wavelength of one channel is located.

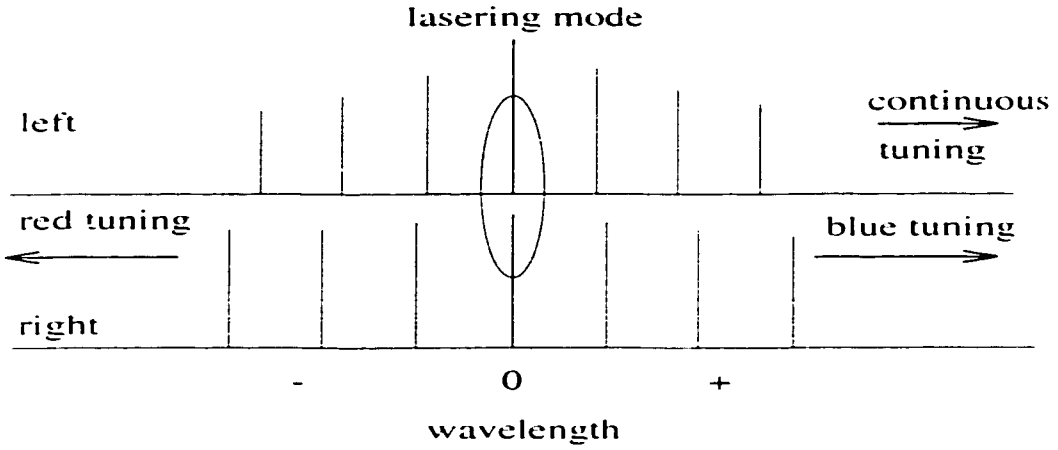

Figure 5. 9 Tuning mechanism of sampled grating DBR type (vernier ruler) wavelength tunable laser

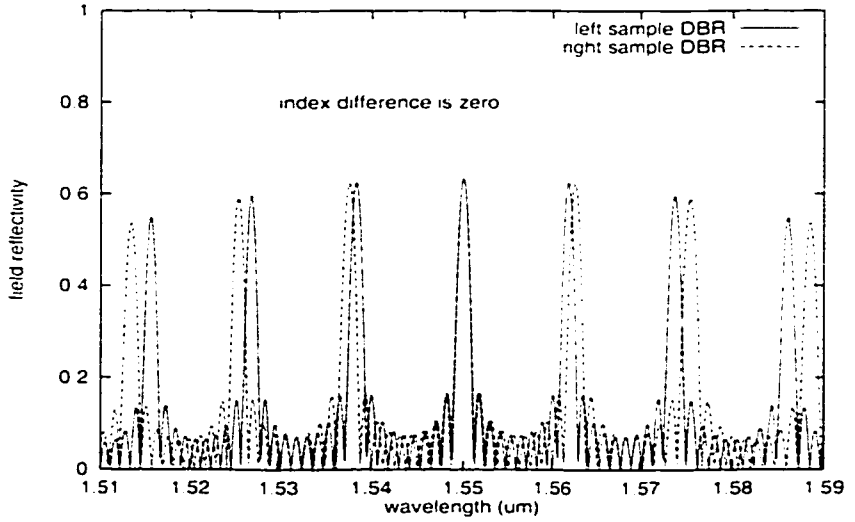

Figure 5. 10 Reflectivity peaks matching of two sampled grating reflector while tuning current equal to zero.

With the design scheme discussed above, we will present some detail numerical simulation results on this kind of DBR sampled grating laser diodes using the model developed in the previous chapters. In the simulation, the complicated passive sections are simulated by digital filters based on the reflectivity profiles, which are calculated analytically by eqn (5.14). Then with the split step approach, the performance of this kind laser diode can be simulated efficiently. The laser structure to be discussed is shown in Figure (5.8). For the left side sampled grating structure, we choose $\Lambda = 32um$ with $L_1 = 3.6um, kL_1 = 0.075$, and there are 10 sampled grating in this section. For the right side sampled grating structure, we use the same parameters as the left side except $\Lambda = 30um$. Bragg wavelength of both sides is set equal to 1.55μm while no carrier injection or electric field is applied with $n_{eff0} = 3.2$.

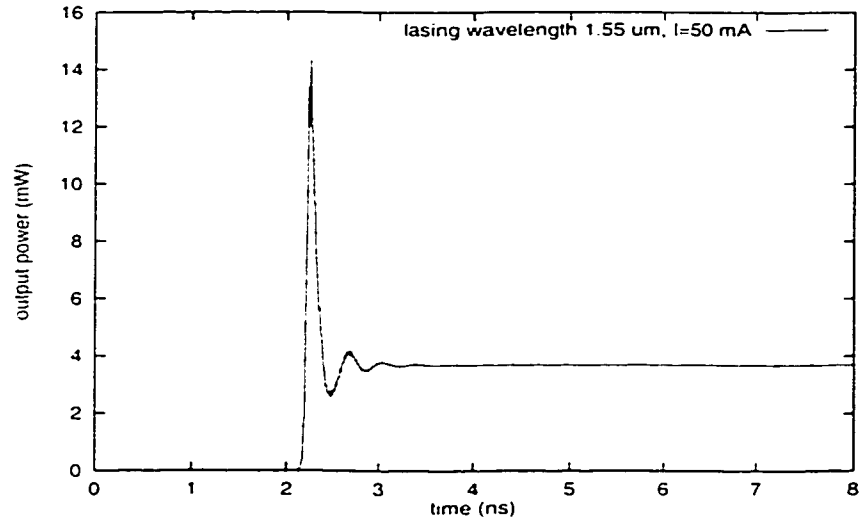

Figure 5. 11 The transient state of sampled grating DBR laser

The reflectivity profiles in this case are shown in Figure (5.10). The lining up wavelength is located at 1.55μm for the two sampled grating structure, and hence the mode near this wavelength will be lasing. Figure (5.11) shows the transient state at this wavelength with the active section biased at 50mA. If we fixed the left-hand side reflectivity profile, then change the refractive index of the right hand side by carrier injection or applied electric field. The lasing modes will be tuned discretely in several wavelengths. Figure (5.12) demonstrates the output spectra of the seven discrete wavelength channels in the same graph.

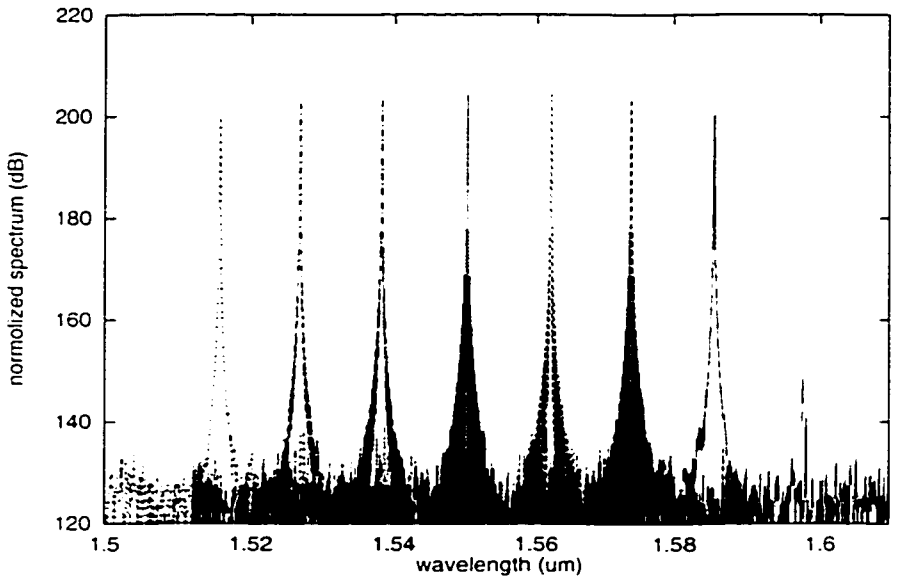

Figure 5. 12 Output spectra of the seven wavelength channels. The total tuning range is around 72nm.

As shown in Figures (5.12) and (5.13), if the effective refractive index changes from – 0.004 to +0.004, i.e., a relative change of 0.2%, it will lead to a wavelength change range from 1515.6nm to 1585.3nm, i.e., a 70nm wavelength spanning with almost equal spacing channels at the interval of 10nm. This is a great improvement on the tuning range compared with the traditional DBR type laser. It should be noted that our simulation results are qualitatively comparable with the experimental measurements and analytical prediction.[6, 3, 10].

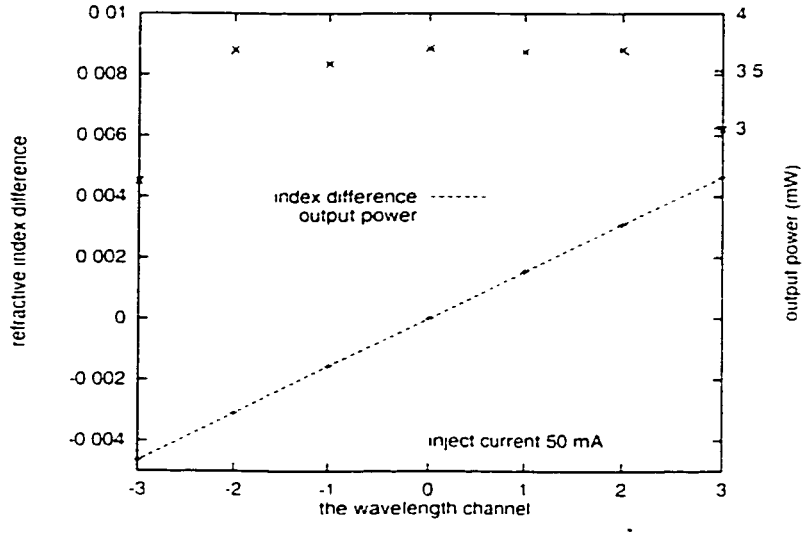

Figure 5. 13 Output power and refractive index difference while tuning the wavelength.

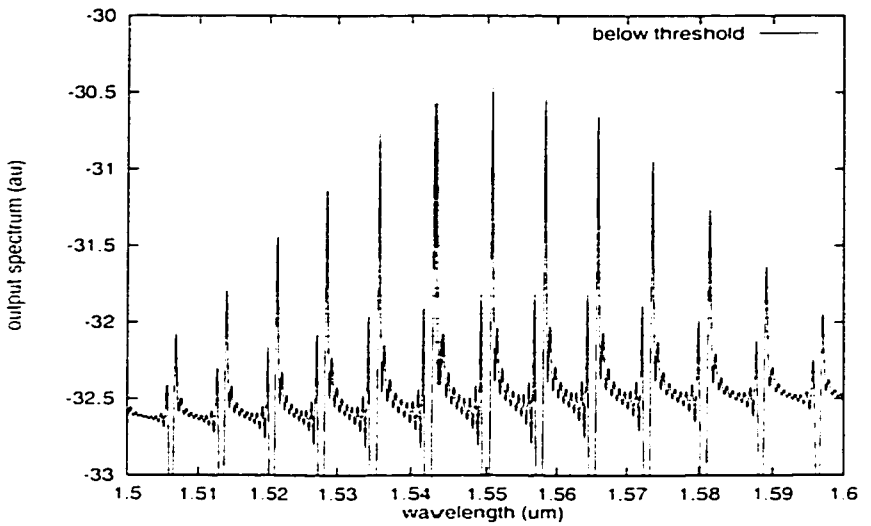

Figure 5. 14 Below threshold spectrum of sampled grating gain coupled DFB laser with both facets AR coated

5.4 DFB Type Tunable Laser

As we show in the previous section, the sampled grating can provide a multi-peak comb like reflectivity profile. Therefore if the structure is applied in the active section as a sampled grating DFB laser, naturally we should expect a multi-modes laser diode. We have demonstrated that a uniform grating DFB laser will present two degenerated modes at the edge of the stop band. Therefore, for a sampled grating DFB structure, we should have a multi-peak output spectrum, and each peak should consist of two degenerated modes. To make one peak corresponding to only one mode, we suggest that a gain coupling should be introduced. To show the above argument clearly, in Figure (5.14), we show a typical below threshold spectrum for a sampled grating DFB laser diode with 10% gain coupling, which is calculated by the transfer matrix method [9]. We can see that it is a potentially multi-mode laser diode with equal wavelength

spacing $\Delta\lambda = \lambda^2/(2n_{eff}\Lambda)$. Therefore if we can find a filter mirror, whose pass-band is less than the mode interval and also is tunable in a wide wavelength range, a wavelength tunable laser with large SMSR will be obtained. Co-directional filter is a good choice to meet this large tuning range requirement [5.8]. In the following section, we will present a brief discussion on the co-directional filter first. Then some numerical simulation results on this sampled grating DFB laser cascaded with a co-directional filter will be presented. To our best knowledge, it is the first rigorous numerical simulation on this type of laser diodes [10].

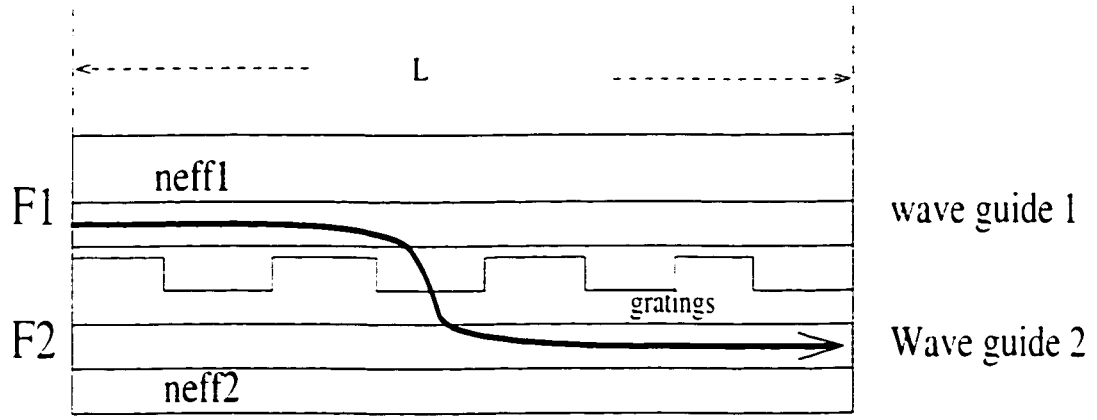

Figure 5. 15 Grating assisted Co-directional coupler filter

5.4.1 Co-directional Filter

The co-directional filter to be discussed is shown schematically in Figure (5.15). If electric field in eqn.(5.1) is expressed as

$$E = F_1(z)\Phi_1(x,y)\exp(-j\beta_1 z) + F_2(z)\Phi_2(x,y)\exp(-j\beta_2 z) \qquad (5.15)$$

and we also assume

$$[\nabla^2 + \omega^2\mu\varepsilon^0]\Phi_i(x,y)\exp(-j\beta_i z) = 0 \quad i = 1,2 \qquad (5.16)$$

Substituting eqns.(5.15) and (5.16) into eqns (5.1), we have

$$\frac{d}{dz}\begin{bmatrix} F_1(z) \\ F_2(z) \end{bmatrix} = \begin{bmatrix} 0 & -jk\exp(j\Delta\beta z) \\ -jk^*\exp(j\Delta\beta z) & 0 \end{bmatrix}\begin{bmatrix} F_1(z) \\ F_2(z) \end{bmatrix} \qquad (5.17)$$

where $\Delta\beta$ is detuning factor and k is the coupling coefficient defined by

$$\begin{aligned} \Delta\beta &= \beta_1 - \beta_2 - 2\pi/\Lambda \\ k &= \frac{k_0^2}{2\sqrt{\beta_1\beta_2}}\int d_1\Phi_1\Phi_2^* dxdy \end{aligned} \qquad (5.18)$$

here we only consider the first order effects, and the definition of d_1 is shown in eqn. (5.6). Solving the coupled mode equation (5.17), finally we obtain

$$\begin{bmatrix} F_1(L) \\ F_2(L) \end{bmatrix} = \begin{bmatrix} T_{11} & T_{12} \\ T_{21} & T_{22} \end{bmatrix} \begin{bmatrix} F_1(0) \\ F_2(0) \end{bmatrix} \tag{5.19}$$

where

$$\begin{aligned} T_{11} &= \left[\cos(sL) - j\frac{(\Delta\beta/2)}{s}\sin(sL)\right]\exp(j\Delta\beta L/2) \\ T_{12} &= -j\frac{k}{s}\sin(sL)\exp(-j\Delta\beta L/2) \\ T_{21} &= -j\frac{k^*}{s}\sin(sL)\exp(j\Delta\beta L/2) \\ T_{21} &= \left[\cos(sL) + j\frac{(\Delta\beta/2)}{s}\sin(sL)\right]\exp(-j\Delta\beta L/2) \end{aligned} \tag{5.20}$$

and s in eqn(5.20) is the eigenvalue equal to $s = \sqrt{(\Delta\beta/2)^2 + k^2}$.

We define a parameter called power exchange coefficient [4], which is equal to the ratio of transmission power of path 2 at z=L to that of path 1 at z=0. From eqn. (5.19), it is easy to show that the power exchange coefficient can be expressed as

$$\gamma = \frac{1}{1 + (\Delta\beta/2k)^2}\sin^2(kL\sqrt{1 + (\Delta\beta/2k)^2}) \tag{5.21}$$

From eqn. (5.21), we find that if $L = \pi/(2k)$, i.e., one coupler length, at the filter central wavelength $\lambda_0 = \Lambda(n_{eff1} - n_{eff2})$, a complete power exchange may occur. We can also demonstrate that the band-width of filter satisfies the relation [4]

$$\Delta w \propto \frac{k\lambda_0^2}{(n_{g1} - n_{g2})} \tag{5.22}$$

and the tuning wavelength range satisfies the relation [4]

$$\Delta\lambda \propto \frac{\Delta n_{eff}}{(n_{g1} - n_{g2})} \tag{5.23}$$

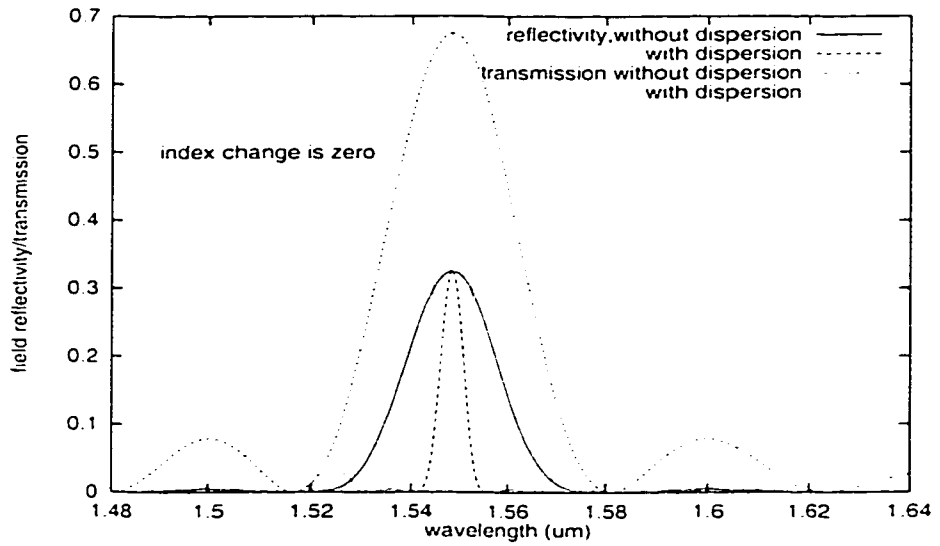

Figure 5. 16 Reflectivity and transmission of the co-directional filter. Refractive index dispersion plays an important role in the bandwidth.

Eqns (5.22) and (5.23) show that tuning range and filter band width both are proportional to the reverse of $n_{g1} - n_{g2}$, which is the group index difference coming from the material dispersion. Normally, it can be 2-3 times larger than the effective index difference [4.8]. From eqns (5.22) and (5.23), it is argued that in order to extend the tuning range of the filter, small refractive index difference between the two waveguides is required. On the other hand, to maintain small band-width of the filter, the refractive index difference should be large enough. Therefore these two requirements must be compromised in the filter design. Finally, to make the filter central wavelength locate at the desired wavelength, an appropriate grating period has to be applied. Figure (5.16) shows the typical reflectivity and transmission of a co-directional filter while the length L equal to one filter length, where cleaved facet condition is used at the end z=L. We can see that material dispersion leads to great shrinkage of filter band-width.

5.4.2 Simulation Results

With the sampled grating DFB in the active section, which provides multi-mode operation, we cascade a co-directional filter with cleaved facet at one end of the laser diode as a wavelength selection and tuning element. The tunable laser structure to be simulated is shown schematically in Figure (5.17). For the active section, we choose $\Lambda = 50\mu m$, with $kL_c = 0.15$, 10% gain coupling and duty cycle $x = L_c / \Lambda$. The total cavity length is equal to 500μm. The Bragg wavelength is 1.55μm while there is no current injection. For the co-directional filter, grating period $\Lambda = 12\mu m$, the central wavelength of the filter also equal to 1.55μm while there is no tuning current or electric field. The total length of the filter is equal to 1000μm, which is one coupling length. In this structure, the adjacent mode spacing of the active sampled grating DFB

is around 7.4nm, while the FWHM of the co-directional filter is less than the half the mode spacing. Therefore, by tuning the refractive index in wave-guide 1 of the co-directional filter, we can obtain a discrete tunable laser diode.

Using the split step approach introduced in the previous chapters, we have simulated the tunable laser diode based on a combination of the sampled grating DFB and a co-directional coupled filter. In the simulation of a co-directional filter, the material dispersion and different group velocity between the two wave-guides present great challenge to the full traveling wave approach [7]. However, in our split step approach, this simulation difficulty can be avoided easily.

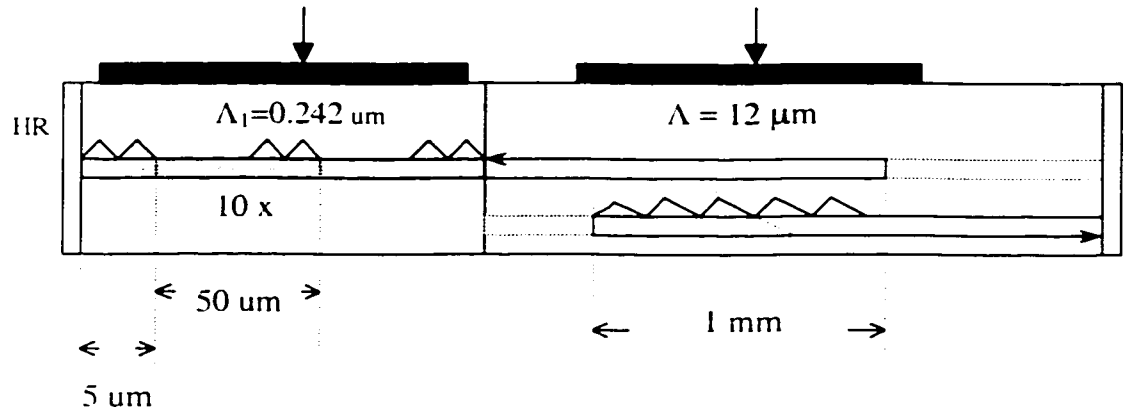

Figure 5. 17 Sampled grating DFB laser cascaded with a co-directional filter.

Figure (5.18) shows the transient state while tuning current equal to zero. While we change the refractive index in wave-guide 1 of the co-directional filter, the lasering wavelength will be tuned discretely to display several channels. In Figure (5.19), we show the output spectra of these lasering channels in the same graph. As shown in

Figures (5.19) and (5.20), this sampled grating DFB wavelength tunable laser can provide more than 70 nm tuning range with 10 discrete lasering channel by a refractive index change in the range less than 0.2%. Unfortunately, there are no experimental results for this kind of device up to now. But to our best knowledge, this simulation is the first numerical calculation results based on a theoretical laser model.

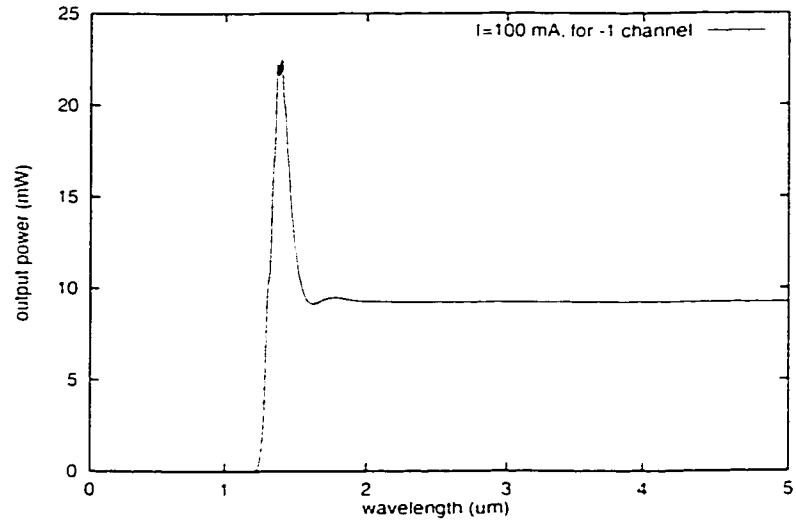

Figure 5. 18 Transient state when the injected current of active section equal to 100mA while the tuning current of co-directional filter is zero.

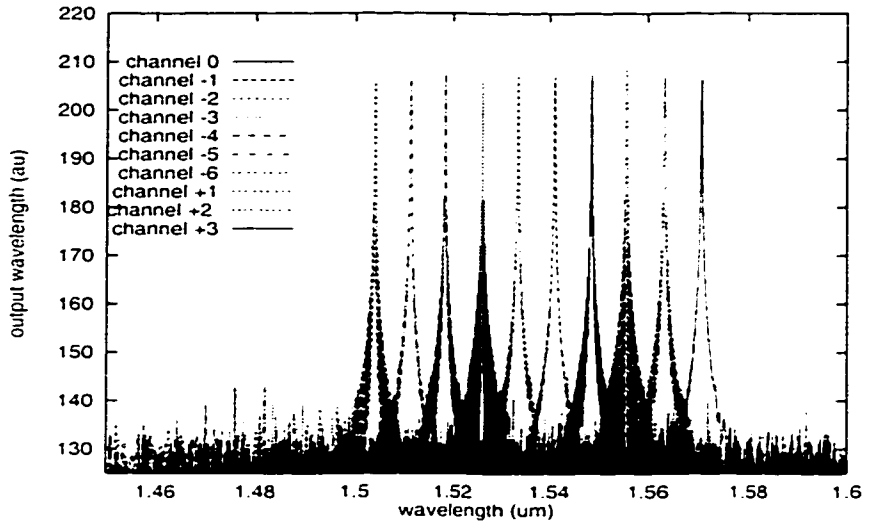

Figure 5. 19 Turning range and output spectrum of sampled grating gain coupled DFB laser with co-directional filter.

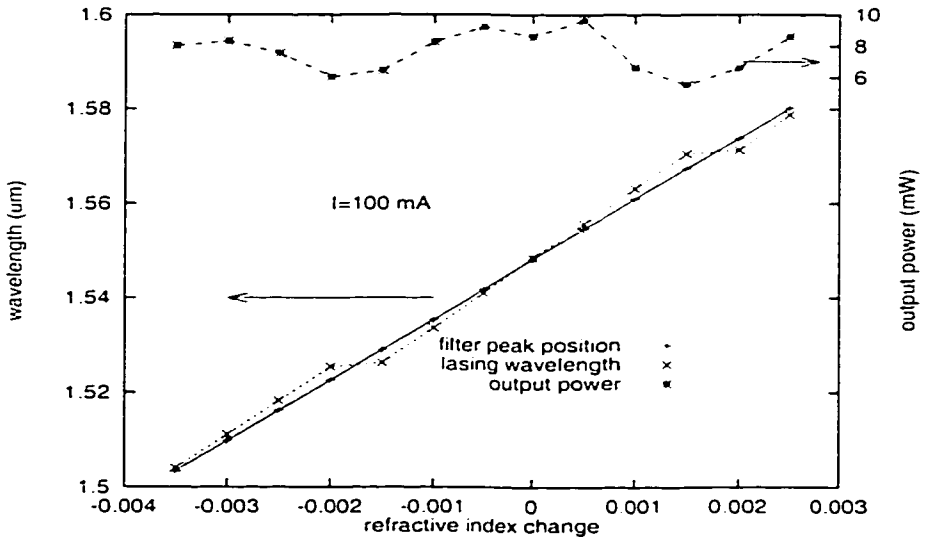

Figure 5. 20 Operating condition while the laser is tuned.

5.5 Summary

In this chapter, using the split step/digital filter approach, we present a detail investigation on broadly wavelength tunable laser diode with the sampled grating structure. Following the design procedure suggested in [3], firstly, we show the numerical simulation results on the DBR type/vernier ruler tunable laser. Our simulation results qualitatively agree well with the experimental measurement. Secondly, using the guideline, which is proposed for the wavelength tunable laser cascaded with co-directional filter [4], we investigated a combined structure consisted of sampled grating DFB and co-directional filter. Although, there are some analytical analyses on this type device [4], we present the first comprehensive simulation based on a rigorous numerical model. It is concluded that the sampled-grating structure can be applied not only as a DBR reflector but also as a DFB component to extend the wavelength tuning range dramatically. The laser model, which we proposed, again is very successful in simulating these kinds of complicated devices.

Chapter 6

Multi-Wavelength Gain-Coupled DFB Laser Cascade

6.1 Introduction

As we discussed in the previous chapter, recent phenomenal progress in development and deployment of WDM technologies for broadband communication systems has called for need of multiple wavelength light sources. Wavelength-tunable laser diodes can offer new system functions such as switching, routing and service segmentation, in addition to the capacity upgrades [1]. Multi-wavelength gain coupled DFB cascade is the most recent design scheme to meet this challenge, which origins naturally from laser array.

Aside from the discrete laser diodes with pre-set wavelengths, an array of laser diodes with different wavelengths placed in parallel appears to be a more compact and

perhaps economical solution. Recently, a new scheme was proposed by Hong and co-workers in which a multi-wavelength laser is realized by placing a number of DFB laser diodes with different wavelengths in series (referred to as laser cascade) [2]. By combination of the multi-wavelength laser array and cascade, a laser matrix has been demonstrated with expanded range of accessible wavelength and similar performance specifications to a typical DFB laser diode.

Different from the laser array in which the different DFB laser diodes are operated independently, stronger interaction among the different laser sections in cascade is expected in the new multi-wavelength lasers. For instance, the lasing optical fields share the same optical cavity. Even when only one of the sections is operated above threshold, the lasing light will still pass through the other sections, which may also have effects on the overall lasing characteristics. To ensure stable operation of the laser in the entire accessible wavelength range, we need to develop proper design guidelines for the grating structure of each section to minimize the interaction. Further, it is important to understand the static and dynamic characteristics of such laser in a wide range of operation conditions in order to identify the regime for stable operation and perhaps to explore new applications.

As shown in chapters 4 and 5, we have developed and demonstrated a comprehensive design model for the DFB laser. Since the traveling-wave model solves the time-dependent coupled-wave equations for the forward the backward traveling waves directly in time domain, it can be readily applied to laser diodes with complex longitudinal structures and/or operated with strong interaction between different sub-cavities. Therefore, it is an ideal simulation tool for the multi-wavelength gain-coupled DFB cascade.

We write this chapter with the following objectives: firstly, based on this comprehensive model, we carried out a systematic simulation for the static and dynamic characteristics of the multi-wavelength DFB laser cascade. In particular, we investigated the design guideline and criteria for the stable CW operation of the laser.

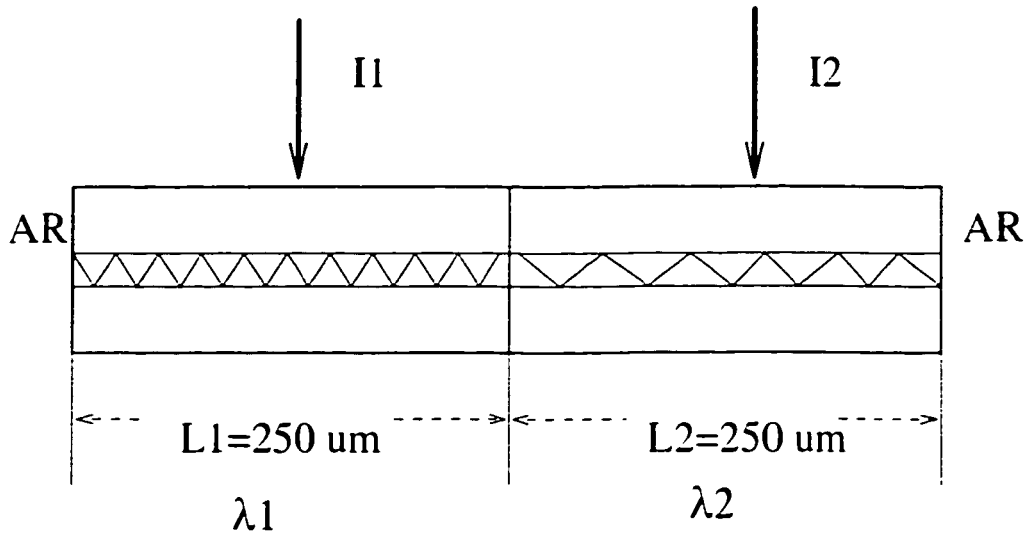

Figure 6. 1 Longitudinal structure of the two-section cascaded DFB laser.

Also, we have revealed and studied possibility for short pulse generation from this laser, primarily due to mode beating of two or more lasing sections. To focus on the interaction between the DFB section, this design guideline is based on a relatively simple two-section structure. Secondly, as a natural extension, we will investigate the case of three-section DFB cascade, which is the structure suggested by Hong and co-workers. Finally, a brief summary will be given.

6.2 Design for the DFB Laser Cascade

The design model used for the multi-wavelength DFB laser cascade is shown schematically in Figure (6.1). For the sake of simplicity, we consider only a structure with two active grating sections placed in series along the laser cavity. The analysis may be readily extended to multi-section structures and the underlying physics and the characteristics of the devices are expected to be the same as the two-section structure.

For each of the active grating sections, distinct Bragg wavelengths are designed and fixed in fabrication by setting different grating period. Other design parameters for the different longitudinal sections are the complex coupling coefficients and the cavity lengths, which are critical for the operation of the device. Finally, the facet reflectivities can be controlled by appropriate coating technology, if necessary.

6.2.1 Key Parameters for Design Consideration

Bragg Wavelength:

The first design consideration is the proper choice of the grating period for each of the lasing section. The Bragg wavelength λ_B is related to the grating period Λ by [5]

$$\lambda_B = 2 n_{eff} \Lambda \qquad (6.1)$$

The separation between the Bragg wavelengths of different lasing sections should be determined by the maximum tuning range achievable by means of temperature change (i.e., the change of temperature of the heat sink and/or that of the active region due to current injection). In our design model, we assume that $\Delta\lambda_B = 6\,\text{nm}$ and choose that grating period such that the Bragg wavelengths for the two sections are $\lambda_{B1} = 1550\,\text{nm}$ and $\lambda_{B2} = 1556\,\text{nm}$, respectively.

Complex Coupling Coefficient

The second design parameter is the complex coupling coefficient. First of all, we need to choose a proper value for the product of the magnitude of the coupling coefficient and the length of the active grating region, i.e., $|\kappa|L$ for each section. When sufficiently large, $|\kappa|L$ is approximately proportional to the width of the stop-band by the following approximate formula:[6]

$$\Delta\lambda \cong \frac{2\lambda_B \Lambda}{\pi}|\kappa| \qquad (6.2)$$

.To minimize the optical interaction among the different lasing sections, we should design $|\kappa|L$ so that there will be no substantial overlap between the stop-bands of the different sections. Figures (6.2a) and (6.2b) show the stop-bands of the two sections with different $|\kappa|L=3$ and $|\kappa|L=5$, respectively. It appears that, for the choice of the separation of the Bragg wavelengths as proposed above, the optimal $|\kappa|L$ should be around 3 ~ 4 to avoid overlap between the stop-bands between the two sections.

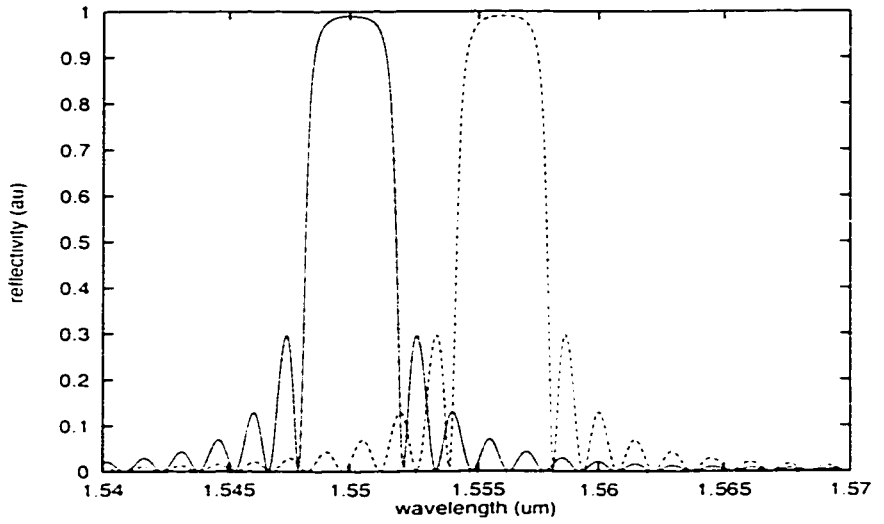

(a)

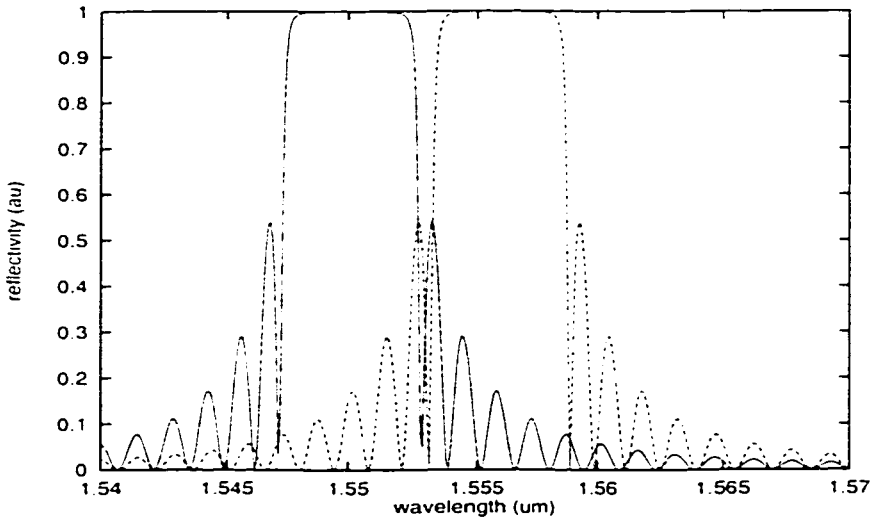

(b)

Figure 6. 2 Stop-band position of the two-section DFB laser. (a) for KL=3.(b) for KL=5.

Another important issue for the stable multi-wavelength operation is the mode stability. For conventional index-coupled DFB lasers, the lasing action may occur on either left or right side of the Bragg wavelength, affected significantly by the phase of the light coming back into the lasing section. To overcome this problem, as we show in the previous chapters, strong gain coupling is introduced to ensure that the lasing will occur on the right side of the Bragg wavelength. In our design model, we assume that the gain coupling is about 10%.

Facet Reflectivities:

Lastly, we need to consider the reflectivities at the two facets of the multi-wavelength laser. For the sake of simplicity, we assume that both facets are anti-reflection coated with zero reflectivities. Therefore, there is no FP mode disturbance.

6.2.2 Conditions for Stable CW Operation

One of the central concerns for the operation of the multi-section DFB laser diode is the condition for stable single-mode CW operation. In practice, we normally bias one of the two sections above threshold, while keep the other section below threshold. Figure 3 shows the output power from the left-facet of the laser diode as a function of the bias current in the left section. The non-lasing right section is assumed to be lossless for the sake of simplicity. Both cases for $|\kappa|L=3$ and $|\kappa|L=5$ are simulated. It is interesting to note that the output power and the slope efficiency from the left facet are higher for the case of $|\kappa|L=5$ than those for $|\kappa|L=3$. In the laser cascade we have examined, there are in fact two optical feedback mechanisms, namely, the distributed-feedback (DFB) effect in the lasing section and the distributed Bragg reflection (DBR) effect in the non-lasing section. As $|\kappa|L$ increases, the output power and the slope

efficiency from the left facet will be reduced by the DFB effect in the lasing section and enhanced by the DBR effect in the non-lasing section. In our current design when $|\kappa| L = 5$, there appears to be substantial feedback from the nonlasing DBR section and hence lead to a net increase in the output power and the slope efficiency from the left facet. On the other hand, the side mode suppression ratio in the case of larger $|\kappa| L$ is smaller due to the inferior mode selectivity of the DFR section, as evident from Figure 6.4.

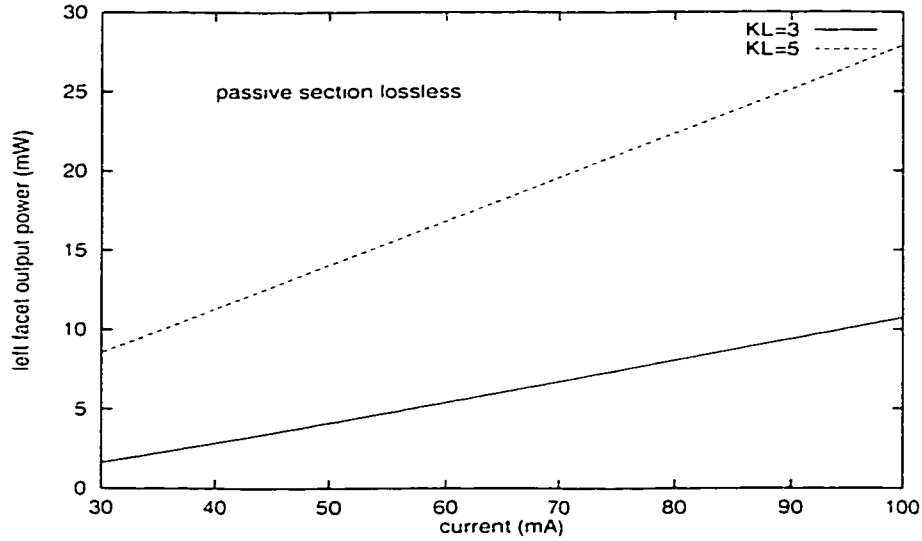

Figure 6. 3 L-I curves while thermal wavelength chirp is not considered for KL=3, and 5 respectivety.

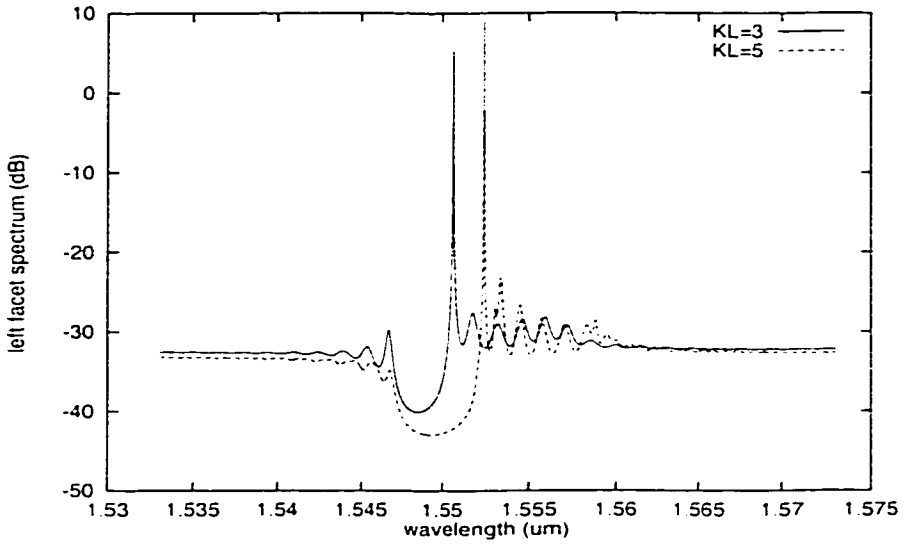

Figure 6. 4 Comparison of typical spectrum between KL=3 and KL=5.

A major assumption in the above design model is that the wavelength shift due to thermal effect in the lasing section is negligible. In practice, however, this is not the case. As the injection current increases, the temperature in the active region of the lasing section rises and causes a wavelength shift towards longer wavelength. Consequently, the stop-band of the lasing section will shift towards the stop-band of the nonlasing section and result in more overlap between the two stop bands. By taking into the thermal wavelength chirp into consideration by simply introducing a temperature (or current)-dependent effective index

$$n_{eff}(I) = n_{eff}(0)[1 + \alpha(I - I_{th})] \qquad (6.3)$$

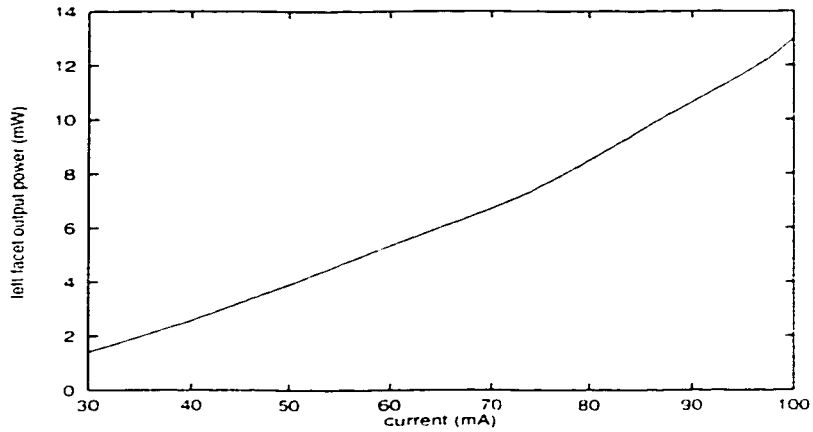

(a)

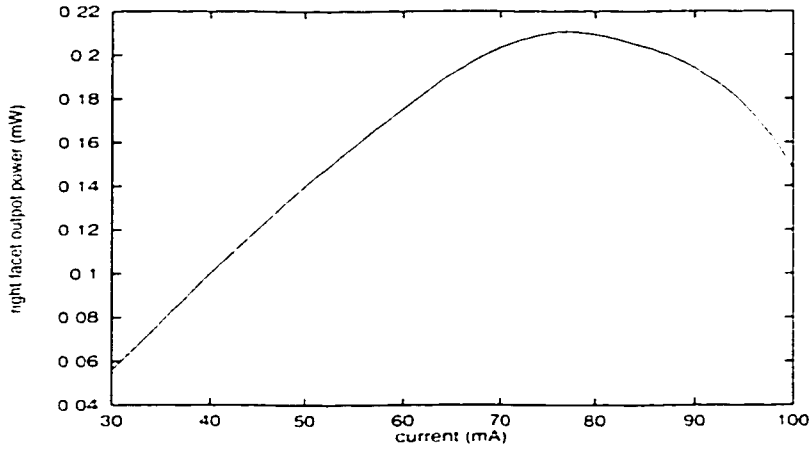

(b)

Figure 6. 5 L-I curves while thermal wavelength chirp is considered. Here KL=3, and passive section with large loss, (a) for left facet, (b) for right facet.

where the coefficient α is chosen to be 2.679×10^{-5} /mA. Figures (6.5a) and (6.5b) show the output powers from the left and the right facets of the laser cascade for the case of $|\kappa| L = 3$. To minimize the non-lasing section feedback, we have assumed a large optical loss in the passive section. It is still observed that due to the enhancement of the DBR section as the injection current increases the slope efficiency of the left power increases, whereas that of the right power drops. The impact of the interaction between the two sections due to the thermal wavelength shift is also illustrated in Figure 6 in which the spectra of the output light from the left facet at different bias currents. For the sake of comparison, the stop band of the nonlasing right section is also shown in the same figure. It is noted that when the lasing wavelength comes to overlap with the stop band of the nonlasing section, kinks in the output powers occur as evident from Figures (6.5a) and (6.5b).

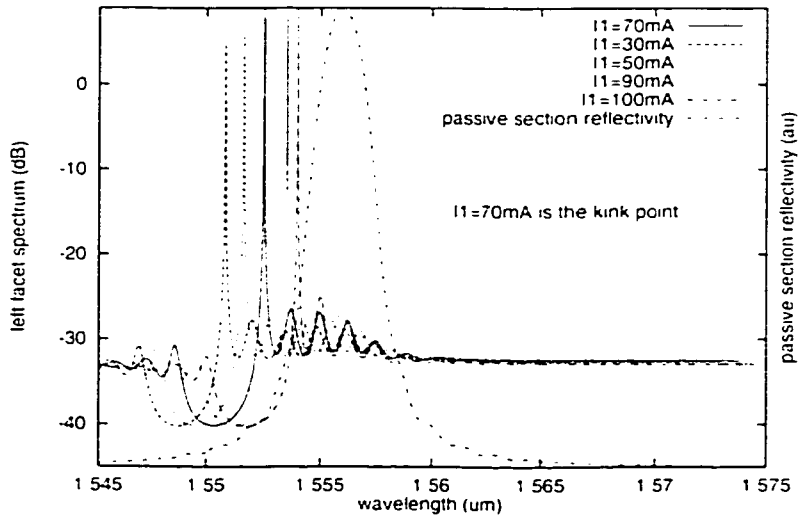

Figure 6. 6 Wavelength chirp and reflectivity spectrum. The laser setup is the same as Fig.5.

6.2.3. Mode Beating and Pulse Generation

In the previous section, we have shown that each section of multi-section DFB laser can be working independently as an individual DFB laser in combination with a passive DBR section. Stable CW operation at distinct wavelength can be achieved by biasing one of the sections while keeping the other section(s) below threshold with proper design of the Bragg wavelengths and the $|\kappa|L$s. On the other hand, when both sections are biased above threshold, the laser may work in a different regime in which short pulse can be generated due to the beating of the two lasing modes. To see this, we fixed the bias of the left section at I_1=100mA and increase the bias on the right section from I_2= 0 to 100mA. [Figure (6.7) and (6.8)]. We also noticed that if the bias current were too high in non-working section, the output power would show great fluctuation in the time domain. Since the Bragg wavelength interval between two adjacent sections is only 6 nm, to catch the mode beating, a fine time scale must be used. In the previous simulation, the time interval between two adjacent points is around 0.012 ns. This large time scale will smear the beating pattern. Therefore in the following simulation, we adjust the time scale to approximately 0.062ps. If the first two sections are both biased at 100 mA , after 8ns, we use the fine time scale to record the output power vs time. Figures 6.8 and 6.9 show the output power and spectrum respectively. It can be seen clearly that there is a beating period around 0.0015 ns. From the spectrum, we can see that two DFB modes are both excited with the mode spacing around 6 nm. It should be noted that the beating period, which is equal to 0.0015ns, is in good agreement with the mode interval 6nm around wavelength at 1550 nm [3.4].

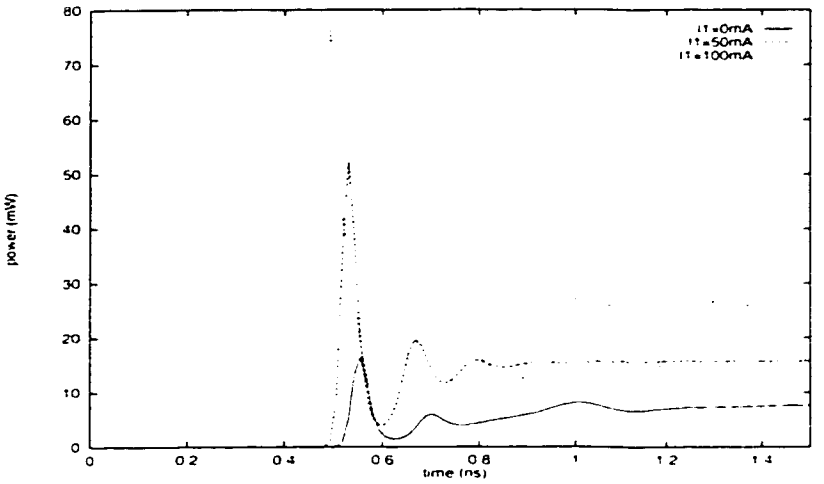

Figure 6. 7 Output power vs time as left section biased at 100mA, while the right section bias changes from 0-100mA.

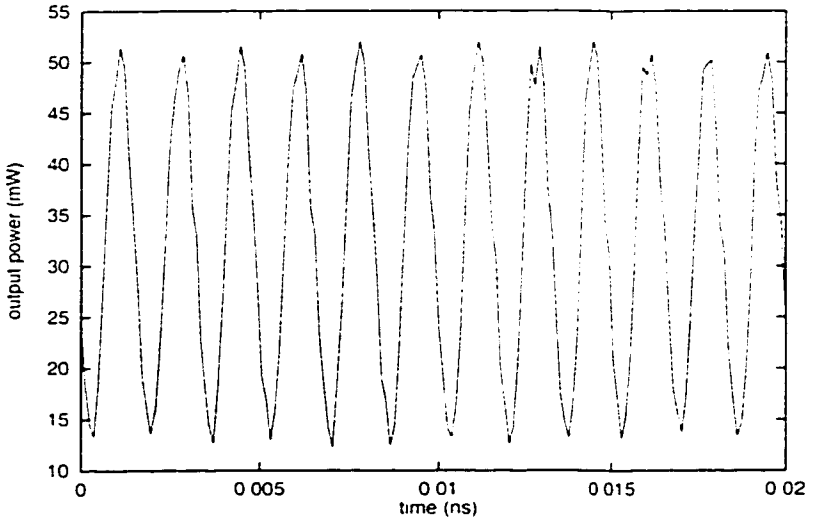

Figure 6. 8 Mode beating in multi-section DFB semiconductor laser while the first two sections are both deeply biased.

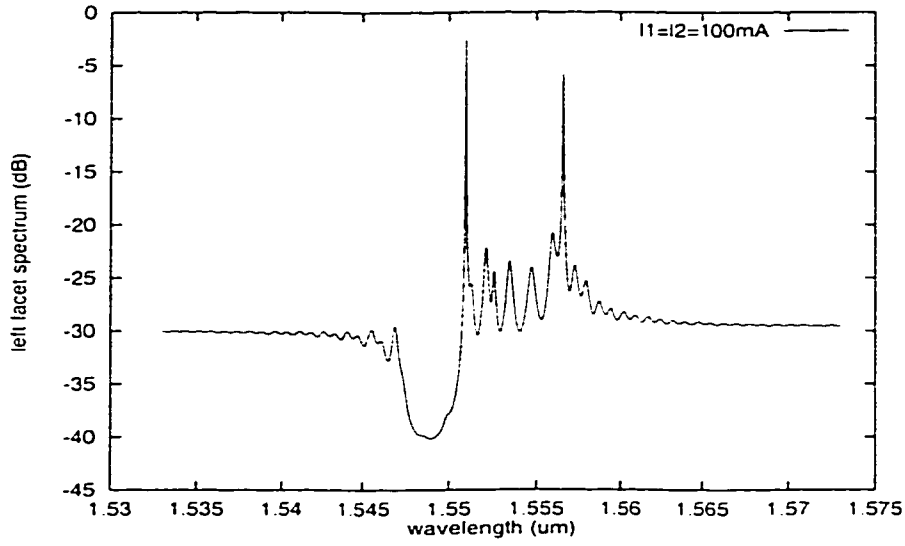

Figure 6. 9 Output spectrum of the two-section DFB semiconductor laser, while the two sections are both deeply biased.

6.3 Three-section DFB Cascade

The three-section gain coupled DFB cascade as suggested by Hong and coworkers is shown schematically in Figure (6.10). The output light is coming out of the laser cavity from left facet. To make the laser diode operate symmetrically for each section, a forth absorption section is added at the right end of the cavity. It is a uniform waveguide with a large optical loss controlled by the injected current. Using the optimal design parameters suggested in the previous part, we choose KL=3 with 10% gain coupling. The Bragg wavelength interval is 6nm between the adjacent sections. While one section is working, its left section or sections will be biased at the threshold or with a little optical loss, but its right section or sections will be biased far below the

threshold with large optical loss. Therefore, the interaction between the adjacent sections is minimized.

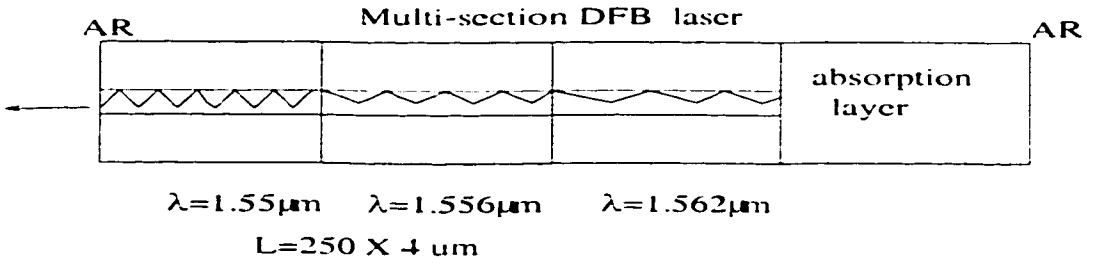

Figure 6. 10 Longitudinal structure of three-section gain-coupled DFB laser cascade.

The CW working condition is exactly as shown in the previous part analysis. We show the output spectra of the three sections in the same graph in Figure (6.11) with the fixed temperature. It can be seen clearly there are three lasing channels with the interval around 6nm. As presented in the previous part, each channel could be tuned by thermal effect individually. It is suggested that to avoid the kink of L-I curve, tuning current should be within certain range. Otherwise, we may change the sink temperature directly to tune the lasing wavelength.

As we show in the design part, this three-section DFB cascade can also generate short light pulse due to the mode beating and competition. Figure (6.12) show the pulse generated by biasing the first two sections deeply while keep the other section with large loss [3,4].

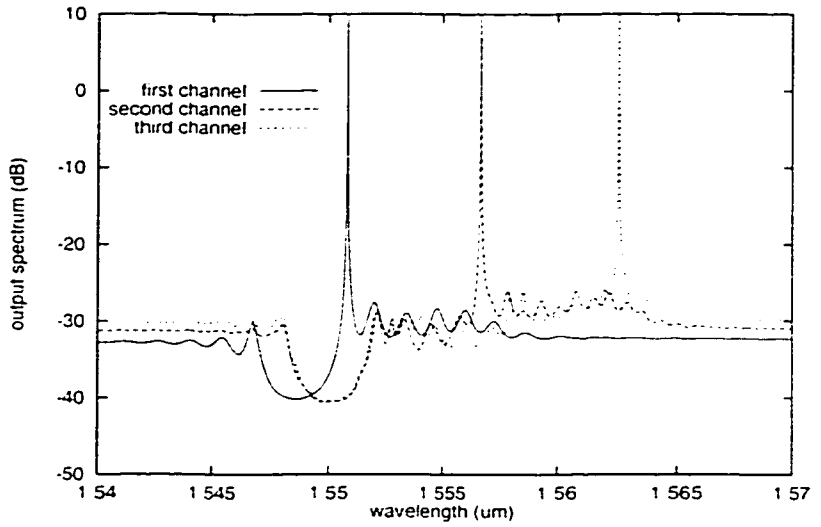

Figure 6. 11 The lasing channels of three-section gain-coupled DFB cascade at a fixed temperature.

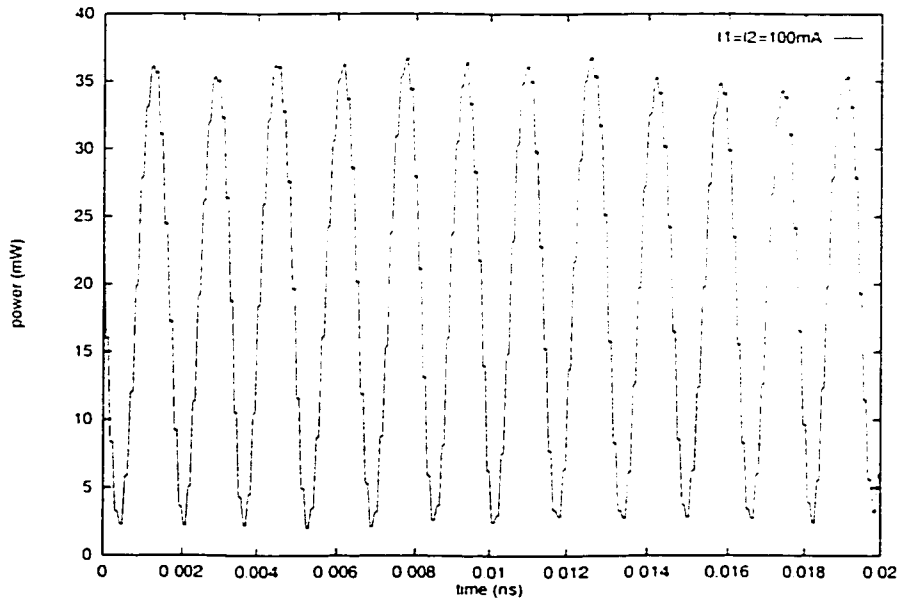

Figure 6. 12 Mode beating while the first two sections deeply biased.

6.4 Summary

In conclusion, we have demonstrated a multi-section gain-coupled DFB laser cascade. Which provides a wide tuning range with programmable tuning mechanism. With the cooperation with Nortel researchers, our theoretical modeling and simulation for the first time is applied directly as a design and optimization tool in the industry and have received very good feedback [3.4]. It is shown that multi-section gain-coupled DFB laser cascade can be used not only as a CW wavelength tunable laser, but also as a short pulse generator.

Chapter 7

Conclusions and Future Research

7.1 Summary of the Achievements

The contributions of our research consist of two parts. The first part is on the development of physical models and simulation techniques. In this part, there are two hierarchical levels of models. The first level is about the material characteristic simulation, which is the basis of the second level models and is also an independent module itself; the second level is the device modeling, or traveling wave model for complex integrated laser diode. With the simulation tools developed, the second part is on the original applications to wavelength tunable lasers, which include sampled grating lasers and multi-section DFB gain coupled cascades.

7.1.1 Simulation Tool Developments

Semiconductor Material Models

Firstly, we have presented an inter-band transition model to simulation the intrinsic refractive index of semiconductor material for InP based material series, which are commonly used in laser diode fabrication for optical communication system. The models may also be extended to the other material systems by minor modifications. Secondly, we generalize the existing models to simulate the refractive index change caused by carrier injection, applied electric field and thermal effects. Inter-band transition model is still the core part in this simulation. For non-radiative process, the index change is mainly due to band filling, band gap shrinkage, plasma effect and band tilting. The physical mechanisms of these effects are explained. Every effect is simulated by a prototype function with some fitting parameters. Finally, We developed a quantum well gain and its refractive index change model based on the QW band structures calculated by k-p theory. The strain effect caused by mismatch of lattice constants between the well and barrier regions is considered naturally in the Hamiltonian. Some key features unique to QW materials, such as negative effective mass of valence bands, band profile shift due to compressive or tensile strain, are demonstrated. This model has been used in NORTEL as QW fabrication design and simulation tool and received good feedback.

In the material modeling and simulations, we have tried to develop models by the following idea. (i). The models are completed to include all known physical observable phenomena. Therefore, using the theoretical models, if we changed some physical inputs, such as quantum well width, carrier injection density, we could predict optical properties changing trend, i.e., an engineer could use the models qualitatively to design a fabrication process for the required optical properties. (ii) The models leave some fitting parameters to calibrate the simulation results with experimental measurements. This approach follows the philosophy, which we presented in the previous chapters, i.e., we do not believe that there is a general physics based model, which can predict such accurate material simulation results as

required at any operating condition. The first part has already accomplished in our thesis, however the second part still needs some works in co-operation with the industry, which will be discussed in the following section.

Laser Diode Models

We have derived the governing optic field equations for the traveling wave model and the standing wave model from the same 1D effective equation. The difference and application limitation of the two approaches are identified. We also incorporate the thermal effects into traveling wave model for the first time. Since the time constant of the thermal effect is much longer than that of the optical effects, we introduce an iteration method to overcome this simulation difficulty. As an original application of our models, we present a theoretical explanation on the various thermal time constants during the large signal modulation of a DFB laser diode, which is observed experimentally. In the explanation, a thermally quasi-static state concept is introduced. Therefore the various time constants could be simulated and explained by a general physics model, instead by fitting a series of parameters to the experimental measurements.

Another important and original achievement is that, we combine the traveling wave model with the standing wave model by introducing a time domain digital filter into laser diode modeling. As we presented in Chapter 4, since traveling wave model has to trace the waveform both in time and space domain by the numerical convergence up-limit $\Delta z = v_g \Delta t$, it would be quite time consuming to simulate the laser performance when passive section is extremely long. Standing wave might also have great numerical difficulty in searching the complex roots corresponding to the laser modes for such a complicated structure. Therefore, on one hand, we keep the traveling wave

concepts in the active section modeling; on the other hand, we introduce a digital filter to simulate the long complex passive section, whose response function in frequency domain is obtained from the reflectivity and transmission spectra of the passive section. This transformation between the frequency domain and time domain made the model versatile in various laser diode simulations. Up to our best knowledge, it is the most advanced approach in the traveling wave model for laser diode simulation.

In summary, we have completed a general traveling wave model, which take into account of the spatial hole burning, spontaneous random noise, material effect, thermal effects, and electric effects. The models can be used to simulate various laser structures, such as FP laser, DFB/(gain coupled, phase shifted) laser, DBR laser and other complex multi-section lasers.

7.1.2 Application on Wavelength Tunable Laser

Sample Grating Assisted Tunable Laser Diode

We have investigated two kinds of laser diodes in this category. One is DBR type Venier ruler like structure. The other is DFB multi-mode laser cascaded with a co-directional filter. These lasers have been discussed qualitatively in the literatures. Our digital filter approach shows great advantage in this kind of complex laser structure simulation/design and hence to our best knowledge, is the first attempt to simulate this kind of lasers based on a rigorous physics model.

Multi-section Gain Coupled DFB Cascade

This complex structure is the most recent design on wide range wavelength tunable laser diode for optical communication system. We have investigated the interaction

between the adjacent sections, optimized the key design parameters for satisfactory laser performance. Especially, the L-I curve kink observed experimentally is explained based on the simulation results. We also point out that there exists a short pulse generation working condition due to multi-mode nature of this DFB cascade. Because of complex multi-section structure and multi-mode nature of this laser diode, our model shows great advantage over other models. This co-operation with NORTEL has presented fruitful results.

7.1 Future Research

Based on the achievements presented in the previous section, we need to complete or improve some tool modules for future applications and to continue our research project or extend our research range.

In the material tool module, as we have shown in previous section, the models are quite good in the sense of physical concept explanation and qualitative trend prediction, however they still could not be used *automatically* as a quantitative simulation tool and be applied in various material simulations. To fill this gap, on one hand, we should have a systematic experimental measured data on the desired optical properties. On the other hand, we need an *automatic and smart* data processing procedure, which can fit our theoretical models to the measured data and also predict the optical properties in specific operating conditions. In the future research, we will continue to co-operate with industry, for example, NORTEL, to collect the desired experimental data. At the same time, we will adapt neural network method as the data processing procedure. In this method, several levels of neural cells, which consist of various prototype functions with fitting parameters, are applied. Firstly the neural network will spend a long time to "learn" the measured data. Mathematically, this

"learning" procedure is just to obtain various fitting parameters in the prototype functions. We also can choose a lot of fitting/optimization methods in this procedure, such as least square, genetic algorithm. After "learning", the neural network will validate the results, i.e., compare the results calculated by prototype functions with the experimental data. If it passed the validation test, the neural network will be ready in the applications; otherwise the learning procedure will be repeated. We can see that neural network method is almost ideal for the material modeling with the prototype functions already derived.

Generally speaking, we try to develop a general neural network algorithm. It will not only benefit material modeling, but also the other simulation and modeling, which can afford long "learning" time and require efficient and accurate simulation results during the real application.

In the laser diode models, transformation between the time domain and frequency domain is the main feature of this thesis. However, some improvements are still to be made. Firstly, we observed that optical spectrum obtained from FFT method was not so clear to show side peak/valley details. Secondly, in digital filter approach, we did not explore all methods except non-recursive approach. In the future research, we may borrow as many mature ideas as we can from digital signal processing area, where the subject has been investigated for a long time. Hopefully, we can solve the problem more flexibly between frequency and time domain and extend the idea to more complicated photonic circuit simulation and design.

Finally, to extend the tuning range of wavelength tunable laser, research engineers have designed various complex laser-structure in recent years. We suggest that the problem might be viewed from another angle. One is to make use of other material properties, such as magnetic effects or other material system in the laser fabrication.

The other is to leave the semiconductor material laser and find the possible wide wavelength tuning range in fiber laser.

In summary, we hope that with the achievement we accomplished and the continued research, our results will not only improve state-of-the art in modeling and simulation of optoelectronic devices and subsystem, but also make great impact on the research and development of optical devices in the industry.

Appendix

Derivation of 1D Effective Optical Equation

In this appendix, we will derive an effective 1D enveloped optical field equation. As shown in the previous chapter, this equation is the governing equation for both traveling wave model and standing wave model.

From Maxwell equations, we can easily derive electric field wave equation in the form

$$\nabla^2 E - \mu_0 \frac{\partial^2 D}{\partial t^2} - \mu_0 \frac{\partial^2 P_L}{\partial t^2} = \mu_0 \frac{\partial^2 P_S}{\partial t^2} \tag{A.1}$$

where P_L and P_S is the polarization related to lasing medium and spontaneous noise respectively. If ω is chosen as a reference frequency, we have

$$\begin{aligned} E(r,t) &= \mathrm{Re}[\hat{E}(r,t)\exp(j\omega t)] \\ D(r,t) &= \mathrm{Re}[\hat{D}(r,t)\exp(j\omega t)] \\ P_L(r,t) &= \mathrm{Re}[\hat{P}_L(r,t)\exp(j\omega t)] \\ P_S(r,t) &= \mathrm{Re}[\hat{P}_S(r,t)\exp(j\omega t)] \end{aligned} \tag{A.2}$$

where $\hat{E}$, $\hat{D}$, $\hat{P}_L$ and $\hat{P}_S$ are the slowly varying enveloped functions. Substituting eqn (A.2) into eqn (A.1), we obtain

$$\nabla^2\hat{E} + \mu_0\omega^2\hat{D} - 2j\mu_0\omega\frac{\partial\hat{D}}{\partial t} + \mu_0\omega^2\hat{P}_L = -\mu_0\omega^2\hat{P}_S \tag{A.3}$$

If define Fourier transform

$$\tilde{F} = \int_{-\infty}^{+\infty}\hat{F}\exp(j\Omega t)dt \tag{A.4}$$

and apply this transformation to eqn. (A.3), we have

$$\nabla^2\tilde{E} + \mu_0\omega^2\tilde{D} - 2j\mu_0\omega(j\Omega)\tilde{D} + \mu_0\omega^2\tilde{P}_L = -\mu_0\omega^2\tilde{P}_S \tag{A.5}$$

In Frequency domain, it is easily to show

$$\begin{aligned}\tilde{D} &= \varepsilon_0 n^2(\Omega)\tilde{E} = (\varepsilon_0 n^2(0) + 2n\frac{\partial n}{\partial\Omega}\Omega)\tilde{E}\\ \tilde{P}_L &= \varepsilon_0\chi_L(\Omega)\tilde{E}\end{aligned} \tag{A.6}$$

where n is refractive index and χ_L is the susceptibility related to lasing medium. If only consider the zero order effect of χ_L in eqn (A.6), and perform the reverse Fourier transform of eqn (A.5), we obtain

$$\nabla^2\hat{E} + \frac{\omega^2}{c^2}(n^2 + \chi_L)\hat{E} - 2j\frac{\omega}{c^2}nn_g\frac{\partial\hat{E}}{\partial t} = -\mu_0\omega^2\hat{P}_S \tag{A.7}$$

In deriving eqn (A.7), we have used the definition $n_g = n(1 - \frac{\lambda}{n}\frac{\partial n}{\partial \lambda})$, and omitted the higher order derivative of $\hat{E}$ respective to t.

We write the enveloped electric field in the form

$$\hat{E}(x, y, z, t) = \Phi(x, y)\Psi(z, t) \tag{A.8}$$

and assume that transverse field satisfies guided mode equation

$$\begin{aligned} &\nabla_t^2 \Phi(x, y) + \frac{\omega^2}{c^2}(n^2 - n_{eff}^2)\Phi(x, y) = 0 \\ &\int \Phi\Phi^* dxdy = 1 \\ &\int_{ACT} \Phi\Phi^* dxdy = \Gamma \end{aligned} \tag{A.9}$$

where n_{eff} is the effective index, the last integral is over the active region and Γ is optical confinement factor. Substituting eqns (A.8) and (A.9) into (A.7), finally we obtain an effective 1D equation for the electric field envelop

$$\frac{\partial^2 \Psi(z, t)}{\partial z^2} + \frac{\omega^2}{c^2}(n_{eff}^2 + \Gamma\chi_L)\Psi(z, t) - 2j\frac{\omega}{c^2}\overline{nn_g}\frac{\partial \Psi(z, t)}{\partial t} = -\mu_0\omega^2 f_s(z, t) \tag{A.10}$$

where $\overline{nn_g} = \int nn_g \Phi(x, y)\Phi^*(x, y)dxdy$. If we write the susceptibility in the form

$$\chi_L = \frac{\bar{n}}{k_0}(j + a_m)g$$

where $k_0 = \omega / c$ is the wave number at reference frequency and a_m is line-width enhancement factor. Also considering the background loss a_L, eqn (A.10) can be written as

$$\frac{\partial^2 \Psi(z,t)}{\partial z^2} + \frac{\omega^2}{c^2}\left[n_{eff}^2 - j\frac{\bar{n}c}{\omega}a_L + \frac{\bar{n}c}{\omega}\Gamma(j + a_m)g \right]\Psi(z,t)$$
$$- 2j\frac{\omega}{c^2}\overline{nn_g}\frac{\partial \Psi(z,t)}{\partial t} = -\mu_0 \omega^2 f_s(z,t)$$

Bibliography

Chapter.1.

[1]. M. Okai, *J. Appl. Phys.* Vol.75, p1, 1994.

[2]. H. Kogelnik and V. C. Shank, *Appl. Phys. Lett.* Vol.18, p152, 1971.

[3]. M. Nakamura, K. Aiki, J. Umeda and A. Yariv, *Appl. Phys. Lett.*Vol. 27, p403,1975.

[4]. H. Soda, Y. Kotaki, H. Sudo, H. Ishikawa, S. Yamakoshi and H. Imai, *J. Quantum. Electron.* Vol. 23, p804, 1987.

[5] F. Kano, Y. Thomori, Y. Kondo, M. Nakao and K. Oe, *Electron. Lett.*Vol. 25, p709, 1989.

[6]. M. Oberg, S. Nilsson, T. Klinga and P. Ojala, *IEEE Photon. Technol. Lett.*Vol.3, p299,1991.

[7]. S. Murata, I. Mito and K. Kobayashi, *Electron. Lett.* Vol.24, p577, 1988.

[8]. S. Takano, T. Sasaki, H. Yamada, M. Kitamura and I. Mito, *Electron. Lett.*, Vol. 25, p356, 1989.

[9]. X. Pan, H. Olesen and B. Tromborg, *Electron. Lett.* Vol.25, p1254, 1992

[10]. A. Zatni and J. Le Bihan, *J. Quantum. Electron.*Vol.31, p1009, 1995.

[11] G. P. Agrawal, Fiber-optic communication system, John Wiley & Sons, Inc, New York, 1992.

[12]. V. Jayaraman, Z-M. Chuang and L. A. Coldren, "Theory, design and performance of extended tuning range semiconductor lasers with sampled gratings", *IEEE. J. Quantum. Electron*. Vol. 29, 1824-1834, 1993.

[13]. Z-M. Chuang and L. A. Coldren, "Design of widely tunable semiconductor lasers using grating –assisted co-directional filters". *IEEE. J. Quantum. Electron* Vol. 19, 1071-1079, 1993.

[14]. J. Hong, H. Kim, F. Shepherd, C. Rogers, B. Baulcomb and S. Clements, " Matrix-grating strongly gain-coupled (MG-SGC) DFB lasers with 34nm continuous wavelength tuning range." *IEEE Photon. Technol. Letts*, Vol 11, 515-517, 1999.

Chapter.2

[1]. S. Adachi, *Physical Properties of III-V Semiconductor Compounds*, John Wiley & Sons, New York (1992).

[2]. P. S. Zory, JR, *Quantum Well Lasers*, Academic Press, Inc., New York (1993)

[3]. J. Terry, *J. Appl. Phys*. Vol. 70, 409, 1991.

[4]. S. Adachi, *Phys Rev B*,. Vol. 35, p35, 1987.

[5]. S. Adachi, *Phys Rev B*, Vol. 39, p12612, 1989.

[6]. S. Adachi, *J. Appl. Phys*, Vol. 66, p6030, 1989.

[7]. J. Micallef and B. L Weiss, *Opt. Quantum. Electron*. Vol. 23, p669, 1991.

[8]. S. Okhe, T. Umeda and Y. Cho, *Opt. Commun*. Vol. 56, p235, 1985.

[9]. J. Weber, *J. Quantum. Electron*. Vol. 30, p1801, 1994.

[10] B. R. Bennett, R. A. Soref and J. A. Alamo, *J. Quantum. Electron*. Vol. 26, p113, 1990.

[11]. K. Tharmalingam, *Phys Rev*. Vol.130, p2204 ,1963.

[12]. A. Alping and L. A. Coldren, *J. Appl. Phys*. Vol. 61, p2430, 1987.

[13]. H. C. Casey, JR and M. B. Panish, *Heterostructure Lasers Part A*. Academic Press, Inc. New York (1978).

[14]. A. R. Adams, *Electron. Lett.* Vol. 22, P249, 1986.

[15]. E. Yablanovitch and E. O. Kane, *IEEE J. Lightwave Technol.* Vol.4, p504, 1986.

[16]. Z. M. Li, M. Dion, Y Zou, J Wang, M Davies and S. P. McAlister. *J. Quantum. Electron.* Vol. 30, p1538, 1994.

[17]. T. Makino, *J. Quantum. Electron.* Vol. 32, p493, 1996.

[18]. S. L. Chuang, *Phys. Rev. B.* Vol.43, p9649, 1991.

[19]. S. W. Corzine, R. H. Yan and L. A. Coldren, *Appl. Phys. Lett.* Vol.57, p2835, 1990.

[20]. F. Stern, *J. Appl. Phys.* Vol.47, p5382, 1976.

[21]. S. L. Chuang, *Physics of Optoelectronic Devices.* John Wiley & Sons, Inc. New York, 1995.

[22]. D. Ahn and S. L. Chuang *J. Quantum. Electron.* Vol. 26, p13, 1990.

[23] Z. Michaliewicz, *Genetic algorithms + Data structures = Evolution Programs.*, Springer-Verlag, New York, 1992

[24] X. Li, W. Li, W. - P. Huang and P. K. Lau, "Validation of ALDS- a 3D laser diode simulator". To be submitted to *J. Quantum. Electron.2000.*

[25].K. N., Gurney, *An introduction to neural networks*, UCL Press, London, 1997.

[26] W. Li, Comprehensive Research Report, University of Waterloo, Dept. of Electrical & Computer Engineering, 1997.

[27] T. Tamir, *Guided-Wave Optoelectronics, Chapter 4*, Springer-Verlag, New York, 1988.

[28] C. - S. Chang, S. – L. Chuang, J. R. Minch, W. W. Fang, Y. K. Chen and T. Tanbun-EK, "Amplified spontaneous emission spectroscopy in strained quantum-well lasers". *J. Selected. Topic. Quantum. Electron.* Vol. 1, p1100-1107, *1995.*

Chapter.3

[1] L. M. Zhang, S. F. Yu, M. Nowell, D. D. Marcenac, and J. E. Carroll, "Dynamic analysis of radiation and side mode suppression in second order DFB lasers using time-domain large signal traveling wave model," *IEEE J. Quantum Electron.*, Vol 30, no. 6, pp.1389-1395, 1994.

[2] C. F. Tsang, D. D. Marcenac, . E. Carroll and L. M. Zhang, "Comparison between 'power matrix model (PMM)' and 'time domain model (TDM)' in modeling large signal responses of DFB lasers," *IEE Proc. J*, Vol 141, no.2, pp.89-96, 1994.

[3] M. Ito and T. Kimura, "Stationary and transient thermal properties of semiconductor laser diode," *IEEE J. Quantum Electron.*, Vol.17, no.5, pp. 787-795,1981.

[4] Xun Li and Wei-Ping Huang, " Simulation of DFB semiconductor lasers incorporating thermal effects," *IEEE J. Quantum Electron.*, Vol. 31, no.10, pp.1846-1855, 1995.

[5] S. Kobayashi, Y. Yamamoto, M. Ito and T. Kimura, "Direct frequency modulation in AlGaAs semiconductor laser," *IEEE J. Quantum Electron.*, Vol.18, pp. 582-594, 1982.

[6] Avi Zadok, Hamutal Shalom, Moshe Tur, W. D. Conwell, and Ivan Andonovic, "Spectral shift and broadening of DFB lasers under direct modulation," *IEEE Photon. Technol. Lett.*, Vol.10, pp.1709-1711, 1998.

[7] S. Ogita, A. J. Lowery and R. S. Tucker, "Influence of asymmetric nonlinear gain on the transient intensities of longitudinal modes in long wavelength Fabry-Perot laser diodes," *IEEE J. Quantum Electron.*, Vol.33, pp.198-210, 1997.

[8] A. A. Saavedra, R.Passy and J. P. von der Weid, "Thermal drift in wavelength switching DFB and DBR lasers," *Electron. Lett.*, Vol. 33, pp.780-781, 1997.

[9] H. Shalom, A. Zadok, M. Tur, P. J. Legg, W. D. Cornwell and I. Andonovic, "On the various time constants of wavelength changes of a DFB laser under direct modulation," *IEEE J. Quantum Electron.*, Vol. 34, pp. 1816-1844, 1998.

[10] W. Li, X. Li and W. -. P. Huang, "A traveling wave approach for laser diodes with consideration for thermal effects". Submitted to *J. Quantum. Electron,1999.*.

[11] William H. Press, Brian P. Flannery, Saul A. Teukolsky and William T. Vetterling, *Numerical Recipes (Fortran)*, Cambridge: Cambridge Univ. Press, 1989.

[12] Govind P. Agrawal and Niloy K. Dutta, *Semiconductor Lasers* Chapter 5, New York: VNR, 1993.

[13] Toshihiko Makino and Jan Glinski, " Transfer matrix analysis of the amplified spontaneous emission of DFB semiconductor laser amplifiers." *IEEE J. Quantum Electron.*, Vol. 24, pp. 1507-1518, 1988.

[14] T. Makino, "Transfer matrix theory of the modulation and noise of multi-element semiconductor lasers," *IEEE J. Quantum Electron.*, Vol.29, pp.2762-2770,1993.

[15] W. R. Smith, J. R. King and B. Tuck, "Mathematical modeling of thermal effects in semiconductor laser operation," *IEE Proc.-Optoelectron.*, Vol.144, pp.389-396, 1997.

[16] A. J. Lowery, *IEE Proc. J*, Vol 139,402-406,1992.

[17] COST240 Group, *IEE Proc-Optielectron*, Vol.141, p82-88, 1994

[18] L. M. Zhang and J. E. Carroll, " Large signal dynamic model of the DFB laser," *IEEE J. Quantum Electron*, Vol. 28, pp. 604-611,1992.

[19] Xun Li, A. D. Sadovnikov, W.-P. Huang and Toshihiko Makino, " A physics-based three-dimensional model for distributed feedback laser diodes," *IEEE J. Quantum Electron*, Vol.34, pp.1545-1553, 1998.

[20] A. J. Lowery, " New dynamic semiconductor laser model based on the transmission line modeling method," *IEE Proc. J*, Vol.134, pp.281-289,1987.

[21]. H. E. Lassen, H. Wenzel and B. Tromborg, *IEE Electron. Lett.*, Vol. 29, 1124-1126, 1993.

Chapter.4

[1]. M. Ohtsu, ed , *Frequency Control of Semiconductor Lasers*, John Wiley & Sons, Inc. New York, 1996.

[2]. J. Archambault and S. G. Grubb, "Fiber Gratings in Lasers and Amplifiers.", *J. Lightwave. Technol.* Vol.15, No.8, pp.1378-1390,1997.

[3]. A. V. Oppenheim and R. W. Schafer, *Discrete-Time Signal Processing*, Pretice-Hall, Inc, Englewood Cliffs, 1989.

[4]. W. H. Press, B. P. Flannery, S. A. Teukolsky and W. T. Vetterling, Numerical Recipes (Fortran Version), Cambridge University Press, Cambridge, 1989.

[5]. M. Yamada and K. Sakuda, "Analysis of almost-periodic distributed feedback slab waveguides via a fundamental matrix approach." Appll. Opt., Vol.26 3474-3478, 1987.

[6]. W. Li, W. - P. Huang and X. Li, "Digital filter approach for simulation of complex integrated laser diodes on the traveling wave model." Submitted to *IEEE. J. Quantum. Electron.* 1999.

Chapter.5

[1]. M. Ohtsu, ed , *Frequency Control of Semiconductor Lasers*, John Wiley & Sons, Inc. New York, 1996.

[2]. G. Agrawal, *Fiber-Optic Communication Systems*, John Wiley & Sons, Inc. New York, 1992

[3]. V. Jayaraman, Z-M. Chuang and L. A. Coldren, "Theory, design and performance of extended tuning range semiconductor lasers with sampled gratings", *IEEE. J. Quantum. Electron.* Vol. 29, 1824-1834, 1993.

[4]. Z-M. Chuang and L. A. Coldren, "Design of widely tunable semiconductor lasers using grating –assisted co-directional filters". *IEEE. J. Quantum. Electron* Vol. 19, 1071-1079, 1993..

[5]. R. C. Alferness, U. Koren, L. L. Buhl, B. I. Miller, M. G. Young, T. L. Koch, G. Raybon and A. Burrus, "Broadly tunable InGaAsP/InP laser based on a vertical coupler filter with 57 nm tuning range." *Appl. Phys. Lett*, Vol.60 3209-3211, 1992.

[6] V. Jayaraman, M. E. Heimbuch, L. A. Coldren and S. P. Denbarrs, "Widely tunable continuous wave InGaAsP/InP sampled grating lasers", *IEE Electron. Lett*, Vol. 30, 1492-1494, 1994.

[7]. B-S. Kim, J-K. Y. Chung and S-H. Kim, "Time-domain large signal analysis of widely tunable DBR laser diodes with periodically sampled and chirped gratings." *IEEE Photon. Technol. Lett*, Vol.10, 39-41, 1998.

[8]. R. C. Alferness, T. L. Koch , L. L. Buhl, F. Storz, F. Heismann and M. Martyak, "Grating assisted InGaAsP/InP vertical codirectional coupler filter" *Appl. Phys. Lett*, Vol.55, 2011-2013, 1989.

[9]. Toshihiko Makino and Jan Glinski, " Transfer matrix analysis of the amplified spontaneous emission of DFB semiconductor laser amplifiers." *IEEE J. Quantum Electron.*, Vol. 24, pp. 1507-1518, 1988.

[10]. W. Li and W. - P. Huang, "Modeling and simulation on sampled grating laser diode with the split-step traveling wave approach." To be submitted to *IEEE J. Quantum. Electron*,2000.

Chapter.6

[1]. P. E. Green, "Fiber Optic Networks", Prentice Hall, Englewood Cliffs, NJ, 1993.

[2]. J. Hong, H. Kim, F. Shepherd, C. Rogers, B. Baulcomb and S. Clements, " Matrix-grating strongly gain-coupled (MG-SGC) DFB lasers with 34nm continuous wavelength tuning range." *IEEE Photon. Technol. Letts*, Vol 11, 515-517, 1999.

[3] W. Li, W. - P. Huang, X. Li and J. Hong, "Traveling wave model for laser diodes and its applications on multi-section DFB laser". NORTEL networks research report, 1999.

[4]. W. Li, W. - P. Huang, X. Li and J. Hong, "Multi-wavelength gain coupled DFB laser cascades: Design modeling and simulation". Submitted to *IEEE. J. Quantum. Electron*, 1999.

[5]. G. P. Agrawal and N. K. Dutta, "Semiconductor Lasers." Van Nostrand Reinhold, New York, 1993.

[6]. S. L. Chuang, "Physics of optoelectronic devices." John Wiley & Sons, Inc, New York, 1995.